

Centre
Eau Terre Environnement

**Electrical Resistivity Tomography Data Assimilation Using Ensemble
Kalman Filter for heat tracing test: a Case Study in Quebec City,
Quebec, Canada**

Par
Benyamin Shariatinik

Thèse présentée pour l'obtention du grade de
Philosophiae Doctor (Ph.D.)
en sciences de la Terre

Jury d'évaluation

Président du jury et
examinateur interne

Richard Martel
INRS-ETE
Université du Québec

Examinateur externe

James Irving
Faculty of Geoscience and Environment
University of Lausanne

Examinateur externe

Véronique Gervais-Couplet
IFP Energies Nouvelles

Directeur de recherche

Erwan Gloaguen
INRS-ETE
Université du Québec

Codirecteur de recherche

Jasmin Raymond
INRS-ETE
Université du Québec

AKNOWLEDGEMENT

Words cannot express my gratitude to my supervisor Erwan Gloaguen for his invaluable patience feedback and moral support. I really inspired by your professional and personal character.

I would like to express my deepest appreciation to my co-supervisor Jasmin Raymond for all his knowledge and expertise shared with me.

I would like to thank the members of the jury Richard Martel, James Irving and Véronique Gervais-Couplet for accepting to take a critical look at my work, I could not have undertaken this journey without you, who generously provided knowledge and expertise.

Special thanks to Bouchedar Abderezack for all the discussion we had about ERT forward modeling and inversion methods and an amazing ERT forward modeling and inversion theory course.

I am also grateful to Luis-charles Boutin for all advice and suggestions about groundwater modeling and FEFLOW software.

I had the pleasure of working with my colleagues Oleksandra Pedchenko, Lee Victoria and Charis Wong, the field work was enjoyable next to you. Thanks should also go to my officemates Amirhossein, Milad, Jerome, Thomas and Matthieu for making a friendly atmosphere.

Lastly, I wish to extend my special thanks to my family, especially my spouse for all their emotional support. Their belief in me has kept my spirits and motivation high during this process.

RÉSUMÉ

Les systèmes d'énergie géothermique, comme les pompes à chaleur d'aquifère utilisent le sous-sol dans les zones urbaines comme sources d'énergie renouvelable. Il est nécessaire de caractériser les propriétés hydrauliques du sous-sol avant l'installation de tels systèmes. Dans ce contexte, un test d'injection de chaleur est une méthode reconnue qui peut aider à l'optimisation de la conception du système. Lors de ces tests d'injection de chaleur, le suivi peut être effectué avec des capteurs de température, des capteurs de pression d'eau et la tomographie de résistivité électrique (ERT) pour aider à caractériser les propriétés hydrogéologiques. Les outils de surveillance utilisés antérieurement comportent des lacunes comme des données de faible résolution et un lissage excessif, de sorte qu'ils ne peuvent pas reproduire l'hétérogénéité des propriétés hydrogéologiques. Les filtres de Kalman d'ensemble (EnKF) est un outil prometteur qui peut aider à surmonter le problème du lissage excessif pour évaluer l'hétérogénéité des propriétés hydrogéologiques. Ici, nous proposons une méthodologie pour assimiler les données d'ERT dans un modèle numérique d'écoulement des eaux souterraines et de transfert de chaleur; où l'eau souterraine est extraite, et l'eau chauffée est réinjectée dans un aquifère de gravier sableux non confiné, soit un site expérimental situé à Québec au Canada. L'ensemble de données d'ERT contient 11 étapes temporelles. Nous avons évalué la qualité des données ERT en vérifiant la moyenne des variations de résistivité apparente mesurées au fil du temps et en effectuant une inversion électrique pour vérifier si elles contiennent des informations sur l'expérience d'injection de chaleur. Le modèle à éléments finis de l'écoulement des eaux souterraines et du transfert de chaleur développé avec FEFLOW 7.3 a été intégré à la relation pétro physique et à la modélisation électrique directe (Resipy) afin d'estimer les valeurs de résistivité électrique. Ensuite, la résistivité apparente estimée est assimilée pour mettre à jour le modèle de conductivité hydraulique en utilisant l'EnKF. Les résultats démontrent que l'approche proposée peut reproduire l'hétérogénéité de K puisque le modèle K mis à jour est raisonnablement conforme au logarithme lithologique. De plus, l'approche proposée a été en mesure de reproduire les mesures de température et de la ERT. La comparaison entre la distribution antérieure et postérieure de K avec ceux obtenus à partir d'essais lugeon montre que l'EnKF a fourni une distribution assimilée de K qui s'est déplacée vers des valeurs inférées avec les essais lugeon.

Mots-clés : Systèmes d'énergie Géothermique, Expérience de traçage de la chaleur, Tomographie de résistivité électrique entre forages, Ensemble Kalman filtre, Conductivité hydraulique, Essais lugeon, Suivi de la température.

ABSTRACT

Geothermal Energy Systems such as groundwater heat pumps relying on aquifers uses renewable sources of energy that are accessible in urban areas. It is necessary to characterize the subsurface hydraulic properties prior to the installation of such systems. In this context, heat tracing experiments is a typical field test that can help with characterization of the subsurface. During a heat tracing experiment, monitoring with downhole temperature sensors, water-level pressure transducers and electrical resistivity tomography (ERT) can be used to characterize the hydrogeological properties. The mentioned monitoring tools contain shortcomings such as low-resolution data and over-smoothing, which prevents them from correctly reproducing the heterogeneity of hydrogeological properties. Ensemble Kalman filter (EnKF) is a promising tool that can overcome the over-smoothing problem to replicate the hydrogeological property heterogeneity. Here, we proposed a workflow to assimilate time-lapse cross-borehole ERT data into a numerical model of groundwater flow and heat transfer. The workflow was tested in a heat tracing experiment where the groundwater was extracted and heated water was reinjected into an unconfined sandy-gravel aquifer located in Quebec City, Canada. The time-lapse cross-borehole ERT surveys contained 11 time-steps. The quality of the monitoring cross-borehole ERT data was assessed by checking the mean value of apparent resistivity of each dataset overtime and also by performing electrical inversion to check if they contained information about heat tracing experiment. The finite element model of groundwater flow and heat transfer developed with FEFLOW 7.3 was integrated with petrophysical relationship and electrical forward modeling (Resipy) to estimate cross-borehole ERT measurements. Then, the estimated apparent resistivity was assimilated to update the hydraulic conductivity (K) model using EnKF. The results demonstrate that the proposed approach can reproduce the heterogeneity of K since the updated K model is reasonably consistent with the lithological log. In addition, the proposed approach was able to reproduce the cross-borehole ERT field and temperature measurements. The comparison between prior and posterior distribution of K with those obtained from slug tests shows that the EnKF provided an assimilated distribution of K that moved toward values inferred with slug tests.

Keywords : Geothermal energy systems, Heat-tracing experiment, Cross-borehole electrical resistivity tomography, Ensemble Kalman filter, Hydraulic conductivity, Slug test, Temperature monitoring.

SOMMAIRE RÉCAPITULATIF

Introduction

Note : Dans ce chapitre, la numérotation des figures est cohérente avec la partie anglaise.

La récente crise climatique s'explique principalement par la consommation de combustibles fossiles (Maslin, 2004). Les effets de la hausse des températures ont des conséquences sur la dégradation des sols, la perte de productivité des terres agricoles et la désertification, la perte de biodiversité, la dégradation des écosystèmes, la baisse des ressources en eau douce, l'acidification des océans et la perturbation et l'appauvrissement de l'ozone stratosphérique (Rossati, 2017).

Il est important de développer des sources d'énergie renouvelable pour réduire la consommation de carburant. Les systèmes de pompes à chaleur géothermique dont les pompes à chaleur d'aquifère dans lesquelles les puits sont installés au niveau de la sous-surface à une profondeur inférieure à 200 m et avec une température inférieure à 25 °C sont maintenant considérées comme une option durable pour le chauffage et la climatisation (Raymond, 2018; Xu, et al., 2020). Ils fournissent aux bâtiments résidentiels et commerciaux une technologie de chauffage et de climatisation moins polluante que les systèmes conventionnels. Ces systèmes géothermiques de faible profondeur tirent profit de l'inertie thermique terrestre considérée comme une source d'énergie renouvelable qui mérite d'être développée (Bayer, et al., 2019). En effet, les systèmes géothermiques à faible profondeur en zone urbaine sont considérés comme une solution efficace pour réduire la consommation de combustibles fossiles selon une démarche de décarbonisation (Raymond, 2018).

L'efficacité des systèmes géothermiques dépend non seulement de la performance des échangeurs de chaleur, mais aussi de la nature et de l'hétérogénéité de la roche et des fluides formant le système aquifère (Raymond, 2018). Par conséquent, la caractérisation des propriétés hydrogéologiques est essentielle à la mise en valeur, à l'exploitation, à la gestion et à la préservation durables des ressources géothermiques (Cultrera, et al., 2018; Hermans, et al., 2012). La caractérisation et l'exploitation durable des aquifères reposent, entre autres, sur notre capacité à prédire les écoulements de l'eau souterraine (Marsily, et al., 2005), lesquels sont principalement fonction de la distribution spatiale de la conductivité hydraulique (K) dans l'aquifère.

Il y a plusieurs outils pour mesurer directement ou indirectement la conductivité hydraulique. Par exemple, les données conventionnelles mesurées in situ ou ex-situ afin d'effectuer la caractérisation hydrogéologique sont:

1. les analyses en laboratoire d'échantillons dits non-remaniés récoltés le long de forages.
2. les mesures hydrogéologiques consistant en une série de tests de perméabilité in situ (Macdonald, et al., 2008).

Bien qu'essentielles et relativement exactes, ces données sont locales et à plus grande échelle, elles ont une résolution grossière. De plus, ces méthodes ne donnent pas d'information sur la continuité spatiale des propriétés hydrogéologiques.

En effet, les coûts élevés de l'installation et du développement des puits restreignent leur nombre, ce qui ne permet pas d'évaluer la variabilité spatiale de K à une échelle pertinente pour identifier le design optimal des systèmes géothermiques. Conséquemment, de nouvelles technologies et méthodologies sont nécessaires pour mieux caractériser l'hétérogénéité des propriétés hydrogéologiques et thermiques des matériaux de proche surface, tout en minimisant et optimisant le nombre de puits.

En plus des données conventionnelles, les tests d'injection de chaleur sont effectués pour caractériser les propriétés hydrauliques et thermiques des aquifères (Anderson, 2005; Saar, 2011). L'expérience peut être faite conjointement avec le profilage de la température en fond de forage et la tomographie de résistivité électrique (ERT) mesurée dans le temps comme outils de suivi sur le terrain. Si les deux outils de suivi précédents ont été utilisés avec succès dans un certain nombre de projets, ils souffrent néanmoins de certains inconvénients. Le profilage de la température au fond du forage ne saisit que l'état local du système. La couverture et la résolution spatiales sont par conséquent limitées. Pour pallier le défaut de résolution de ces données, des méthodes géophysiques ont émergé. La méthode ERT est populaire pour les études hydrogéologiques, car les mesures ERT dans le temps sont sensibles aux variations de la résistivité qui est elle-même caractéristique des variations des propriétés des fluides. La méthode ERT dans le temps permet une couverture spatiale dense de la résistivité électrique en 2D/3D afin d'évaluer les variations dynamiques peu profondes de l'état hydrogéologique d'un site (Binley, et al., 2015). Au cours des dernières décennies, l'ERT dans le temps a été mis en œuvre avec succès pour caractériser la géométrie d'un panache thermique (Aghasi, et al., 2013) ou pour représenter l'espace et le mouvement temporel du panache (Pidlisecky, et al., 2011; Singha and Gorelick, 2006). La lacune associée à l'inversion ERT est un lissage excessif, de sorte que les

valeurs extrêmes des paramètres inversés sont inférieures aux vraies valeurs. En d'autres termes, la régularisation conduit la solution vers un sous-espace de solutions acceptables mais au détriment de la variance des paramètres (Day-Lewis, et al., 2005). En outre, il y a plus de paramètres à prendre en compte que de données, ce qui rend un problème pour lequel il y a plus d'une solution qui correspond aux données (ill-posed problem; Menke, 1984).

La méthode d'assimilation bayésienne a été mise en œuvre progressivement au cours des dernières années dans le domaine hydrogéologique (Chen and Zhang, 2006; Tso, et al., 2020; Bouzaglou, et al., 2018; Camporese, et al., 2011). L'idée est d'intégrer des mesures ERT dans le temps et des modèles numériques d'écoulement des eaux souterraines afin de mieux décrire l'état actuel d'un système hydrogéologique (Wiklea and Berliner, 2007). L'assimilation bayésienne peut fournir une meilleure prévision de l'état futur du système, ce qui est la tâche que les outils de suivi conventionnels ne permettent pas d'accomplir. Dans (Tso, et al., 2020), l'approche Ensemble Smoother with Multiple Data Assimilation (ES-MDA) a été proposée pour identifier divers paramètres de détection de fuites à l'aide de données ERT dans le temps. Afin d'estimer les propriétés hydrauliques du sol dans une expérience en laboratoire d'intrusion d'eau salée, les données d'ERT ont été assimilées dans un modèle hydrogéologique à l'aide d'EnKF (Bouzaglou, et al., 2018).

Dans la présente étude, nous avons l'intention d'évaluer le potentiel de la mise en œuvre d'EnKF (Evensen, 1994) pour estimer l'hétérogénéité de la K de l'aquifère dans une expérience de traçage thermique dans une optique de conception de pompes à chaleur d'aquifère. Cette étude a également permis d'évaluer la capacité d'EnKF à traiter les incertitudes de l'expérience de terrain. À cette fin, une expérience de traçage thermique effectuée par pompage des eaux souterraines et réinjection d'eau chaude dans un aquifère de sable et gravier non confiné a été conçue. Les données de tomographie de résistivité entre forages ont été utilisées pour suivre l'évolution du changement de la température souterraine. En outre, un modèle numérique d'éléments finis de l'écoulement des eaux souterraines et du transport de la chaleur (FEFLOW 7.3) (Diersch, 2014) a été mis au point pour simuler l'expérience de traçage de la chaleur. À chaque pas de temps de surveillance ERT, le modèle de température souterraine résultant de simulations numériques est converti en conductivité électrique en utilisant la relation pétrophysique. Ensuite, le modèle de conductivité électrique obtenu est utilisé pour exécuter une modélisation électrique directe avec Resipy (Saneian, et al., 2018). La modélisation électrique directe fournit des valeurs d'ERT aux mêmes points de mesures enregistrés sur le terrain. Enfin,

les mesures de champ ERT sont assimilées dans le modèle de transport de chaleur à l'aide de l'approche EnKF pour mettre à jour le modèle K.

Objectifs de recherche

L'objectif de notre projet est de développer des outils méthodologiques et numériques de caractérisation de la distribution spatiale des propriétés hydrauliques du sous-sol dans le but d'optimiser les systèmes géothermiques. Ces développements sont testés sur un site expérimental dans le cadre d'un projet de recherche en géothermie nommé Aquifroid où le potentiel des pompes à chaleur d'aquifère est étudié.

Dans la présente étude, une approche multidisciplinaire est proposée afin d'estimer la conductivité hydraulique d'un aquifère lors d'un essai d'injection de chaleur. L'idée générale consiste à faire un suivi temporel du panache de chaleur avec la méthode de résistivité entre forages couplés avec des mesures de température in situ afin d'intégrer l'ensemble des données dans un modèle numérique de l'écoulement des eaux souterraines et du transfert de chaleur qui permettra de faire des prédictions les plus fiables. Nous proposons de développer de nouveaux outils numériques d'intégration de données géophysiques et un modèle numérique dans le but de simuler de façon couplée l'écoulement de l'eau souterraine et le transfert de chaleur. Ces algorithmes permettront de caractériser l'hétérogénéité spatiale de la distribution de K qui seront considérés dans les simulations. Les développements scientifiques de ce projet permettront aussi d'améliorer les méthodes de conception des systèmes géothermiques utilisés pour le chauffage et la climatisation des bâtiments.

Site d'étude

L'expérience de traçage thermique a été réalisée à Québec, au Canada, près de la baie de Beauport, sur la rive nord du fleuve Saint-Laurent (Figure 1.10a). La caractérisation du site a commencé par un essai de pénétration au cône (CPT) pour mieux comprendre les lithologies présentes sur le site. La Figure 1.11b montre la lithologie interprétée des mesures CPT à l'emplacement du puits #2. La stratigraphie du site a été interprétée et comprend cinq unités avec une séquence de couches de limon, de sable et de gravier sur une couche d'argile compacte. Entre 24 et 30 m de profondeur, on trouve un aquifère de sable et de gravier, avec une fraction de gravier qui augmente en profondeur.

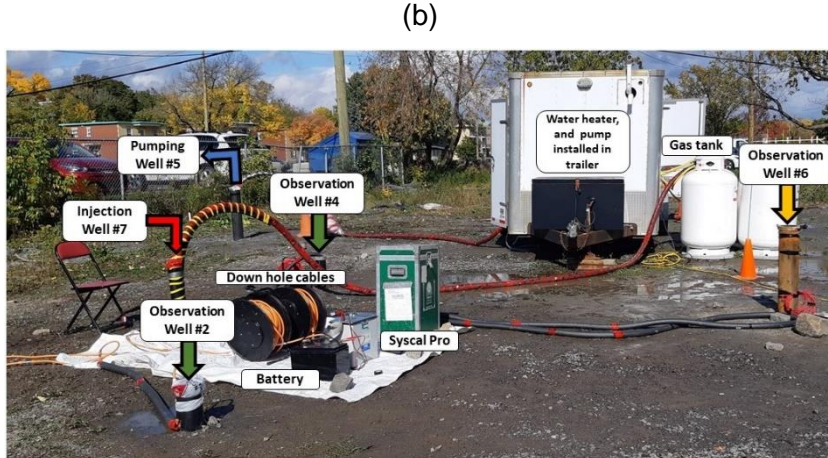
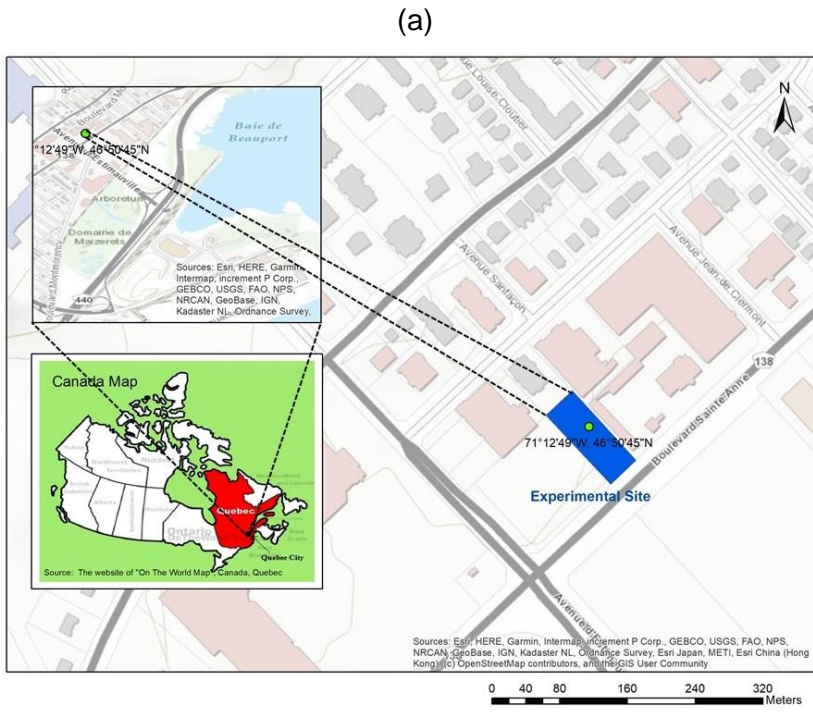


Figure 1.10 : a) Le site d'étude est situé près de la baie de Beauport, sur la rive nord du fleuve Saint-Laurent à Québec, au Canada. b) Installation de l'équipement de traçage thermique sur le site et emplacement des puits de pompage, d'injection et d'observation. La position du pompage, de l'injection et de trois puits de surveillance ERT, le câble de fond de trou acheminé au fond des puits #2 et #4 ainsi que le chauffe-eau installé dans la remorque sont montrés.

Cinq puits ont été installés sur ce site pour effectuer l'expérience d'injection de chaleur (Figure 1.10b et Figure 1.11a). Un puits de pompage (puits #5) a été foré dans la partie nord du site pour fournir l'eau qui sera réchauffée et réinjectée. Le puits #5 est en amont hydraulique par rapport au puits d'injection (puits #7) et les deux sont espacés de cinq mètres. Trois autres puits d'observation ont été forés pour effectuer les mesures de tomographie de résistivité électrique entre forages et le suivi temporel de la température. Le puits #2 et le puits #6 se trouvent dans la

partie sud du site, et le puits #4 a été foré au centre du site. Les puits #2 et #4 étaient équipés de six électrodes avec un écartement d'un mètre qui couvre l'intervalle de la crête des puits. En outre, une électrode a été installée au fond du puits #6 comme électrode dite à l'infini pour réaliser une configuration pôle-dipôle. Les limites latérales du site ne permettaient pas de mettre l'électrode à l'infini à la surface. Tous les puits ont été crevés dans l'intervalle entre 24 m et 30 m de profondeur (Figure 1.11b), sauf le puits #4 qui est crevé sur toute la longueur saturée de l'aquifère. La direction de l'écoulement des eaux souterraines est ouest-est, perpendiculairement à la section entre les puits #2 et #4 (Figure 1.11a).

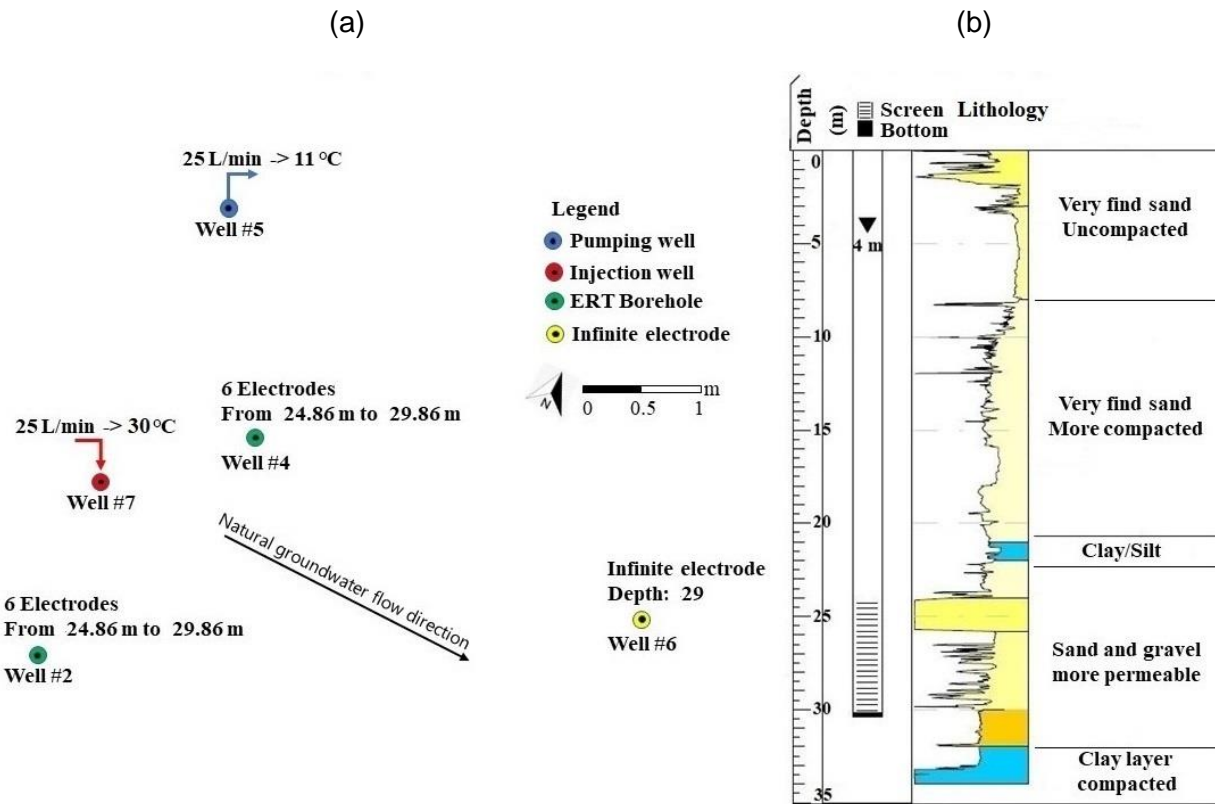


Figure 1.11 : a) La configuration des puits de pompage, d'injection et de surveillance ERT b) les unités lithologiques interprétées à l'aide des diagraphies CPT dans le puits 2 et le schéma du tubage installé.

Des tests de réponse thermique avec un câble chauffant ont été effectués dans le puits #4 et le puits #6 pour mesurer la conductivité thermique de chaque couche plusieurs semaines avant l'essai d'injection de chaleur. Des capteurs de température et des sondes de niveau d'eau ont été installés dans les puits avant le lancement de l'expérience afin de mesurer la température non perturbée de l'aquifère et le gradient hydraulique, respectivement.

Le pompage et l'injection de chaleur ont débuté le 1er septembre 2020 et ont duré 75 heures. Les débits de pompage et d'injection ont varié au fil du temps de 25 à 3 ($\text{l} \cdot \text{min}^{-1}$) en raison du

colmatage du puits d'injection dû à l'activité biologique. L'eau pompée est passée directement par un chauffe-eau et a été réinjectée dans le puits #7 à une température d'environ 30 °C. La température de base de l'aquifère avant l'expérience de traçage thermique était de 10.3 °C. Au cours de l'expérience, les mesures de tomographie de résistivité ont été effectuées 11 fois à intervalle de temps non régulier variant de 6 à 12 heures.

Méthodologie

Étapes de réalisation

La mise en œuvre de l'assimilation de données dans le cadre de l'hydrogéologie est une approche multidisciplinaire visant à intégrer l'hydrogéophysique et l'assimilation de données pour mieux caractériser les propriétés hydrauliques de la sous-surface et des fluides (Figure 2.1). Un ensemble de paramètres de conductivité hydraulique est fourni au début du processus à travers des simulations géostatistiques. L'ensemble est propagé par la simulation transitoire de l'écoulement de l'eau souterraine et du transport de chaleur pour modéliser la température du sous-sol à un temps donné. Ensuite, les températures calculées sont converties en une distribution de résistivité électrique 3D au moyen d'une relation pétrophysique. Une modélisation directe électrique utilisant la distribution de résistivité électrique 3D calculée dans la dernière étape est calculée pour prédire la résistivité électrique apparente souterraine à l'emplacement des électrodes. Enfin, les mesures de tomographie de résistivité entre forages (observations) et la résistivité électrique apparente prévue (sortie de la modélisation électrique directe) sont assimilées pour mettre à jour la conductivité hydraulique de l'ensemble. Dans les sous-sections suivantes, chaque étape est expliquée en détail.

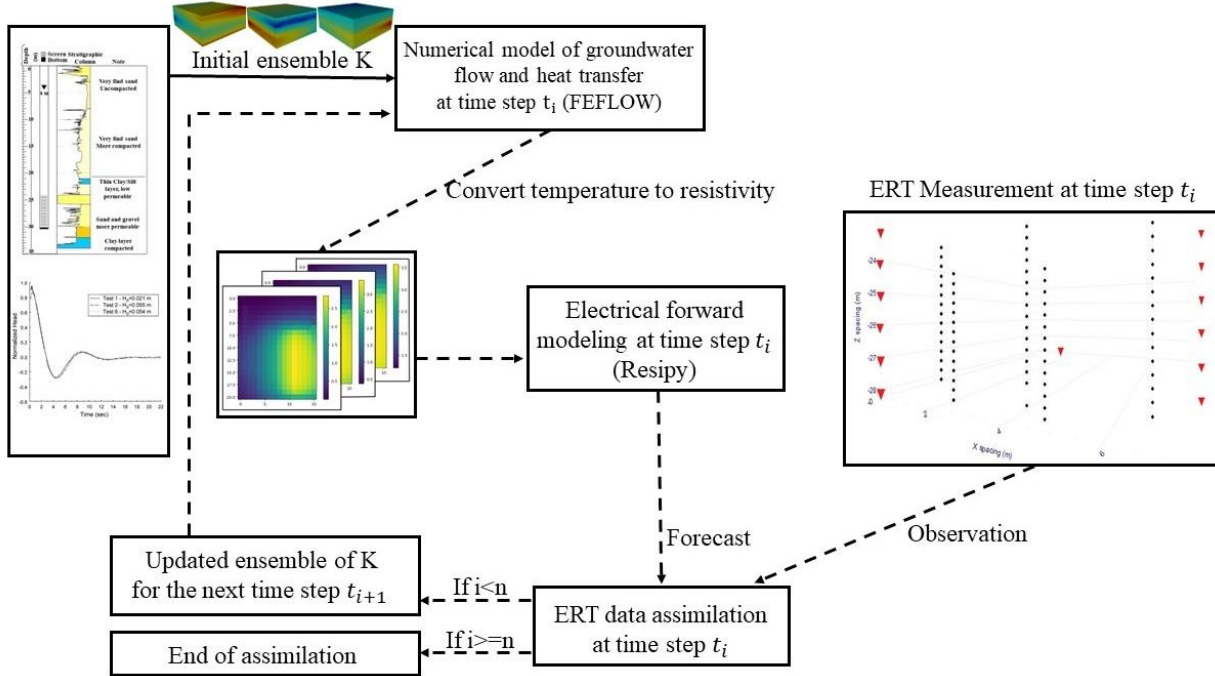


Figure 2.1 : Les étapes de réalisation des travaux montre la mise en œuvre de l'assimilation de données ERT inter-forages en accéléré pour calibrer la distribution 3D de la conductivité hydraulique. La lettre n désigne le nombre de pas de temps de suivi.

Modèle numérique de l'écoulement des eaux souterraines et du transfert de chaleur

Les fonctions d'API de FEFLOW 7.3 (DHI, n.d.) ont été utilisées pour reproduire les résultats de l'expérience de traçage de la chaleur afin de mieux comprendre le système d'écoulement de l'eau souterraine. Dans cette étude, la conductivité hydraulique est la variable d'état à mettre à jour par l'assimilation des données ERT. Un ensemble initial de 100 réalisations de conductivité hydraulique 3D a été généré en utilisant l'approche de simulation gaussienne séquentielle (SGS) (Remy, et al., 2009) non conditionnelle basée sur les informations précédentes des mesures sur le terrain et les informations en bibliographie (Hwang, et al., 2017; Talbot Poulin, et al., 2013). La simulation SGS a été effectuée à l'aide du logiciel de simulation géostatistique libre SGeMS.

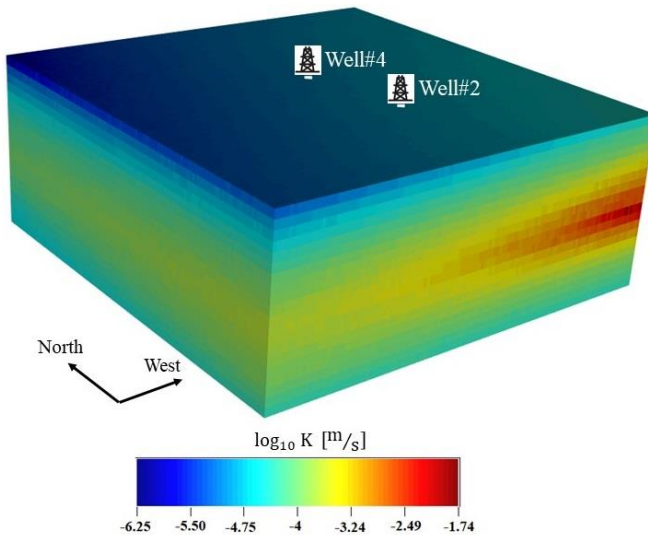


Figure 3.1 : La distribution 3D des conductivités hydrauliques de l'aquifère de gravier sableux ($\log_{10} K$ [m/s]) fournie par SGS. L'emplacement du puits de pompage (puits #4) et d'injection (puits #2) est indiqué.

Les dimensions du modèle sont de 14m x 19m x 14m le long des axes X, Y et Z, respectivement. Un maillage triangulaire 3D contenant 29 coupes et 28 couches d'une épaisseur de 0,5m a été généré dans l'interface FEFLOW. Chaque coupe et couche de maillage est composée de 7335 éléments et 3737 nœuds, respectivement. De plus, l'élément minimal a une taille de 0,2 m. Le maillage 3D est composé de 205380 éléments et 108373 nœuds en tout. Les conditions limites d'écoulement et de transfert de chaleur doivent être définies de façon à reproduire avec exactitude l'expérience de traçage de la chaleur.

Les puits de pompage et d'injection ont été considérés comme des puits à couches multiples, de sorte que le débit est spécifié pour chaque couche en fonction de leur valeur de conductivité hydraulique. On a imposé des limites hydrauliques de type 1 (charges constantes) aux limites est et ouest du modèle afin de reproduire un gradient hydraulique de 3 mm/m représentant les conditions mesurées avant l'essai (Diersch, 2014). Une condition limite de type I (température constante) a également été imposée au puits d'injection.

Mesures d'ERT entre forages

L'un des principaux inconvénients des mesures ERT de surface est la diminution de la résolution avec la profondeur. C'est une limitation physique fondamentale qui ne peut être surmontée en reconfigurant la séquence d'acquisition de surface ou la modélisation numérique (Loke, 2013). Théoriquement, le seul moyen d'améliorer la résolution des données à une plus grande profondeur est de placer les électrodes (source et récepteur) plus près de l'objectif. Dans le cas

de notre projet, nous proposons de faire des mesures ERT entre forages. Des électrodes de puits sont introduites dans les forages pour effectuer des sondages ERT à la profondeur désirée.

Les configurations des électrodes dipôle-dipôle, triple pôle, pôle-dipôle, etc. ont été proposées pour réaliser une coupe ERT transversale au panache de chaleur. Les électrodes de fond de trou peuvent être configurées différemment pour les configurations de réseaux électriques. Il est important de noter que de nombreuses configurations peuvent être produites en réorganisant la position des électrodes sources et récepteur.

Chaque point de mesure (correspondant à un quadripôle) du protocole électrique de l'ERT est constitué des positions de deux paires d'électrodes de potentiel (P1-P2) et de courant (C1-C1). Le quadripôle réciproque est obtenu en changeant la position des électrodes de courant (P1-P2) avec les électrodes de potentiel (C1-C2). En théorie, la valeur mesurée par le quadripôle normal et réciproque devrait être identique en vertu du principe de réciprocité. Toutes différences entre elles représentent l'erreur réciproque qui sert de repère pour caractériser le modèle d'erreur de la mesure ERT. Nous avons suivi l'approche proposée par Binley et al. (1995) afin de créer une relation linéaire entre la résistivité apparente mesurée et l'erreur de mesure.

L'inversion électrique en suivi temporel

Il existe différentes stratégies pour faire une inversion électrique dans le temps. Le plus simple est l'inversion électrique indépendante, dans laquelle l'inversion est faite individuellement à chaque pas de temps de surveillance. Les résultats de deux temps successifs sont soustraits pour visualiser le changement de résistivité entre les deux pas de temps (Gunther and Ruckery, 2019; Günther, et al., 2006). Une autre stratégie est appelée inversion du ratio lorsque le ratio des données est calculé entre les deux pas de temps et inversé en résistivité apparente (Loke, 2001). Toutefois, cette approche n'est valable que pour les faibles contrastes de résistivité, car elle ne tient pas compte de la distribution de sensibilité en fonction du modèle réel (Loke, 2001).

La stratégie basée sur un modèle de référence est une autre stratégie de suivi temporel, où les modèles sont contraints de prendre soit le premier résultat d'inversion, soit le précédent comme modèle de référence pour l'inversion actuelle. Dans ce cas, les résultats d'inversion montrent le changement de résistivité (ratio) plutôt que leurs valeurs absolues (Loke, 2001).

Relation pétrophysique et modélisation directe électrique

Il existe une relation pétrophysique bien connue reliant la conductivité électrique et la température d'un fluide (Hayley, et al., 2007; Hermans, et al., 2012; Sen and Goode, 1992; Équation 2.2).

$$\frac{\sigma_{f,T}}{\sigma_{f,10.3}} = m_f(T - 10.3) + 1 \quad 2.2$$

Où $\sigma_{f,T}$ fait référence à la conductivité électrique de l'eau à la température T en °C et $\sigma_{f,10.3}$ est la conductivité électrique de l'eau à la température de base de 10.3 °C, m_f est le taux de variation de la conductivité électrique de l'eau pour changement d'unité de température. Étant donné que notre expérience est menée dans un aquifère de sable et gravier pendant une courte période de temps, les changements de température de la matrice sont négligeables. Par ailleurs, comme l'aquifère est un aquifère de sable et gravier, la conductivité électrique de surface est elle aussi négligeable. En conséquence, le changement mesuré de la conductivité électrique est censé refléter le changement de température du fluide interstitiel. La relation entre la conductivité électrique et de fluide interstitiel peut être dérivée à l'aide de la loi d'Archie (Archie, 2013).

$$\sigma_{f,T} = \frac{\sigma_{b,T}}{\sigma_{b,10.3}} \sigma_{f,10.3} \quad 2.3$$

Ici, $\sigma_{b,T}$ représente la conductivité électrique du fluide interstitiel à la température T et $\sigma_{b,10.3}$ est la conductivité électrique globale à la température de base de 10.3 °C.

Si nous insérons l'équation 2.2 dans l'équation 2.3 pour calculer la résistivité électrique globale en utilisant une distribution de température souterraine donnée à chaque pas de temps t .

$$\sigma_{b,T} = \sigma_{b,10.3}((T - 10.3)m_f + 1) \quad 2.4$$

Ici, T est une matrice 3D représentant la température à chaque nœud, où $\sigma_{b,T}$ représente la conductivité électrique brute.

Dans l'étape suivante, la modélisation directe électrique est effectuée sur les modèles de résistivité électrique pour estimer la résistivité apparente aux points de mesure réels.

La modélisation électrique directe est réalisée à l'aide de Resipy, un logiciel ouvert dont le code permet d'effectuer une modélisation électrique directe sur un modèle numérique 3D.

L'assimilation des données ERT

L'assimilation des données ERT est une approche efficace pour combiner le modèle numérique et les observations afin de produire un modèle mis à jour qui est plus représentatif de l'état du modèle que le modèle numérique et les observations (Camporese, et al., 2015). Evensen, (1994) a été le premier à formuler l'approche par EnKF ; cette méthode est une approximation de type Monte-Carlo du modèle traditionnel du filtre de Kalman (Kálmán, 1960). Dans notre étude,

l'ensemble fait référence aux 100 réalisations fournies en utilisant la simulation SGS non conditionnelle de conductivité hydraulique (K ; la variable à mettre à jour):

$$\mathbf{E} = \begin{bmatrix} \mathbf{x}_1 \\ \vdots \\ \mathbf{x}_n \end{bmatrix} \quad 2.20$$

L'EnKF consiste en la répétition de deux étapes principales, la prédition et l'analyse. Les deux étapes seront discutées par la suite.

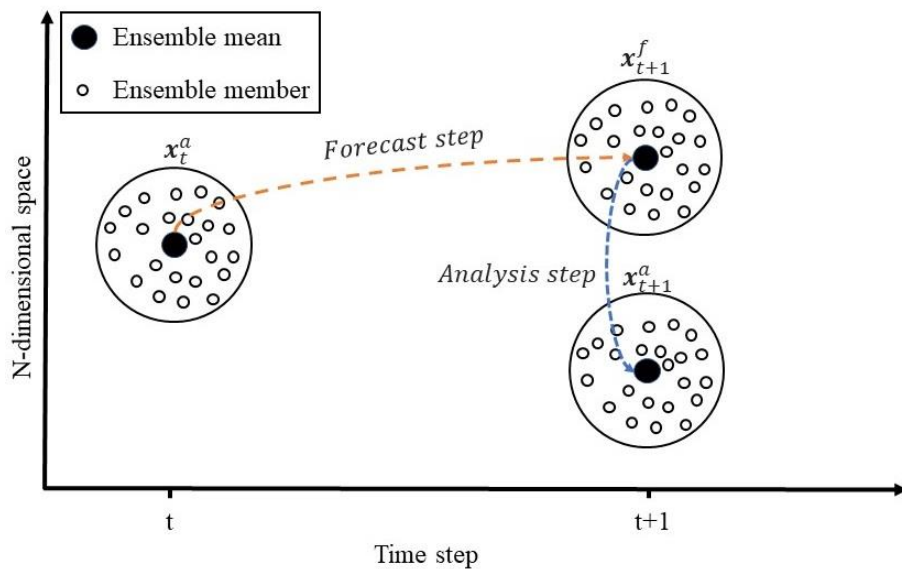


Figure 2.10 : Le schéma des étapes de prévision et d'analyse d'EnKF.

- Étape de prévision:

Soit un modèle transitoire pour le flux d'eau souterraine et le transfert thermique, l'ensemble de K est intégré dans le temps et la résistance électrique apparente est modélisée à chaque pas de temps de surveillance au moyen des équations 2.18 et 2.19.

$$\mathbf{X}_t^f = \mathbf{F}(\mathbf{X}_{t-1}^a) + \mathbf{q}_t \quad 2.18$$

$$\mathbf{Y}_t^o = \mathbf{H}(\mathbf{X}_t^f) + \mathbf{r}_t \quad 2.19$$

Où \mathbf{X}_t^f est l'ensemble de la distribution calculée de la température du sous-sol au temps t , F fait référence au modèle numérique de l'écoulement de l'eau souterraine et du transfert de chaleur, \mathbf{X}_{t-1}^a représente l'Ensemble de K mis à jour au temps $t-1$, il faut remarquer que \mathbf{X}_0^a (premier pas de temps $t=0$) est égal à l'ensemble initial de K , \mathbf{q}_t est l'erreur du modèle. La fonction ' H ' est la

fonction de modélisation électrique directe qui établit un lien entre K et la résistivité électrique apparente modélisée. Le terme \mathbf{Y}_t^o est la résistivité apparente modélisée au temps t qui est calculée en propageant l'ensemble de résistivité électrique apparente via la fonction de modélisation directe électrique (' \mathbf{H} '). \mathbf{r}_t fait référence à l'erreur de résistivité électrique apparente mesurée.

- Étape d'analyse

L'ensemble de K (\mathbf{E}_t^f) est initialisé à chaque pas de temps de surveillance à l'aide de l'équation suivante :

$$\mathbf{E}_t^a = \mathbf{E}_t^f + \bar{\mathbf{K}} \left\{ \mathbf{y}_t^{prd} - \mathbf{H}(\mathbf{E}_t^f) \right\} \quad 2.25$$

Ici, \mathbf{E}_t^a représente l'ensemble mis à jour de K au pas de temps t, $\bar{\mathbf{K}}$ est le gain de Kalman (KG) (Équation 2.27), \mathbf{y}_t^{prd} sont les mesures apparentes du champ de résistivité électrique au pas de temps de surveillance t. L'ensemble mis à jour de K au pas de temps t peut être vu comme une moyenne pondérée de \mathbf{E}_t^a et des mesures.

$$\bar{\mathbf{K}} = \bar{\mathbf{C}}_{err}^f \mathbf{H}^T \left(\mathbf{H} \bar{\mathbf{C}}_e^f \mathbf{H}^T + \mathbf{C}_{err}^m \right)^{-1} \quad 2.27$$

Ici $\bar{\mathbf{C}}_{err}^f$ représente la matrice de covariance d'erreur de \mathbf{E}_t^a , \mathbf{C}_{err}^m est la matrice de covariance d'erreur de mesures. Par conséquent, l'exactitude des résultats d'assimilation dépend de manière cruciale de l'estimation des deux matrices précédentes.

La taille limitée de l'ensemble peut générer une fausse corrélation sur de longues distances entre la variable d'état et l'observation qui se traduit par une fausse mise à jour de la variable d'état lors des étapes d'analyse de l'assimilation (Evensen, 2009). D'autre part, l'utilisation d'un ensemble de grande taille augmente considérablement le temps de calcul. Il faut donc faire un compromis entre la taille de l'ensemble et le temps de calcul afin d'obtenir des résultats qui ne divergent pas et un temps de calcul qui n'explose pas. La technique d'inflation de covariance multiplicative est une autre solution pour annuler l'effet de corrélation parasite où le modèle de covariance d'erreur de mesure est multiplié par un facteur d'inflation à chaque étape d'assimilation (Evensen, 2009; Wu and Zheng, 2017 [online]).

Résultats

Mesure d'ERT dans le temps.

Les mesures de l'ERT ont été effectuées dans une section formée des puits #2 et #4, qui est perpendiculaire à l'écoulement naturel des eaux souterraines. Les configurations de dipôle-dipôle, de pôle-dipôle et de pôle-tripôle ont été acquises pour effectuer le suivi temporel. Toutes les combinaisons possibles d'électrodes ont été prises en considération, sauf celles qui avaient deux électrodes de courant dans le même puits, car elles provoquent un court-circuit entre les électrodes de courant. Finalement, la séquence de mesure est constituée de 596 paires de quadripôles normaux et réciproques qui mettent environ 30 minutes à être acquise. En raison de la présence d'une couche argileuse au-dessus et au-dessous de l'aquifère, le temps de mesure pour chaque quadripôle a été établi à 500 millisecondes pour éliminer tout effet de polarisation induite (IP) sur les mesures de potentiel.

Les mesures ont été effectuées sur 11 étapes de temps au cours de 7 jours consécutifs. Tous les ensembles de données ont été filtrés en termes de valeurs aberrantes et d'erreurs réciproques avant de calculer la résistivité électrique apparente moyenne (Figure 3.3). La résistance électrique apparente moyenne pour l'ensemble de données de puits est de 42,55 ohm.m. Comme prévu, la résistivité apparente a diminué de 9 % pendant la phase d'injection d'eau chaude et commence à augmenter légèrement après la fin de l'injection de chaleur (phase de restitution thermique, Figure 3.3).

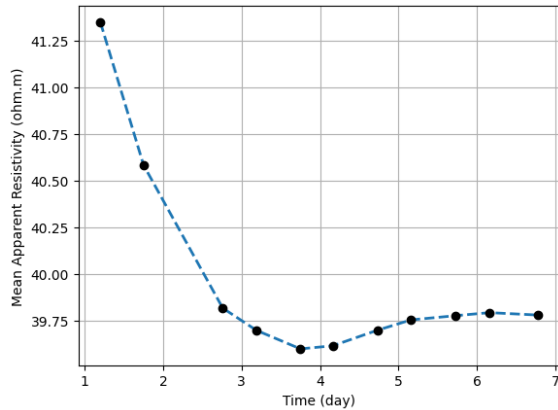


Figure 3.3 : La résistivité apparente moyenne (ohm.m) de chaque ensemble de données de pas de temps de suivi par rapport au temps après le début de l'expérience d'injection de chaleur.

L'estimation de l'erreur d'observation est essentielle pour l'approche d'assimilation des données, car l'exactitude des résultats est assujettie à ce paramètre (Wu and Zheng, 2017). Elle joue un rôle important dans le calcul des valeurs de perturbation des mesures et de la matrice de covariance des erreurs de mesure lors de l'étape d'assimilation. On considère le modèle d'erreur réciproque pour obtenir le modèle d'erreur de mesure (Binley, et al., 1995). Pour toutes les étapes

de la surveillance par ERT, chaque paire de mesures normales et réciproques a servi à créer un modèle d'erreur linéaire comme montré à la Figure 2.7.

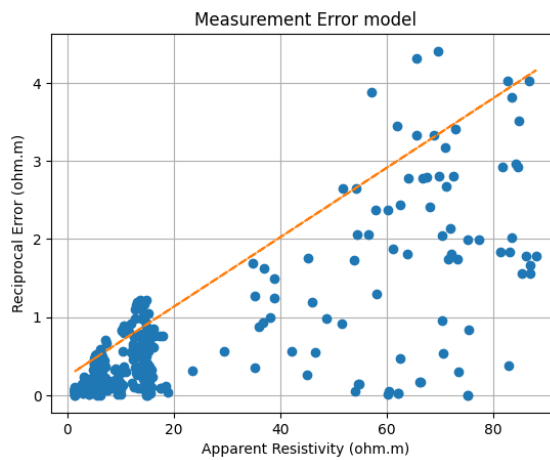


Figure 2.7 : La résistivité apparente est tracée en fonction des valeurs d'erreur réciproques pour créer un modèle d'erreur linéaire. Le modèle linéaire est utilisé pour prédire l'erreur de mesure pour chaque quadripôle.

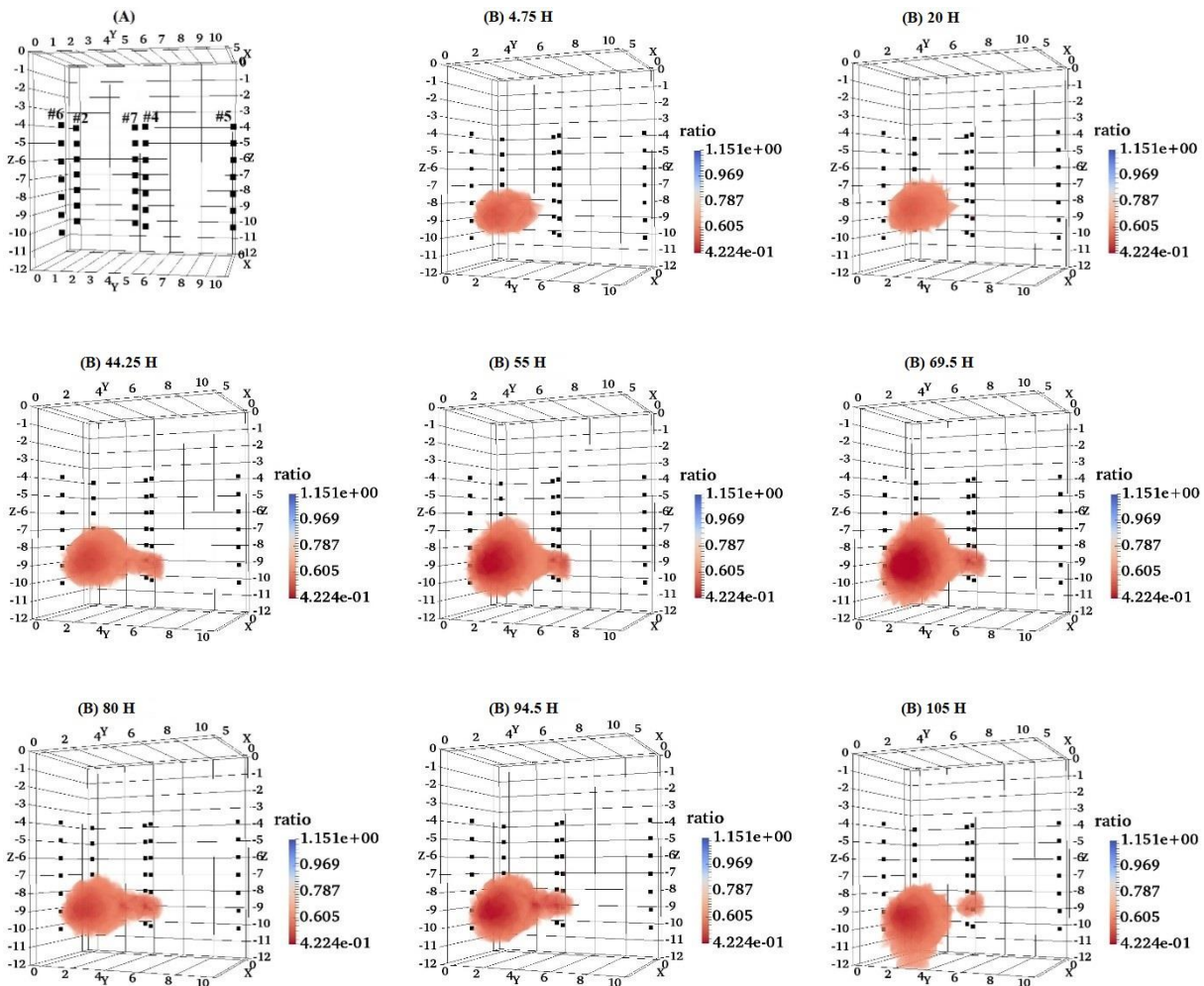
Par conséquent, une répartition des erreurs est fournie pour chaque pas de temps de surveillance, ce qui permet de générer des erreurs aléatoires pour perturber les mesures et créer une matrice de covariance des erreurs d'observation.

L'inversion électrique dans le temps

Avant de commencer l'assimilation, une inversion électrique dans le temps a été effectuée pour vérifier que les données d'ERT soient informatives sur l'évolution du panache d'eau chaude. L'inversion électrique dans le temps a été effectuée en utilisant le logiciel libre BERT (Gunther and Ruckery, 2019). L'inversion avec modèle de référence a été utilisée comme stratégie d'inversion (voir la section 2-5-4). La courbure maximale de type L-curve a été utilisée pour optimiser le coefficient de régularisation (Günther, et al., 2006).

Avant d'inverser les ensembles de données ERT, il est nécessaire de filtrer les mesures dont l'erreur réciproque est de plus de 10% de leur propre valeur. La Figure 3.4B présente les modèles inversés par intervalles de temps avec les données filtrées. La variation maximale de résistivité est observée au centre du panache de chaleur, où le ratio est égal à 0,4, selon le coefficient de variation de la conductivité électrique de l'eau par unité de changement de température (équation 2.2), la variation de résistivité correspond à une augmentation de 3,03 °C de la température souterraine. Il est facile de constater que la diminution de la résistivité/hausse de température est plus élevée au centre du panache qu'à l'avant. En ce qui concerne les résultats de l'inversion, le panache de chaleur s'étend pendant les deux premiers jours de l'injection de chaleur, puis rétrécit

légèrement pendant le temps de restitution thermique. En outre, le panache s'est largement répandu au fond de l'aquifère correspondant à une valeur de conductivité hydraulique plus élevée. Les résultats de l'inversion montrent que le panache se propage vers le puits #4 au bout de 41,5 heures. L'hypothèse géologique est que la profondeur correspondant à la plus grande quantité de gravier est au fond de l'aquifère et accélère le déplacement de la chaleur vers le puits #4; l'anomalie s'y maintient pendant 40 heures, puis elle commence à disparaître comme prévu pendant la phase de restitution thermique.



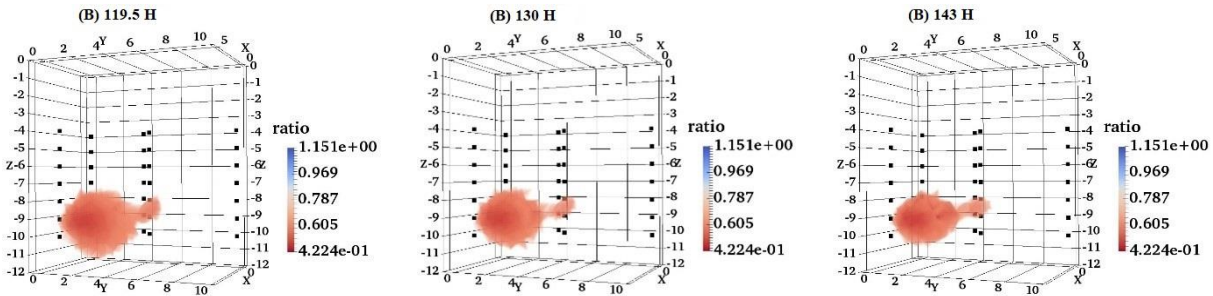
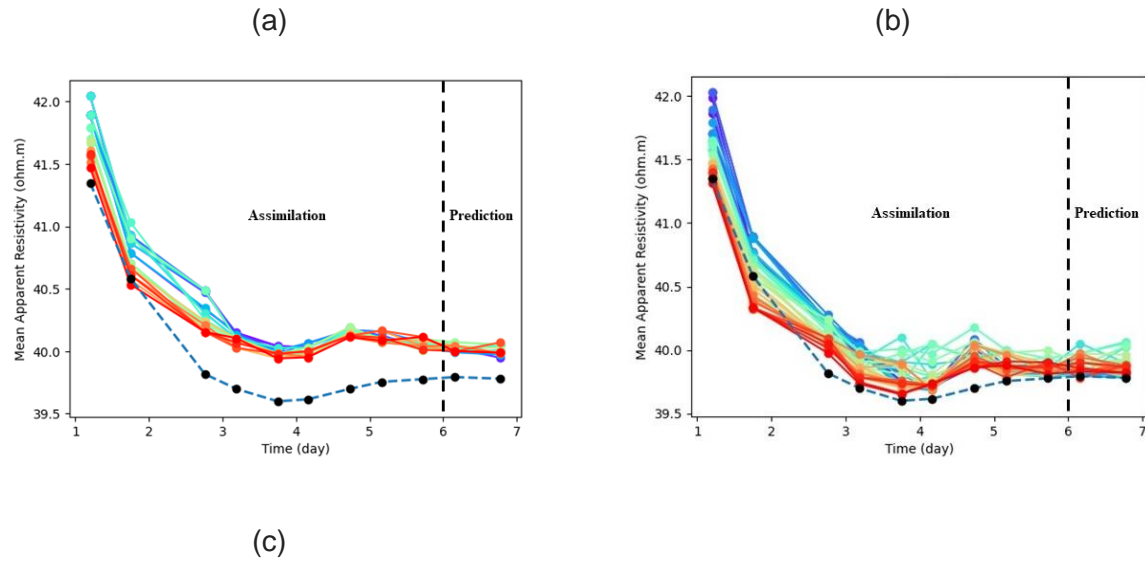


Figure 3.4 : A) Position des puits B) Les résultats d'inversion time-lapse du suivi d'ERT à 14 pas de temps. Chaque résultat représente le rapport entre le modèle de résistivité actuel et le modèle de résistivité de base. La ligne pointillée carrée marque la partie écran des puits de la profondeur de 24 à 30.

Assimilation et prédition des données de l'ERT

L'avantage des sondages en tomographie de résistivité entre forages par rapport aux mesures in situ, telles que le suivi de la température dans les puits, est de fournir une couverture spatiale étendue du sous-sol. C'est pourquoi la reproduction des données de ERT à chaque étape temporelle a été considérée comme les observations à reproduire pour notre expérience d'assimilation afin d'en assurer la qualité.



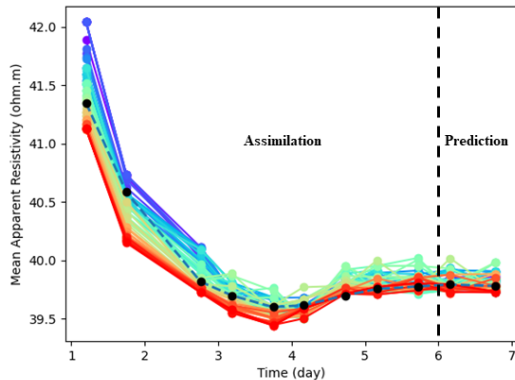


Figure 3.6 : La ligne pointillée représente la résistivité apparente moyenne des mesures sur le terrain. Les valeurs colorées sont des valeurs simulées par modélisation électrique directe pour chaque membre de l'ensemble en fonction du temps après le début de l'injection de chaleur. (a, b et c) montrent les mêmes informations pour 20, 40 et 60 membres de l'ensemble respectivement.

Nous avons mesuré 11 ensembles de données de ERT au cours des étapes d'injection de chaleur et de restitution thermique. Les ensembles de données d'observation ont été divisés en deux groupes pour évaluer l'exactitude de l'approche. Le premier concerne les neuf premiers pas de mesure et les deux derniers sont utilisés pour effectuer la prévision de l'état futur du système et ne sont pas utilisés lors de l'assimilation.

Les résultats sont présentés à la Figure 3.6, où nous montrons les moyennes mesurées et prévues des graphiques de résistivité apparente sur 11 étapes de temps pour diverses tailles d'ensemble. Il est simple de constater comment la taille de l'ensemble influe sur la précision des résultats (Figure 3.6).

En raison de la petite taille de l'ensemble, l'essai d'assimilation de 20 réalisations (Figure 3.6a) n'a pas réussi à trouver une solution réaliste. La variance a diminué de façon spectaculaire jusqu'au neuvième stade qui marque la fin de l'assimilation et l'état futur a été surestimé. La taille de l'ensemble a été augmentée à 40 réalisations (Figure 3.6b), ce qui a amélioré la qualité des résultats en termes de diminution de la variance, mais les prédictions n'ont pas convergé.

La Figure 3.6c montre les résultats pour un ensemble de 60 réalisations qui ont été sélectionnées comme la taille optimale de l'ensemble permettant d'éviter la divergence et l'effondrement de la variance et d'avoir un délai de calcul raisonnable. Le temps d'exécution est d'environ 72 heures pour assimiler un ensemble de 60 réalisations pour 11 étapes de temps de suivi.

Un point d'observation de température situé à 28 m de profondeur du puits #4 (Figure 1.11) est considéré dans le maillage de simulation du modèle numérique. La Figure 3.8 montre les températures simulées en fonction des mesures sur le terrain pendant l'injection et la période de

restitution à la même profondeur pour le puits #4. Même dans les deux premières étapes de suivi, les températures simulées ne convergent pas, mais dès la troisième étape, elles convergent vers la mesure de terrain.

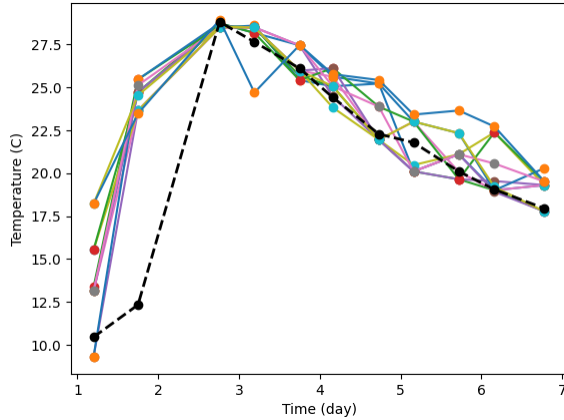


Figure 3.8 : La ligne de trait est la température mesurée à la profondeur de 28m du puits #4. Les lignes pleine de couleur représentent la température modélisée.

La distribution initiale et finale de K de l'ensemble est illustrée à la Figure 3.9. De plus, les valeurs de la moyenne et de l'écart-type (std) sont indiquées pour vérifier leur changement avant et après l'assimilation. La valeur std a été réduite au cours de l'expérience d'assimilation, mais elle n'a pas entraîné l'effondrement de la variance. Après neuf étapes d'assimilation des données ERT, la valeur moyenne de K a convergé vers la valeur de l'essai hydraulique in situ.

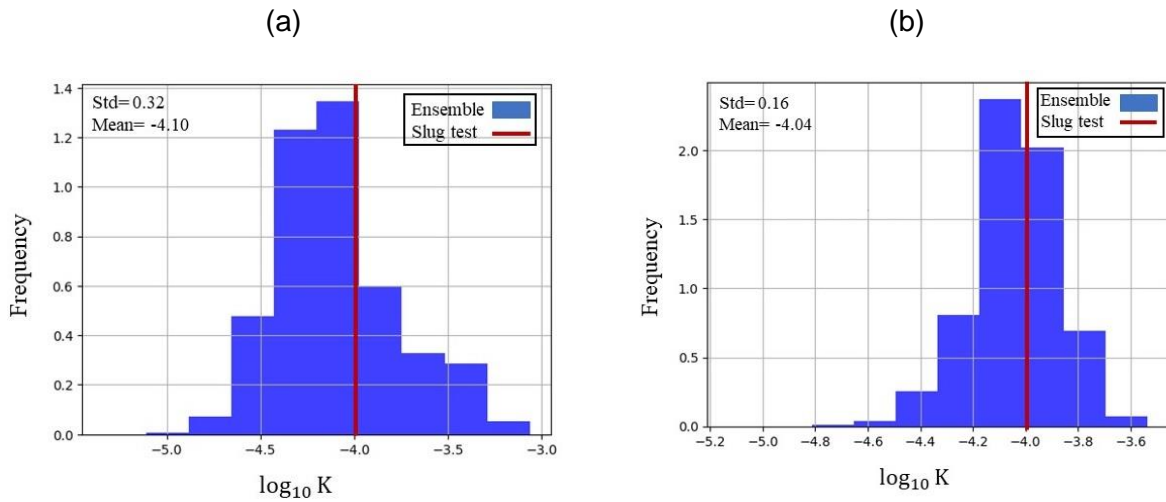
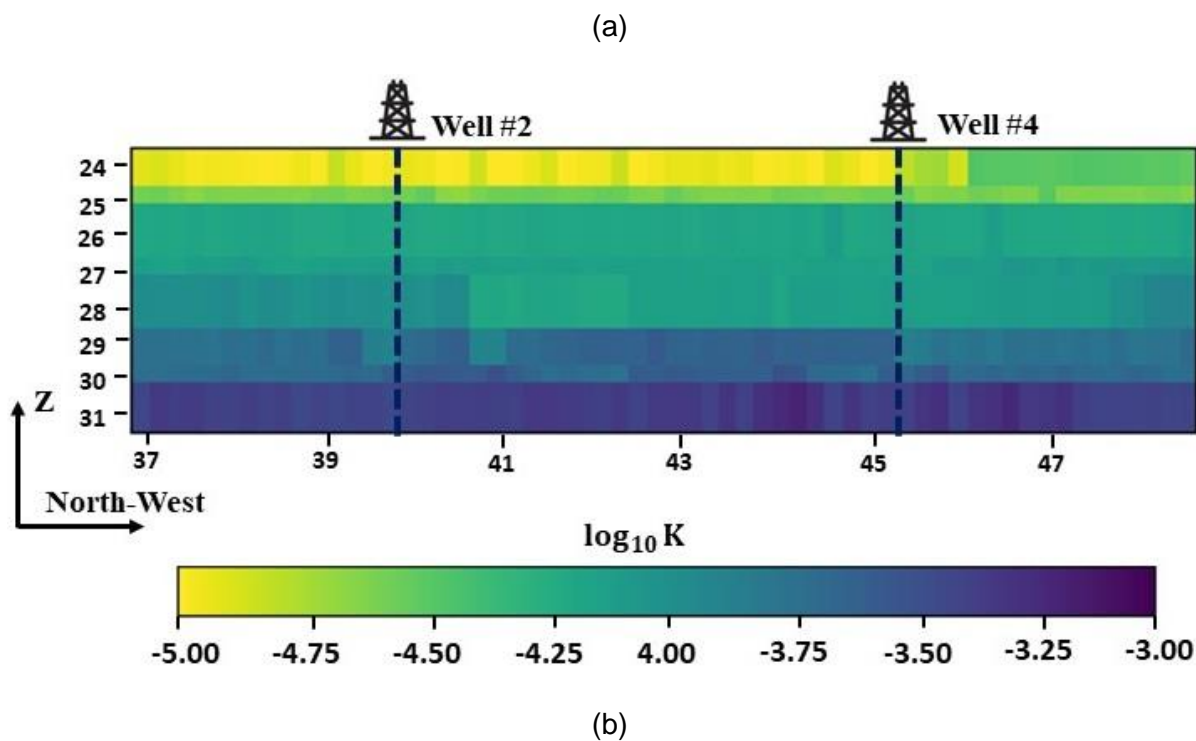
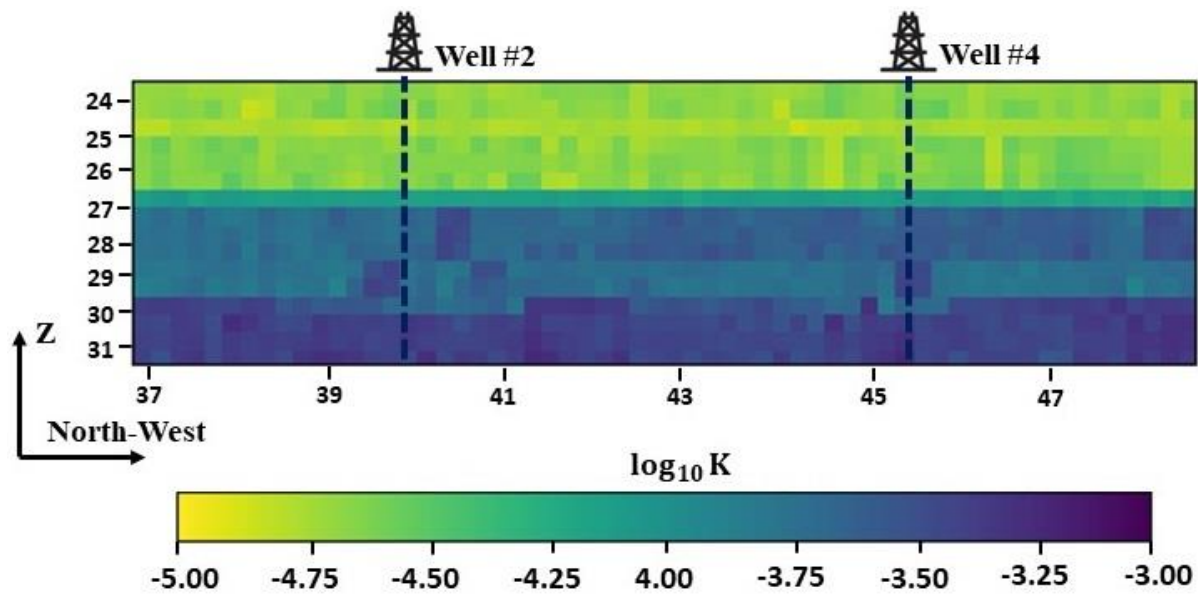


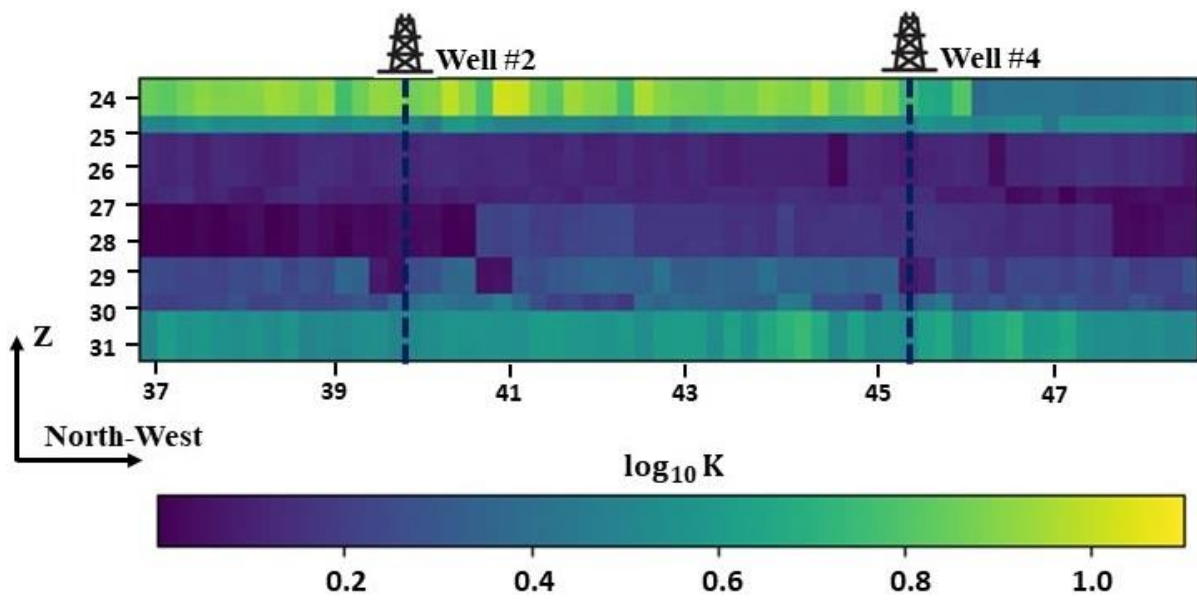
Figure 3.9 : a) Distribution initiale de la conductivité hydraulique de l'ensemble aléatoire avant le début de l'expérience d'assimilation. b) Distribution finale de la conductivité hydraulique pour le même membre de l'ensemble après les dernières étapes d'assimilation. La ligne rouge verticale marque la moyenne? des résultats des essais lugeons.

Les Figures 3.9a et b montrent la moyenne de K de l'ensemble avant et après l'assimilation dans la section transversale des puits #2 et #4, respectivement. Selon la Figure 3.10, la plage des valeurs de K dans la section après assimilation (b) est supérieure à la plage de K avant assimilation (a). Cela concorde avec les résultats de la Figure 3.9, où la moyenne de distribution de l'ensemble postérieur de K s'est déplacée vers des valeurs K plus élevées après neuf étapes d'assimilation. Il est à signaler que l'ensemble de départ a été généré par simulation non conditionnelle avec une variance forte, car nous n'avions qu'une valeur de K pour l'ensemble de l'espace crête (Figure 3.10a, Figure 3.1). Après neuf étapes d'assimilation des données de ERT, une zone avec des valeurs plus élevées de K apparaît à partir de la profondeur de 27 m au fond de l'aquifère. L'analyse de la diagraphe lithologique (Figure 1.11b) montre aussi une couche au fond de l'aquifère avec une plus grande quantité de gravier, vraisemblablement associé à une plus grande conductivité hydraulique. La différence entre la section avant et après assimilation a été calculée pour visualiser l'intensité de mise à jour de chaque pixel (Figure 3.10c). Les valeurs d'écart-type de l'ensemble K postérieur ont été tracées à la Figure 3.10d. Les valeurs d'écart-type ont une intensité moindre dans l'intervalle de 25 m à 30 m de section transversale où les électrodes de fond ont été montées. Il montre que le taux de convergence vers une estimation K non biaisée est plus élevé pour la zone qui a été couverte par les données ERT croisées.





(c)



(d)

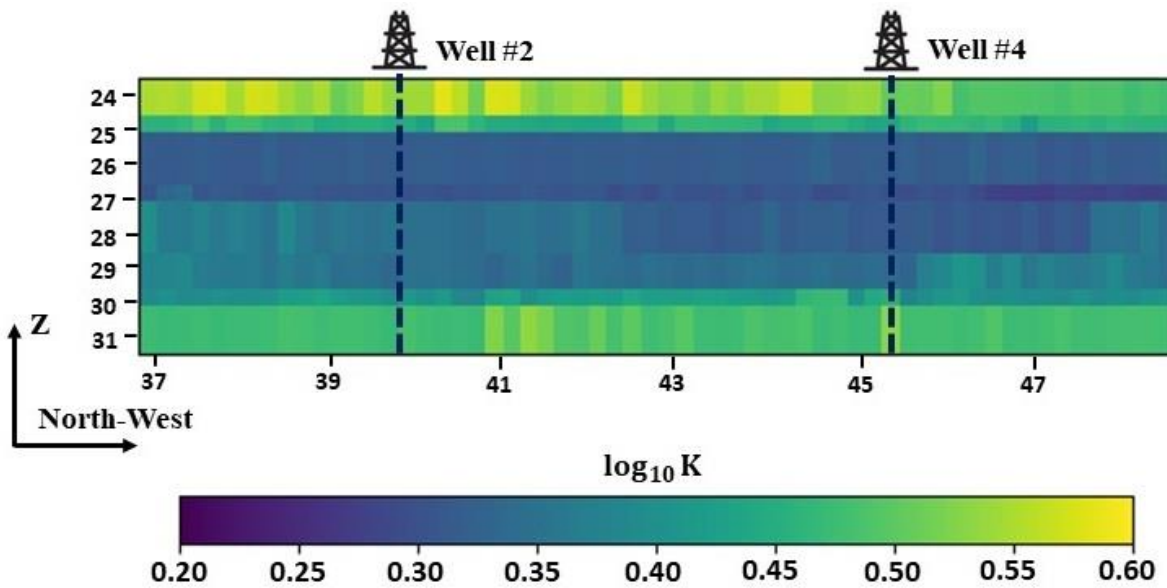


Figure 3.10 : Section transversale du puits 2 à 4. a) la distribution initiale de la conductibilité hydraulique. b) distribution de la conductivité hydraulique après la dernière étape d'assimilation. c) le décalage entre la section transversale a et b qui montre les valeurs mises à jour lors de l'expérience d'assimilation. d) L'écart-type de la distribution K postérieure à chaque pixel de section transversale a été montré. La taille de pixel est de 0,5 m par 0,2 m le long des axes Z et X, respectivement.

Conclusions

Les observations de l'ERT sont des mesures indirectes et à faible coût permettant d'obtenir des données sensibles aux changements de température. Elles sont utiles pour les expériences d'assimilation de données en hydrogéophysique, car elles fournissent des données à haute résolution spatiale et temporelle sensibles à des changements de l'état des aquifères. Dans ce projet, nous avons utilisé des outils d'assimilation de données afin de mettre à jour la répartition spatiale de la conductivité hydraulique d'un aquifère de sable graveleux peu profond dans le cadre d'une expérience de traçage thermique. La comparaison entre les valeurs de résistivité électrique modélisées et mesurées est en accord, confirmant la fiabilité de la méthode. Par ailleurs, des mesures de la température ont été comparées avec celles estimées par notre méthode. Elles convergent après deux pas d'assimilation.

Finalement, nous avons montré que l'assimilation de données ERT dans un modèle hydrogéologique avec une expérience de traçage thermique est un outil efficace qui peut fournir une meilleure caractérisation des propriétés hydrauliques de l'aquifère qui sont essentielles dans le processus de conception de pompes à chaleur d'aquifère. En outre, cette méthode peut être considérée comme une approche puissante pour évaluer l'incertitude relative à la distribution hétérogène des propriétés hydrauliques du sous-sol. La comparaison entre les fonctions de

densité de vraisemblance initiale et finale et la distribution de la conductivité hydraulique inférée avec les essais de terrain confirme que l'approche proposée permet de corriger adéquatement l'ensemble de départ, même si celui-ci est légèrement biaisé.

TABLE OF CONTENT

AKNOWLEDGEMENT.....	III
RÉSUMÉ	V
ABSTRACT.....	VII
SOMMAIRE RÉCAPITULATIF.....	IX
TABLE OF CONTENT	XXXIII
LIST OF FIGURES	XXXV
LIST OF TABLES	XXXIX
LIST OF EQUATIONS	XLI
LIST OF ABBREVIATION AND NOMENCLATURE	XLIII
1 INTRODUCTION	1
1.1 GLOBAL WARMING PROBLEM	1
1.2 RESIDENTIAL AND COMMERCIAL BUILDING CARBON FOOTPRINT	3
1.3 GROUND SOURCE COOLING/HEATING SYSTEM	5
1.4 GROUNDWATER HEAT PUMP SYSTEM	6
1.5 SUBSURFACE CHARACTERIZATION.....	7
1.6 OBJECTIVES.....	10
1.7 CONTRIBUTION.....	10
1.8 PROJECT'S CONTEXT	11
1.9 EXPERIMENTAL SITE	12
1.9.1 <i>Hydrogeological background</i>	12
1.9.2 <i>Field setup</i>	15
1.9.3 <i>Theoretical background</i>	21
2 METHODOLOGY	25
2.1 WORKFLOW	25
2.2 NUMERICAL MODEL OF GROUNDWATER FLOW AND HEAT TRANSFER	26
2.2.1 <i>Define a mesh</i>	26
2.2.2 <i>Material properties</i>	28
2.2.3 <i>Initial condition</i>	29
2.2.4 <i>Boundary condition</i>	30
2.3 TIME-LAPSE ELECTRICAL RESISTIVITY TOMOGRAPHY.....	31
2.3.1 <i>Petrophysical relationship and forward modeling</i>	31
2.3.2 <i>Cross-borehole ERT array</i>	33
2.3.3 <i>Error model of ERT measurements</i>	37
2.3.4 <i>Time-lapse electrical inversion of DC resistivity data</i>	38
2.4 DATA ASSIMILATION	40

2.4.1	<i>Bayes' rule</i>	40
2.4.2	<i>Monte Carlo simulation</i>	41
2.4.3	<i>Ensemble Kalman filter</i>	42
3	RESULTS	49
3.1	GEOSTATISTICAL SIMULATIONS.....	49
3.2	CROSS-BOREHOLE ERT MEASUREMENTS.....	49
3.2.1	<i>Evaluation of cross-borehole ERT monitoring data</i>	50
3.3	MODEL OF MEASUREMENT ERROR	52
3.4	ASSIMILATION RESULTS.....	53
4	DISCUSSION	63
5	CONCLUSIONS	67
6	REFERENCES	69

LIST OF FIGURES

FIGURE 1.1 : THE GLOBAL CONCENTRATION OF THREE MAJORS GHGS ARE PLOTTED BASED ON NOAA GLOBAL AIR SAMPLING NETWORK DATA SINCE 1979 (BRUHWILER, ET AL., 2021).....	2
FIGURE 1.2 : THE OBSERVED AND PREDICTED GLOBAL CONCENTRATION OF CO₂ IN ATMOSPHERE SINCE 1750 (INDUSTRIAL ERA) (EUROPEAN ENVIRONMENT AGENCY, 1993).....	3
FIGURE 1.3 : A) THE GLOBAL TEMPERATURE ANOMALY SINCE 1880. B) THE GLOBAL SEA HEIGHT VARIATION SINCE 1995 (SOURCE: CLIMATE NASA.GOV).....	3
FIGURE 1.4 : A & B) CO₂ EMISSION BY RESIDENTIAL AND COMMERCIAL BUILDING. C) A COMPARISON BETWEEN DIFFERENT HEATING TECHNOLOGY IN TERM OF ENERGY COST AND LEVEL OF CARBON EMISSION (LEUNG, 2018; MAIDMENT, 2013).	5
FIGURE 1.5 : THE SCHEMATIC OF A TYPICAL GROUND-COUPLED HEAT PUMP SYSTEM CONFIGURATION IN COOLING (A) AND HEATING (B) MODE (MAIDMENT, 2013).....	6
FIGURE 1.6 : THE GWHP SYSTEM CONFIGURATION. A) DISCHARGING TO SURFACE WATER BODIES. B) THE OPEN LOOP SYSTEMS WITH AQUIFER RE-INJECTION (LADISLAUS, 2001).....	7
FIGURE 1.7 : HYDRO-STRATIGRAPHIC CROSS-SECTION C-C'. THE CROSS-SECTION ILLUSTRATES THE PROTO-SAINTE-LAURENT DELTA THAT INCLUDE THE HYDRO-STRATIGRAPHIC EXIST AT THE BASE OF QUEBEC CITY (TALBOT POULIN, ET AL., 2013).	13
FIGURE 1.8 : THE THICKNESS OF THE DELTAIC AQUIFER IN QUEBEC CITY AREA (LAMARCHE, 2011). THE RED CIRCLE INDICATES THE EXPERIMENTAL SITE LOCATION.	14
FIGURE 1.9 : THE VULNERABILITY OF POPULATION TO HEAT WAVE IN QUEBEC CITY AREA. THE YELLOW LINE MARKS THE DELTAIC SANDY AQUIFER EXTENSION AROUND QUEBEC CITY (BARETTE ET AL., 2018). THE RED CIRCLE INDICATES THE EXPERIMENTAL SITE LOCATION.	15
FIGURE 1.10 : A) THE EXPERIMENTAL SITE IS NEAR THE BAIE DE BEAUPORT, NORTHERN SHORE OF THE ST-LAWRENCE RIVER, QUEBEC CITY, CANADA. B) HEAT-TRACING EQUIPMENT SETUP AT THE SITE, AND LOCATION OF PUMPING, INJECTION, AND OBSERVATION WELLS. THE POSITION OF PUMPING, INJECTION AND THREE ERT MONITORING WELLS, DOWNHOLE CABLE RUN INTO THE BOTTOM OF WELL #2 AND #4, WATER HEATER WAS INSTALLED IN TRAILER.....	16
FIGURE 1.11 : A) THE CONFIGURATION OF THE PUMPING, INJECTION AND ERT MONITORING WELLS B) INTERPRETED LITHOLOGICAL UNITS USING CPT LOGS IN WELL #2 AND SCHEME OF THE INSTALLED WELL CASING.	17
FIGURE 1.12 : GROUNDWATER TEMPERATURE PROFILE MEASURED IN WELL #2.	18
FIGURE 1.13 : THE TRT ANALYSIS PLOTS. A) INJECTION PERIOD B) RECOVERY PERIOD.....	19

FIGURE 1.14 : THE PLOT SHOWS THE ONE OF THE AIR- PRESSURIZED SLUG TEST ANALYSES PERFORMED IN THE WELL#2.....	20
FIGURE 2.1 : THE WORKFLOW SHOWS THE IMPLEMENTATION OF TIME-LAPSE CROSS-BOREHOLE ERT DATA ASSIMILATION TO CALIBRATE SUBSURFACE 3D DISTRIBUTION OF K. THE LETTER N REFERS TO THE NUMBER OF MONITORING TIME STEPS.....	26
FIGURE 2.2 : A) SUPER MESH ILLUSTRATING THE WELL LOCATION AND EXTENSION OF MODEL DOMAIN. B) DEFINE 2D MESH PARAMETERS. C) 2D TRIANGULAR MESH D) 3D MESH WITH VERTICAL RESOLUTION OF 0.5 M.....	28
FIGURE 2.3 : THE INITIAL HYDRAULIC HEAD IS THE RESULT OF A STEADY STATE SIMULATION.	30
FIGURE 2.4 : THE LINEAR RELATIONSHIP BETWEEN WATER ELECTRICAL CONDUCTIVITY AND TEMPERATURE, THIS RELATIONSHIP IS USED TO DETERMINE THE BULK ELECTRICAL CONDUCTIVITY USING ARCHIE'S LAW (HERMANS, ET AL., 2015).....	32
FIGURE 2.5 : THE PLOT ILLUSTRATES 4 TYPES OF CROSS-BOREHOLES ERT ARRAYS. A) DIPOLE-DIPOLE B) TRIPOLE-POLE C) POLE-DIPOLE D) POLE-POLE. AT EACH MEASURING TIME-STEP, THE ELECTRODE(S) IN THE LEFT BOREHOLE ARE FREEZE AT THEIR LOCATION AND ELECTRODE(S) IN THE RIGHT BOREHOLE MOVE FROM TOP TO THE BOTTOM OF BOREHOLE.	34
FIGURE 2.6 : THE SENSITIVITY PATTERN OF TWO, THREE AND FOUR-ELECTRODE ARRAY. A & B) THE SENSITIVITY PATTERN OF POLE-POLE ARRAY. C & D) THE SENSITIVITY PATTERN OF DIPOLE-POLE ARRAY. E & F) THE SENSITIVITY PATTERN OF DIPOLE-DIPOLE ARRAY, IN THIS CONFIGURATION THE C1 AND P1 LOCATED IN ONE BOREHOLE, C2 AND P2 ARE IN OTHER BOREHOLES. COMPARISON BETWEEN THE SECTION OF (E) AND (F) ILLUSTRATES THAT DECREASING P1-C1 AND P2-C2 SPACING INCREASE THE POSITIVE SENSITIVITY QUANTITY BETWEEN BOREHOLES (LOKE, 2013).	37
FIGURE 2.7 : THE APPARENT RESISTIVITY IS PLOTTED VERSUS RECIPROCAL ERROR VALUES TO MAKE A LINEAR ERROR MODEL. THE LINEAR MODEL IS UTILIZED TO PREDICT MEASUREMENT ERROR FOR EACH QUADRUPOLE.	38
FIGURE 2.8 : THE SCHEMATIC OF BAYES' RULE. THE MULTIPLICATION OF PRIOR AND DATA RESULTS IN A DISTRIBUTION THAT HAS LESS VARIANCE THAN BOTH INITIAL PROBABILITY DISTRIBUTIONS.....	41
FIGURE 2.9 : THE FLOWCHART OF MONT CARLO SIMULATION.	42
FIGURE 2.10 : THE SCHEMATIC OF FORECAST AND ANALYSIS STEPS OF ENKF.....	44
FIGURE 3.1 : THE 3D DISTRIBUTION OF SANDY GRAVEL AQUIFER HYDRAULIC CONDUCTIVITIES (LOG10 K [M/S]) PROVIDED BY SGS. THE LOCATION OF PUMPING (WELL#4) AND INJECTION (WELL#2) WELL WAS SHOWN.	49
FIGURE 3.2 : THE UPSIDE-DOWN RED TRIANGLES REPRESENT THE LOCATION OF DOWNHOLE ELECTRODES AND BLACK CIRCLES IN THE MIDDLE OF PANEL ARE CROSS-BOREHOLE ERT MEASURING POINTS. THE PLOT WAS PREPARED USING ELECTRE-PRO SOFTWARE (TRUFFERT, 1990).	50

FIGURE 3.3 : THE MEAN APPARENT RESISTIVITY (OHM.M) OF EACH ERT MONITORING TIME-STEP DATASET VERSUS THE TIME AFTER THE BEGINNING OF HEAT INJECTION EXPERIMENT.....	51
FIGURE 3.4 : A) POSITION OF WELLS B) THE TIME-LAPSE INVERSION RESULTS OF 14 TIME-STEP ERT MONITORING. EACH RESULT REPRESENTS THE RATIO OF CURRENT TIME-STEP RESISTIVITY MODEL AND THE BASE-LINE RESISTIVITY MODEL. SQUARE DASH LINE MARKS THE SCREEN PART OF WELLS FROM THE DEPTH OF 24 M TO 30 M.....	52
FIGURE 3.5 : THE COLORED CIRCLES REPRESENT FIVE MEASURED APPARENT RESISTIVITY DATASET VERSUS RECIPROCAL ERROR IN DIFFERENT COLORS. THE FITTED LINES ARE LINEAR ERROR MODEL. THE LINEAR ERROR MODEL IS USED TO PREDICT MEASUREMENT ERROR FOR EACH QUADRUPLE IN CROSS-BOREHOLE ERT ARRAY...	53
FIGURE 3.6 : THE DASH LINE REPRESENTS MEAN APPARENT RESISTIVITY OF FIELD MEASUREMENTS. THE COLORED ONES ARE SIMULATED VALUES BY ELECTRICAL FORWARD MODELING FOR EACH ENSEMBLE MEMBER VERSUS TIME AFTER THE BEGINNING OF HEAT INJECTION. (A, B AND C) DEMONSTRATE THE SAME INFORMATION FOR 20, 40 AND 60 ENSEMBLE MEMBERS RESPECTIVELY.....	55
FIGURE 3.7 : THE AVERAGE SIMULATED TEMPERATURE OF SIXTY REALIZATIONS IN CROSS-SECTION OF WELL #2 AND WELL #4 FOR ALL ASSIMILATION TIME-STEPS.....	57
FIGURE 3.8 : DASH LINE IS THE MEASURED TEMPERATURE AT THE DEPTH 28 M OF WELL#4. THE COLORED SOLID LINES REPRESENT THE SIMULATED GROUNDWATER TEMPERATURE OF SIXTY REALIZATIONS AT THE DEPTH 28 M OF WELL#4.....	58
FIGURE 3.9 : A) INITIAL K DISTRIBUTION OF ENSEMBLE BEFORE THE BEGINNING OF THE ASSIMILATION EXPERIMENT. B) POSTERIOR K ENSEMBLE DISTRIBUTION AFTER NINE ASSIMILATION STEPS. THE VERTICAL RED LINE MARKS THE GEOMETRIC MEAN OF SLUG TESTS RESULT.....	58
FIGURE 3.10 : THE CROSS-SECTION BETWEEN WELL #2 AND WELL #4. A) INITIAL K DISTRIBUTION. B) K DISTRIBUTION AFTER LAST ASSIMILATION STEP. C) THE MISFIT BETWEEN CROSS-SECTION A AND B WHICH SHOWS THE UPDATED VALUES DURING ASSIMILATION EXPERIMENT. D) STANDARD DEVIATION OF POSTERIOR K DISTRIBUTION AT EACH PIXEL OF CROSS-SECTION WAS MAPPED. EACH PIXEL SIZE IS 0.5 M BY 0.2 M ALONG Z AND X AXIS RESPECTIVELY.....	61

LIST OF TABLES

TABLE 1.1 : THE WELLS CHARACTERIZATION.....	17
TABLE 1.2 : THE RESULTS OF TWO TRT PERFORMED IN WELL #4 AND WELL #6. THE INTERPRETED THERMAL CONDUCTIVITY IN WELL #6 APPEARED MORE RELIABLE.....	18
TABLE 1.3 : THE THERMAL CONDUCTIVITY CALCULATED AT 28 M IN WELL #6 BASED ON THE TRT ANALYSIS FOR BOTH HEAT INJECTION AND RECOVERY.....	20
TABLE 1.4 : THE RANGE OF K ESTIMATED BY SLUG TEST. THE SLUG TEST WAS PERFORMED IN WELL #2.....	20
TABLE 2.1 : SUMMARY OF K OF LITHOSTRATIGRAPHIC UNITS (HWANG, ET AL., 2017; TALBOT POULIN, ET AL., 2013).....	28
TABLE 2.2 : THE TABLE OF MATERIAL PROPERTIES (TALBOT POULIN, ET AL., 2013).....	29
TABLE 2.3 : PUMPING AND INJECTION RATE TIME-SERIES.....	30
TABLE 2.4 : THE TIME-SERIES OF INJECTED WATER TEMPERATURE.....	30

LIST OF EQUATIONS

EQUATION 1.1	8
EQUATION 1.2	8
EQUATION 1.3	9
EQUATION 1.4	21
EQUATION 1.5	21
EQUATION 1.6	21
EQUATION 1.7	21
EQUATION 1.8	22
EQUATION 1.9	22
EQUATION 1.10	22
EQUATION 1.11	22
EQUATION 1.12	23
EQUATION 1.13	23
EQUATION 2.1	31
EQUATION 2.2	32
EQUATION 2.3	32
EQUATION 2.4	32
EQUATION 2.5	33
EQUATION 2.6	33
EQUATION 2.7	35
EQUATION 2.8	38
EQUATION 2.9	39
EQUATION 2.10	39
EQUATION 2.11	39
EQUATION 2.12	40
EQUATION 2.13	41

EQUATION 2.14	41
EQUATION 2.15	41
EQUATION 2.16	42
EQUATION 2.17	42
EQUATION 2.18	43
EQUATION 2.19	43
EQUATION 2.20	43
EQUATION 2.21	44
EQUATION 2.22	45
EQUATION 2.23	45
EQUATION 2.24	45
EQUATION 2.25	45
EQUATION 2.26	45
EQUATION 2.27	46
EQUATION 2.28	46
EQUATION 2.29	46
EQUATION 2.30	46
EQUATION 2.31	46
EQUATION 2.32	46
EQUATION 2.33	47

LIST OF ABBREVIATION AND NOMENCLATURE

Abbreviations:

BC	Boundary condition
CPT	Cone penetration test
DA	Data assimilation
DC	Direct current
EnKF	Ensemble Kalman filter
ERT	Electrical resistivity tomography
GHGs	Greenhouse gases
GHPs	Geothermal heat pump systems
GSHP	Ground source heat pump
GWHP	Groundwater heat pump system
IPCC	Intergovernmental Panel on Climate Change
ILS	Infinite Linear Source
KF	Kalman filter
LT	Low temperature
QMC	Quebec Metropolitan Community
SGE	Shallow geothermal energy
SGS	Sequential gaussian simulation
SPC	Specific point condition
TRT	Thermal response test

Nomenclature:

Roman Letters	
A	Anomaly of state
B	Aquifer thickness (m)

C	Covariance matrix
c_f	Specific heat of the fluid ($J \cdot kg^{-1} \cdot K^{-1}$)
D_{err}^m	iid sample from a white Gaussian error
d	Data in electrical forward modeling
E	Ensemble (a set of realizations)
Exp	Expectation function
E_{rp}	Reciprocal error (ohm.m)
Err	Error
e	Gravitational unit vector
F	Forecast operator
F	Formation factor
F^*	Physical model
f^B	Bottom bounding surface of aquifer (m)
f_μ	Viscosity relation function of liquid
g	Gravitational acceleration ($m \cdot s^{-2}$)
H	Length of the borehole (m)
H	Observational operator
h	Hydraulic head (m)
I	Electrical current (amp)
J	Jacobian matrix
K	Hydraulic conductivity ($m \cdot s^{-1}$)
\bar{K}	Kalman gain
L_w	Total length liquid-filled borehole (m)
m	Parameters in electrical forward modeling
m_f	Slope of fitted line for the increase in electrical conductivity per unit $^{\circ}\text{C}$
N	Ensemble size

Q_h	Flow supply term ($\text{m}^3 \cdot \text{s}^{-1}$)
Q_{hw}	Flow well-type specific point condition ($\text{m}^3 \cdot \text{s}^{-1}$)
Q_T	Heat supply term ($\text{W} \cdot \text{m}^{-2}$), , is the
Q_{Tw}	Well-type specific point condition term ($\text{W} \cdot \text{m}^{-2}$)
Q_w	Total pumping rate ($\text{m}^3 \cdot \text{s}^{-1}$)
\mathbf{q}	Darcy velocity ($\text{m} \cdot \text{s}^{-1}$)
\mathbf{q}_t	Forecast error vector
$\bar{\mathbf{q}}$	Depth-integrated Darcy velocity ($\text{m} \cdot \text{s}^{-1}$)
R	Radius of well casing and screen(s) (m).
R	Measured apparent resistivity (ohm.m)
R	Roughness matrix
r_t	Observational error vector
$\vec{r} = (x, y, z)$	Vector of Cartesian coordinates (m)
$\vec{r}_s(x_s, y_s, z_s)$	Electrical current source location (m)
P	Probability function
S	Sensitivity function
S_0	The specific storage coefficient (m^{-1})
s	Saturation
T	Temperature ($^\circ\text{C}$)
T_0	Background temperature ($^\circ\text{C}$)
T_f	Temperature of fluid phase ($^\circ\text{C}$)
T_s	Temperature of solid phase ($^\circ\text{C}$)
t	Time (s)
t_{off}	End time for the heat injection (s)
$\mathbf{V}(\vec{r})$	Distribution of electrical potential (volt)
\mathbf{W}_d	Data weight matrix

X	Unknown system state
x	Expected values for a specific location of the simulation domain
Y	Prior knowledge of the system (observations)
Y_a	Anomaly of observation
Greek Letters	
α	Regularization (or smoothing) parameter
γ	Euler's number
γ	Compressibility of liquid (psi^{-1})
$\delta()$	Dirac delta function
ε_e	specific yield
θ	Porosity
λ_f	Thermal conductivity of fluid phase ($\text{W.m}^{-1}\text{K}^{-1}$)
λ_{eff}	Effective thermal conductivity ($\text{W.m}^{-1}\text{K}^{-1}$)
λ_s	Thermal conductivity of solid ($\text{W.m}^{-1}\text{K}^{-1}$)
μ_0	Reference viscosity of liquid (Pa.s).
ρ	Electrical resistivity (Amp)
ρ_0	Reference density of liquid (kg.m^{-3})
$\rho_f c_f$	Fluid volumetric heat capacity ($\text{J.K}^{-1}.\text{m}^{-3}$)
$\rho_s c_s$	Solid volumetric heat capacity ($\text{J.K}^{-1}.\text{m}^{-3}$)
$\rho' c'$	Effective volumetric heat capacity ($\text{J.K}^{-1}.\text{m}^{-3}$)
σ_b	Bulk electrical conductivity (S.m^{-1})
σ_f	Fluid electrical conductivity (S.m^{-1})
χ	Buoyancy coefficient
∇T	Gradient of temperature °C
Subscript	
b	bulk

D	Dirichlet-type boundary
d	Data
e	Effective
err	Error
f	Fluid
i	i th row
j	j th column
m	Parameter
ref	Reference
rp	Reciprocal
s	Solid
T	Temperature
w	Borehole
Superscript	
a	Analyzed
an	Anomaly
f	Forecasted
m	Measurement
o	Observation
prd	Perturbed
T	Transpose

1 INTRODUCTION

The recent global warming is generally attributed to the increased level of greenhouse gases such as carbon dioxide (CO_2), methane (CH_4) and nitrous oxide (N_2O) etc. in the Earth's atmosphere (Rossati, 2017). Our carbon footprint needs to be reduced by cutting down our fossil fuels consumption. One solution is to install a low-emission geothermal heat pumps as cooling and heating systems in buildings (Raymond, 2018). In the following subsection, we will discuss about the global warming problem. It is followed by presenting an EnKF implementation in hydrogeology as a robust approach to better characterize subsurface hydraulic conductivity (K) which will help to design a geothermal heat pump system optimally.

1.1 Global warming problem

Global warming is one of the most challenging scientific issues of the 21st century, affecting different aspects of our global society. The global warming is not just a scientific problem, but it has changed different aspects of our life such as economics, sociology, geopolitics, and individual's lifestyle (Maslin, 2004). The Earth's temperature is controlled by the energy balance between the solar energy gained and the loss of this energy is returned to space. GHGs are the reason for capturing solar energy into the atmosphere and warming our planet (Maslin, 2004).

The increasing concentration of greenhouse gases (GHGs) such as carbon dioxide (CO_2), methane (CH_4) and nitrous oxide (N_2O) in the atmosphere (Figure 1.1) has significantly perturbed the energy balance of the climate system (Bruhwiler, et al., 2021). This is mostly related to fossil fuels consumption to supply energy, agricultural activities, and deforestation.

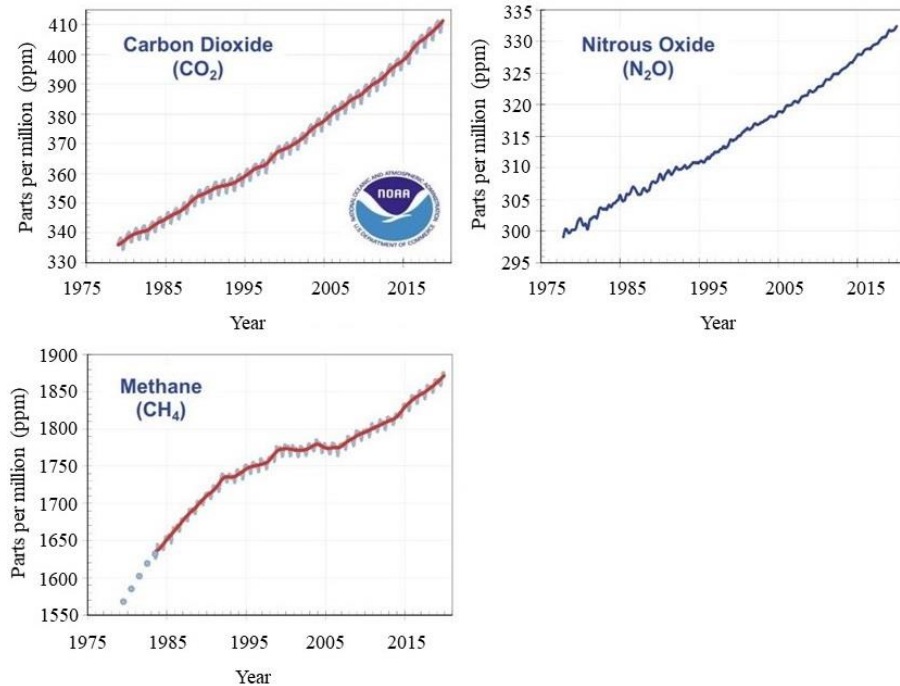


Figure 1.1 : The global concentration of three majors GHGs are plotted based on NOAA global air sampling network data since 1979 (Bruhwiler, et al., 2021).

Carbon dioxide plays a crucial role in controlling global climate (Maslin, 2004). The comparison between the increasing rate of carbon dioxide (CO₂) in the atmosphere pre-and after the industrial era (1750) proves the effect of industrial activity on the level of GHGs in the atmosphere (Figure 1.2). The Intergovernmental Panel on Climate Change (Nakicenovic, et al., 2000) employed a range of scenarios of socio-economic, technological, and demographic developments to predict the level of greenhouse gas concentrations until the end of the 21st century. These scenarios assume that no climate-driven policy measures will be put into action to decrease the current rate of GHGs. Under these scenarios, greenhouse gas concentrations are estimated to increase to a range of [650-1350] ppm CO₂ by 2100. The IPCC projections predict that GHGs concentrations are likely to exceed 550 ppm CO₂ in the next few decades (before 2050). If it passes this level, it is not likely that global temperature increase will remain below the European Environment Agency (EEA) target which is less than 2 degrees °C above pre-industrial levels (European Environment Agency, 1993).

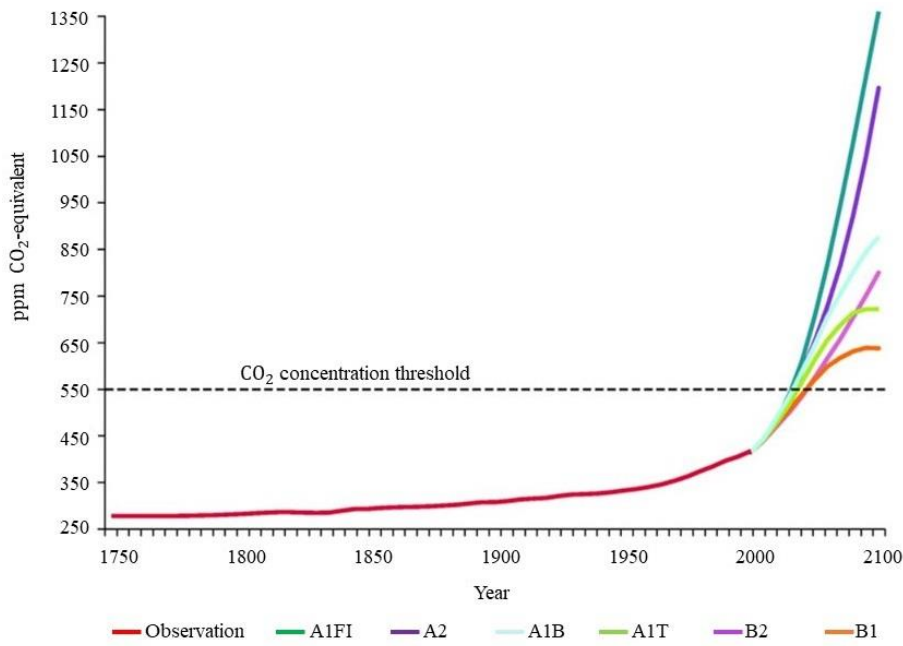


Figure 1.2 : The observed and predicted global concentration of CO₂ in atmosphere since 1750 (industrial era) (European Environment Agency, 1993).

The increasing CO₂ concentration resulted in increased global average surface and ocean temperature by about 1 °C and sea level up to 100 mm until 2020 (Earth Science Communications team at NASA's Jet Propulsion Laboratory, n.d.). The effects of rising temperature include soil degradation, loss of productivity of agricultural land and desertification, loss of biodiversity, degradation of ecosystems, reduced fresh-water resources, acidification of oceans, and the disruption and depletion of stratospheric ozone (Rossati, 2017).

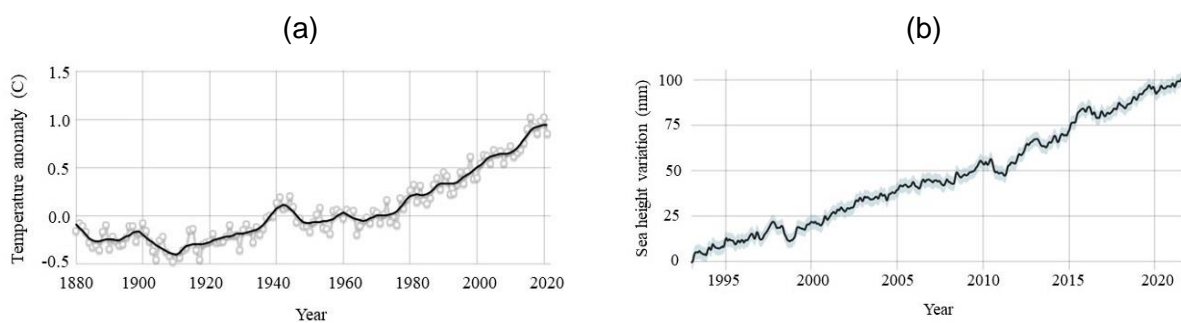


Figure 1.3 : a) The global temperature anomaly since 1880. b) The global sea height variation since 1995 (source: climate nasa.gov).

1.2 Residential and commercial building carbon footprint

As mentioned earlier, the CO₂ emission is attributed to different sectors, including residential and commercial building carbon emission. Based on a study in the United States in 2018, the

residential and commercial building CO₂ emission due to space heating/cooling accounts for roughly 38 percent and 30 percent respectively (Leung, 2018).

Geothermal energy refers to the thermal energy, reserved within the Earth's crust. According to the standard nomenclature of ASHRAE (2002), geothermal resources are divided into three groups (Maidment, 2013):

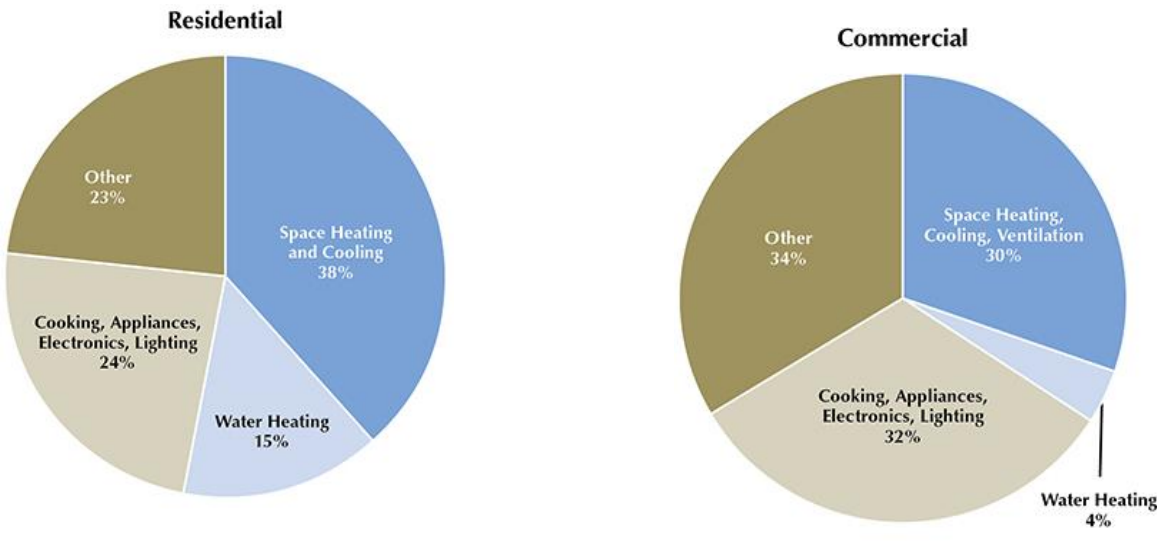
- High temperature (HT): temperature is more than 150 °C, usage: electrical power generation
- Intermediate temperature (IT): temperature is <150 °C and > 30 °C, usage: heating and hot water supply
- Low temperature (LT): temperature is less than 30 °C; usage: for cooling and heating with a geothermal heat pump system (GHPs).

The shallow geothermal energy (SGE) which is accessible in the urban area belongs to the third type (LT) of geothermal resources (Raymond, 2018). The LT geothermal resource can provide a sustainable solution reducing the residential carbon footprint and energy cost saving by furnishing a less-emission heating and air-conditioning technology compared to regular ones (Maidment, 2013; Oldenborger, et al., 2005; Figure 1.4c).

Geothermal energy popularity is increasing among worldwide renewable source of energy and geothermal heat pump system (GHPs) are the most popular applications among geothermal technologies (Ladislaus, 2001). The GHPs utilization has grown by 10 % since 1994 in developed countries. For instance, the greatest number of GPHs system has been installed in the United States since 2005, the capacity and the number of operating GHPs system in the USA were 6300 MW and 600 000, respectively (Park, et al., 2015).

(a)

(b)



(c)

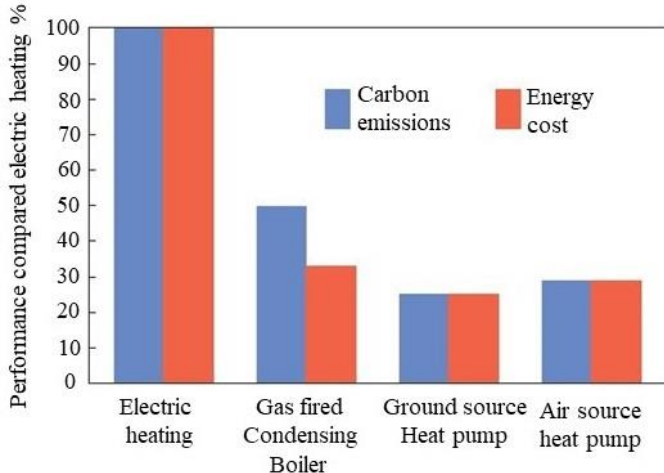


Figure 1.4 : a & b) CO₂ emission by residential and commercial building. c) A comparison between different heating technology in term of energy cost and level of Carbon emission (Leung, 2018; Maidment, 2013).

1.3 Ground source cooling/heating system

A ground source heat pump (GSHP) is an electrically powered heating/cooling system that gains or inject heat from/to the subsurface using fluid circulated through long loops of underground pipes or pumped and injected from an aquifer (Raymond, 2018).

The effect of the sun, weather, and seasonal temperature change reaches only to the depth of 10 to 20 meters. Therefore, the subsurface temperature in deeper part is constant throughout the year, ranging from 9 °C to 11 °C thus, it offers a renewable source of heat (Maidment, 2013). In this case, the earth is considered as a heat source (during the winter) or a heat sink (during the summer). The geothermal heat pump utilizes this constant source of energy for two purposes:

- To capture heat energy from earth for space heating
- To transfer heat to subsurface for space cooling

Figure 1.5 is a schematic of a typical ground-coupled heat pump system. It consists of a GSHP connected to ground heat exchanger. (Maidment, 2013; Raymond, 2018; Sarbu and Sebarchievici, 2016). During the winter, the circulating fluid warms up while it circulates in the ground loop and collects the energy of the ground. The warmed circulating fluid delivers energy through ground heat exchanger to the building. In the summertime, the process is reversed, and the heat is rejected to the ground.

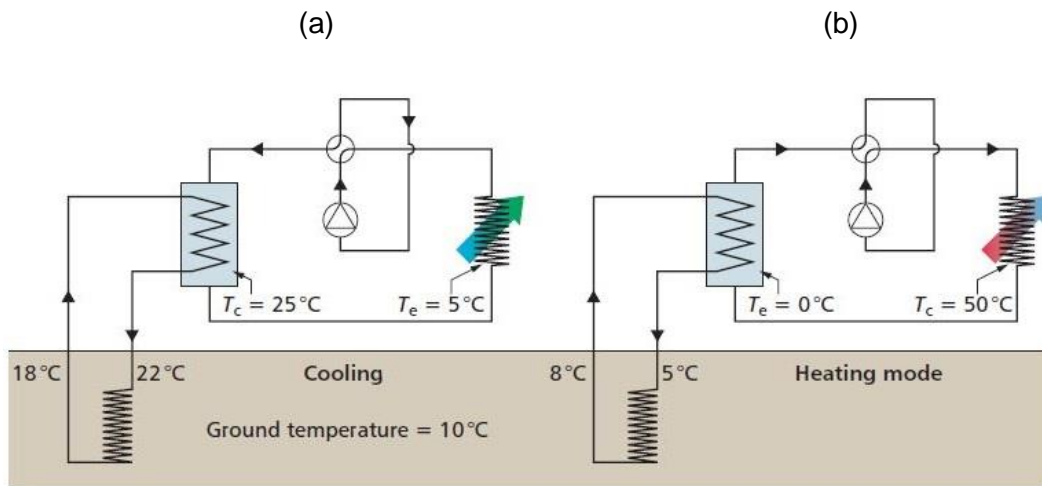


Figure 1.5 : The schematic of a typical ground-coupled heat pump system configuration in cooling (a) and heating (b) mode (Maidment, 2013).

There are three main types of geothermal heat pumps including groundwater heat pump (open loop), surface water heat pumps (open and closed loop) and ground-coupled heat pump (closed loop). The following is a short discussion of the groundwater heat pump systems (Maidment, 2013; Raymond, 2018).

1.4 Groundwater heat pump system

Groundwater heat pump (GWHP) system uses groundwater as the heat source that circulates through a heat pump or heat exchanger. The groundwater is pumped from one well (pumping well), once it has circulated through the heat pump or heat exchanger, the water reinjected into the ground through another well (injection well). The performance of GWHP systems is strongly dependent upon the hydrogeological conditions of the site. For the sustainable performance of an GWHP system, there must be an aquifer under the site where borehole can be installed.

Figure 1.6 illustrates two types of GWHP system arrangement. The simplest configuration is discharging to waste system where the pumped water from a single or a net of boreholes is disposed into surface water bodies (Figure 1.6a). The GWHP system with aquifer re-injection is another type in which the pumped water is re-injected back into the aquifer.

It should be noticed that a high pumping/injection flow rate makes a flow circulation between pumping and recharge well. A significant circulation can impose a change in the pumping water temperature with time, either increase in cooling mode or decrease in heating mode. This phenomenon is called thermal breakthrough (Maidment, 2013; Sarbu and Sebarchievici, 2016). This type of system is obviously practical only in the site where an aquifer is available.

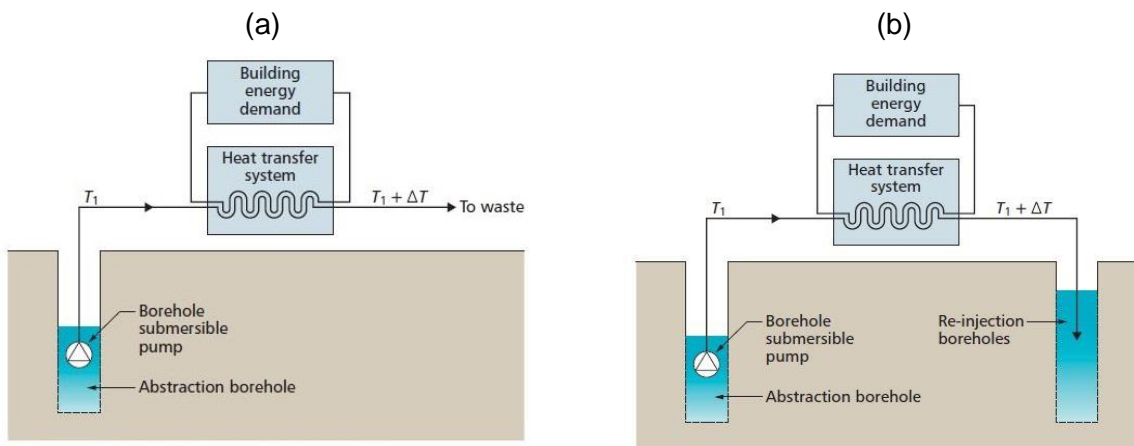


Figure 1.6 : The GWHP system configuration. a) discharging to surface water bodies. b) The Open loop systems with aquifer re-injection (Ladislaus, 2001).

Most GWHP systems operate by pumping groundwater and re-injecting it back into the aquifer. Therefore, the heat transfer in GWHP system is dominated by advection heat transfer mode. The K is one of the main parameters in advection heat transfer governing equations (Kaviany, 1995). Therefore, it is essential to estimate aquifer K heterogeneity prior to installation of open loop system to guarantee the sustainable short/long-term functionality of system (Raymond, 2018; Maidment, 2013). Any mischaracterization of subsurface parameters can lead to over/underestimation design which result in increasing installation cost or malfunction of the system in the long term (Ahmadfar and Bernier, 2014).

1.5 Subsurface characterization

There is a need to characterize the aquifer hydraulic properties in order to have a sustainable and optimal design of the geothermal system. The heat tracing experiment is a well-known tool to characterize the aquifer hydraulic parameters (Hermans, et al., 2015; Saar, 2011; Giambastiani,

et al., 2013). The experiment is performed jointly with downhole temperature monitoring and time-lapse electrical resistivity tomography (ERT) as monitoring tools (Hermans, et al., 2015; Cultrera, et al., 2018). Although both preceding monitoring tools have been used successfully in several projects, they suffer from some drawbacks. Firstly, downhole temperature monitoring is point measurement that captures the local state of the system and provides no information outside the wells. As a result, temperature measurement suffers from limited spatial coverage and resolution. To tackle the preceding shortcoming, geophysical methods have emerged (Camporese, et al., 2011). Amongst them, ERT method is popular for hydrogeological studies, as time-lapse ERT measurements are sensitive to subsurface resistivity variations and measuring points cover 2D/3D space hence it is a reliable tool to investigate shallow subsurface dynamic variations in hydrogeological state (Yan and Dongxiao, 2006; Tso, et al., 2020; Bouzaglou, et al., 2018; Camporese, et al., 2008). In the recent decades, it has been implemented successfully in the context of hydrogeology to characterize the plume geometry (Aghasi, et al., 2013) or to retrieve the spatial and temporal movement of a plume (Pidlisecky, et al., 2011; Singha and Gorelick, 2006). Inverted electrical resistivity images allow to capture the heat plume shape and propagation in the subsurface. To do so, a series of quadrupole of electrodes are deployed at the surface or/and in well. Two electrodes emit a current into the ground and the last two are measuring the potential difference.

Least-squares inversion, often referred to as inversion, is the term used in geophysics to describe the process to infer the parameters (\mathbf{m}) from measured data (\mathbf{d}) (Günther, 2004). The forward model is:

$$\mathbf{F}^*(\mathbf{m}) = \mathbf{d} \quad 1.1$$

Here \mathbf{F}^* is the physical model that links parameters (\mathbf{m}) to data (\mathbf{d}).

The inverse is iteratively computed using the least-square formalism known as normal equations:

$$\mathbf{m}_{i+1} = \mathbf{m}_i + (\mathbf{J}^T \mathbf{J})^{-1} \mathbf{J}^T (\mathbf{d} - \mathbf{F}^*(\mathbf{m}_i)) \quad 1.2$$

where \mathbf{J} is the Jacobian matrix of \mathbf{F}^* for a given \mathbf{m}_i . The Jacobian matrix represents the local derivative of \mathbf{F} with respect to the parameters.

The major problem with the least-square inversion is that it is designed to estimate the mean as its name implies. The least-squares inversion neglects the extreme values of the parameters which play a crucial role, for example, in groundwater flow and heat transfer. In addition, there

are several numerical burdens in geophysical inversion. Most of the time, there are more parameters than data, making the problem highly ill-posed (Menke, 1984). Then, the problem must be regularized to guide the solution toward a subspace of acceptable solutions. Most of the time, the subspace is the space of the smoothest solutions or the flattest (Day-Lewis, et al., 2005).

$$\mathbf{m}_{i+1} = \mathbf{m}_i + (\mathbf{J}^T \mathbf{C}_m \mathbf{J} + \mathbf{C}_d)^{-1} \mathbf{C}_m \mathbf{J}^T (\mathbf{d} - \mathbf{F}^*(\mathbf{m}_i)) \quad 1.3$$

where \mathbf{C}_m is the covariance matrix of the parameters (usually the diagonal matrix of variances) and \mathbf{C}_d is the diagonal covariance matrix of measurement error. Furthermore, the hydrogeophysical relationship between the geophysical and hydrogeological parameter is required which is calibrated on a site-specific basis so, for every case study we need to calibrate the hydrogeophysical equation (Camporese, et al., 2011).

Bulk electrical conductivity measured by time-lapse ERT measurements are not directly related to K. However, they are sensitive to changes in pore fluid properties such as temperature. The petrophysical relationship is used to quantify the relationship between bulk electrical conductivity and pore fluid temperature. Bulk electrical conductivity is usually expressed in terms of porosity, grain size and tortuosity, saturation, pore fluid electrical conductivity and surface electrical conductivity. This study focuses on a fully saturated zone in which the distribution of grain size is dominated by sand and gravel. Thus, the surface conductivity is neglected, and the bulk electrical conductivity is dominated by fluid electrical conductivity (Revil et al., 2006).

Given that, the subsurface temperature distribution is closely linked to the K heterogeneity, the petrophysical relationship can establish a link between time-lapse ERT measurement and K heterogeneity. For instance, imaging the dynamic evolution of the heat plume using time-lapse ERT measurement provide information about the K distribution.

The Bayesian assimilation method such as the Kalman filter (KF) (Kálmán, 1960) propose a promising tool for hydrogeological characterization. The idea is to integrates time-lapse measurements and numerical models to better characterize statistically the current state of the system. In addition, it can provide a better prediction of a future state of the system which is the task that monitoring tools fail to accomplish. Nevertheless, the dimensionality and nonlinearity of the system is a challenge for Kalman filter method.

Ensemble methods have been proposed to reduce the dimensionality and complexity problem where the system state is approximated using Monte-Carlo approximation (Evensen, 2009). During the last decades, the ensemble Kalman filter (EnKF) has been implemented to simulate

the dynamic hydrogeological process (Fletcher, 2017). As an effort to estimate the soil hydraulic properties in a laboratory experiment of saltwater intrusion, monitored-ERT data were assimilated into a hydrogeological model using ensemble Kalman filter (EnKF) (Bouzaglou, et al., 2018). Camporese et al., (2015) compared coupled and uncoupled hydrogeophysical inversions based on EnKF assimilation of time-lapse ERT-monitored tracer test data for a synthetic case study. Gernez et al., (2019) also developed a workflow to compute the anisotropy of K by iterative assimilation of electrical resistivity measurements (Gernez, et al., 2019).

1.6 Objectives

The objective of our project was to better characterize the heterogeneity of subsurface K to improve the design of GWHP systems used for heating and cooling buildings. A methodological and numerical workflow using EnKF was developed to reach this objective. This study uses the working hypothesis that ERT monitoring data can be used to better reproduce the heterogeneity of the aquifer K as they provide better spatial coverage of subsurface hydrogeological process such as heat injection than other monitoring tools such as downhole temperature monitoring data.

We proposed a data assimilation workflow for integrating hydrogeological, thermal and geophysical data with the aim of building coupled models of groundwater flow and heat transfer. Moreover, we assess the capability of cross-borehole ERT data as monitoring tool in a data assimilation framework during the heat tracing experiment. The proposed workflow gives access to the spatial heterogeneity of K unlike the conventional calibration method which specifies an average value of K to each hydro facies.

It is essential that the proposed workflow would be tested on real data. Therefore, the proposed workflow was tested at an experimental site in Quebec City, Canada, where a heat tracing test was achieved. The proposed workflow can easily be adapted for other case studies or even be used to characterize other subsurface hydraulic properties.

1.7 Contribution

The contribution of this thesis is to implement cross-bore ERT data assimilation instead of using conventional least-square inversion and monitoring point measurement such as downhole temperature monitoring to characterize the heterogeneity of subsurface K.

The proposed workflow allows integration of geological, hydrogeological and geophysical data to generate a set of possible subsurface K distribution scenarios in order to consider the uncertainty

associated with K distribution. In addition, it reduces the project cost by minimizing the number of boreholes required at the study site using low-cost indirect ERT measurements.

This study aimed to evaluate the capability of the proposed assimilation workflow to address uncertainties in real field data that do not exist in controlled laboratory studies. I wrote one conference paper (Shariatnik, et al., 2021).

1.8 Project's context

Conventional building air conditioning technologies release large amounts of heat into the air and contribute to the creation of urban heat islands. Shallow aquifers in permeable geological formations provide natural infrastructure that can contribute to energy-efficient cooling. The subsurface of major Canadian cities generally maintains a stable temperature below 11 °C (Majorowicz, et al., 2009), although the local temperature may increase by 5 °C due to the heat islands (Ferguson and Woodbury, 2004). Hence groundwater can be used to cool down buildings using geothermal systems, which offers an energy savings of 40-80% compared to conventional systems. The technologies needed to implement this promising alternative are available, but its potential for use in large urban buildings remains to be determined.

To do so, the Aquifroid project has been proposed to carry out a risk and opportunity study to determine the potential of different aquifers in Canada for air conditioning in the context of climate change adaptation. The aims of the project are as follows:

- to identify opportunities for the use of aquifers for air conditioning in large cities,
- to better understand the risks represented by the chemical and bacteriological composition of groundwater, and
- to predict the impact that the accelerated deployment of this technology could have on a city-wide scale, taking the example of Quebec City, one of the ten largest cities in the country with a population of over 0.5 million.

The ultimate objective is to identify best practices in the use of aquifers for air conditioning and lessen our carbon footprint, while ensuring the protection of groundwater resources. In addition, it will help protect the health of Canadians and prevent discomfort, inconvenience or disease that can result from an extreme heat wave caused by global warming. Throughout this project, field tests were carried out in Quebec City, which will include a heat tracing test, hydraulic well tests and numerical modeling of thermal systems to assess the overall impact on urban heat islands

and the temperature of aquifers. The site was also assessed for installing an open loop geothermal system.

This study contributes to Aquifroid project. In this study a multidisciplinary approach is proposed in order to study a problem with an emphasis on hydrogeology. A heat tracing test was considered to develop methodological and numerical tools for characterizing the spatial distribution of the hydraulic properties of the subsoil in order to optimize geothermal systems. The effectiveness of geothermal systems depends not only on the performance of the heat exchangers, but also on the nature and heterogeneity of the rock and the fluids forming the aquifer system. The optimal design of a geothermal system therefore requires the hydraulic characterization of the aquifers in which they are installed.

1.9 Experimental site

1.9.1 Hydrogeological background

The nature and spatial distribution of geological deposits play an important role over groundwater runoff. In the territory of the Quebec Metropolitan Community (QMC), the geological history of the region led to the establishment of three geological provinces overtapped by a complex of soft deposits of glacial and recent origin. The spatial distribution of these geological units is related to the spatial distribution of groundwater (Talbot Poulin, et al., 2013).

The Figure 1.7 illustrates the hydrostratigraphic cross-section of Proto-Saint-Laurent's delta situated at the base of Quebec City. The map was provided by Laval University based on the PACES-CMQ hydrogeological database (Talbot Poulin, et al., 2013). Regarding to the hydrostratigraphic cross-section, the rock is overtapped by the sediments of the upper Wisconsinan to pre-Wisconsinan (Lamarche 2011) consisting mainly of sandy or gravelly silt (Hydrofacies #2). Deep-water marine sediments composed of silt (Hydrofacies #1) cover this unit. Deltaic sediments of the Proto-St.Lawrence composed of sand (Hydrofacies #4) and a thin gravel layer at the base (Hydrofacies #5) cover the previous unit. On the surface, alluvial deposits of estuarine and fluvial origin form a layer of sandy silt (Hydrofacies #2; Talbot Poulin, et al., 2013).

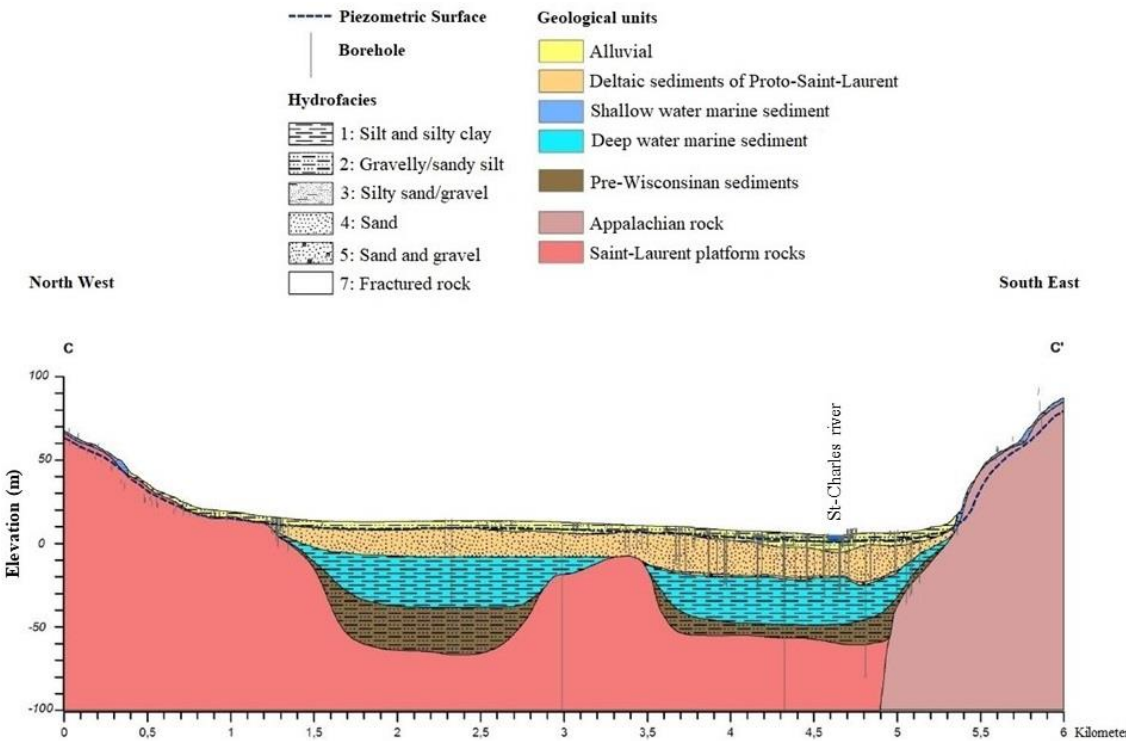


Figure 1.7 : Hydro-stratigraphic cross-section C-C'. The cross-section illustrates the Proto-Saint-Laurent Delta that include the Hydro-stratigraphic exist at the base of Quebec City (Talbot Poulin, et al., 2013).

Two distinct aquifers separated by deep-sea silts are present in this area. The former is a deep aquifer in the fractured rock and the latter is a shallow deltaic sand aquifer. The Deltaic Sand Aquifer is a regionally significant soft deposit aquifer. Figure 1.8 shows the thickness of the deltaic aquifer in the Quebec City area which is up to 80 m (Lamarche, 2011).

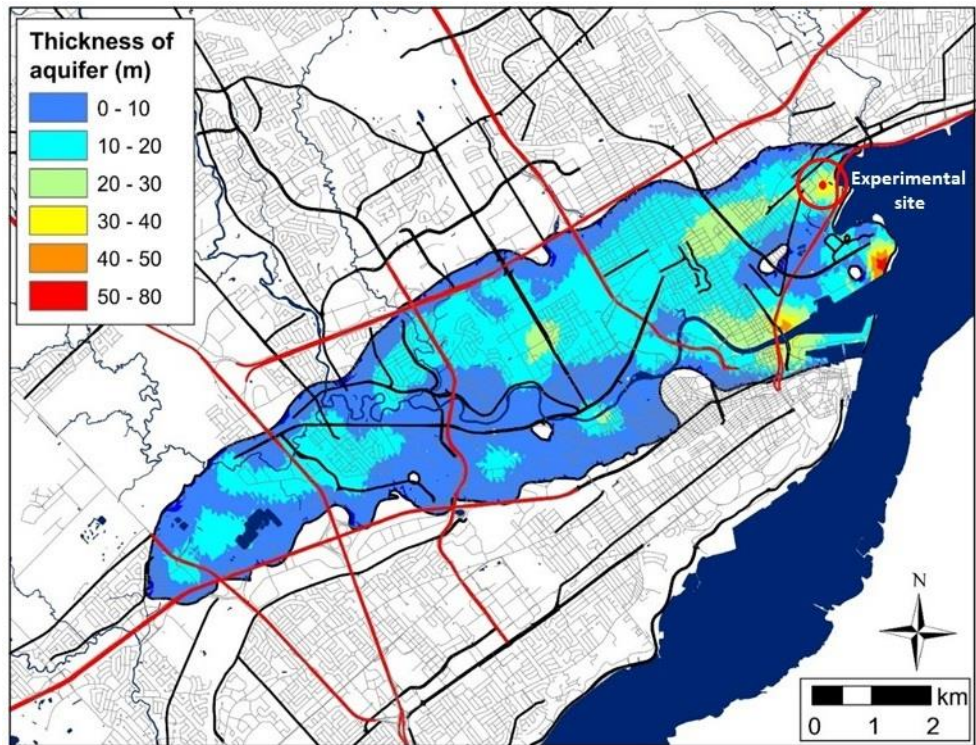


Figure 1.8 : The thickness of the deltaic aquifer in Quebec City area (Lamarche, 2011). The red circle indicates the experimental site location.

Conventional building air conditioning technologies release large amounts of heat into the air. The accumulation of thermal energy in our cities contributes to the formation of the urban heat island (Arnfield, 2003). Extreme heat can cause discomfort, especially among vulnerable individuals, or intensify the symptoms of certain diseases. Urban aquifers are a natural infrastructure that can help reduce the effects of heat islands by replacing the low CO₂ and energy-saving geothermal cooling system with conventional building cooling technologies. Figure 1.9 shows the deltaic aquifer extension with regard to the vulnerability of Quebec population to heat wave (Barette et al., 2018).

The deltaic sandy aquifer covers a large part of Lower Quebec City affected by urban heat islands. The aquifer is located directly under important urban infrastructures. The thickness, location and depth of this deltaic sandy aquifer make it an interesting target for developing ground source cooling system in the Quebec City area.

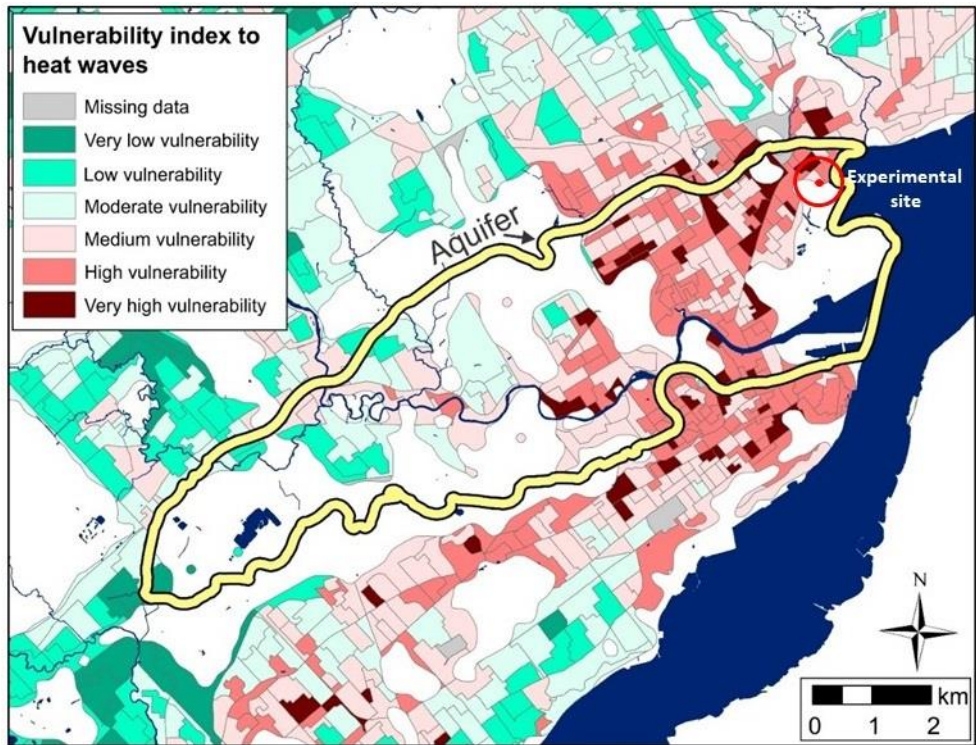


Figure 1.9 : The vulnerability of population to heat wave in Quebec City area. The yellow line marks the deltaic sandy aquifer extension around Quebec City (Barette et al., 2018). The red circle indicates the experimental site location.

In this study, a heat injection experiment was designed to characterize the heterogeneity of the hydraulic properties of the deltaic aquifer in a specific experimental site in Quebec City in order to provide information for installing GWHP systems. We will discuss the experiment field setup detail in the following.

1.9.2 Field setup

The heat-tracing experiment was conducted at a site in Quebec City, Canada, near the Baie de Beauport, northern shore of the St-Lawrence River (Figure 1.10a). Characterization of the subsurface site was initiated through a cone penetration test (CPT) to better understand the lithologies present at the site. Figure 1.11 shows the configuration of monitoring wells (a) and interpreted CPT log with lithostratigraphic units for Well #2 (b). Based on the CPT results, the site's lithostratigraphy is interpreted to be a sequence of five distinct units. Overlying the bedrock, the first basal unit is composed of compact clay. The second unit is composed of sand and gravel, fining upward sequence, at a depth ranging from 24 m to 30 m below the ground surface. This unit is interpreted to be the main aquifer at the site. The aquifer is overlaid by a thin clay/silt unit

and the clay/silt unit is overlaid by two units of more compacted and uncompacted very fine sand, respectively.

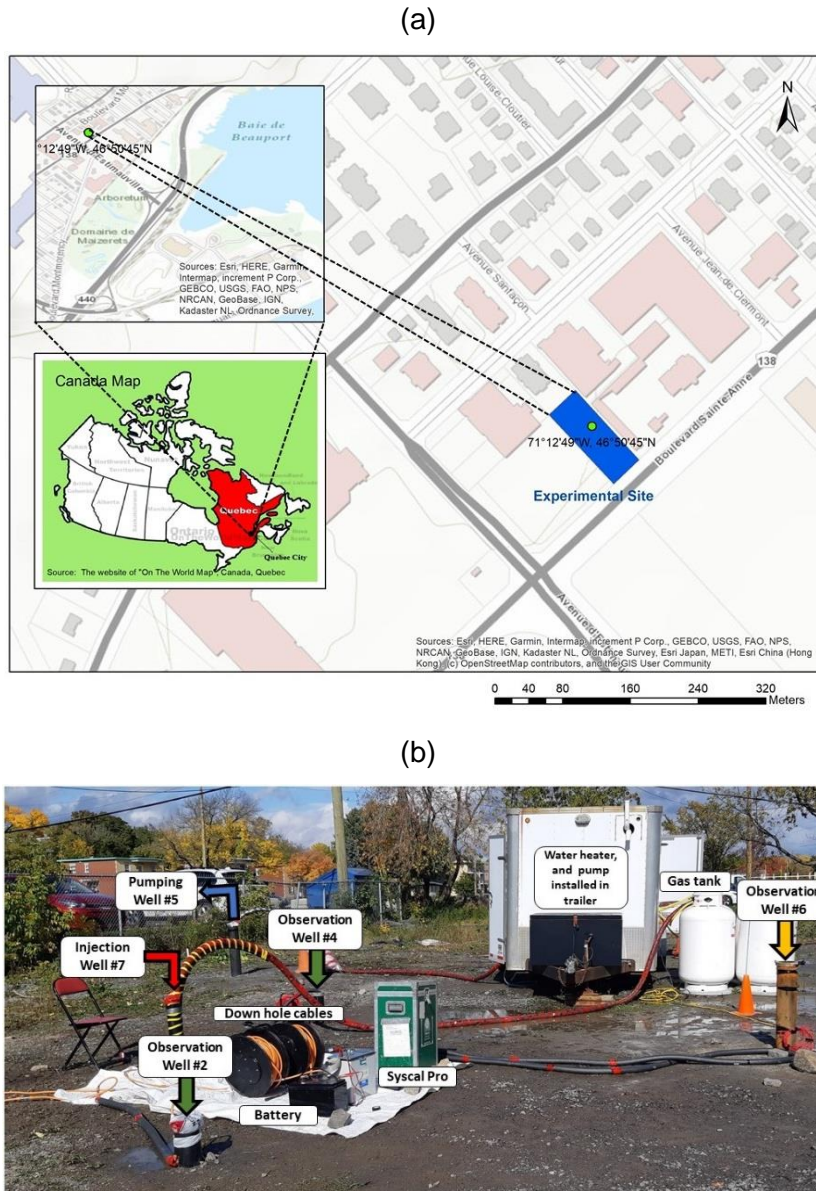


Figure 1.10 : a) The experimental site is near the Baie de Beauport, northern shore of the St-Lawrence River, Quebec City, Canada. **b)** Heat-tracing equipment setup at the site, and location of pumping, injection, and observation wells. The position of pumping, injection and three ERT monitoring wells, downhole cable run into the bottom of well #2 and #4, Water heater was installed in trailer.

At the experimental site, five wells were installed to perform the heat-tracing experiment (Figure 1.10b & 1.11a; Table 1.1). A pumping well (Well #5) was drilled at the northern part of the site, to supply the water that was heated and reinjected in Well #7. The Well #5 is hydraulically upgradient from the injection well (Well #7) and both are five meters apart. Three monitoring wells were used to perform cross-borehole ERT monitoring. Well #2 and Well #6 are located in the

southern part of the site and Well #4 in the middle of the site. The Well #2 and #4 were equipped with six downhole electrodes with one meter spacing across the screened interval; An electrode was mounted at the bottom of Well #6 as an infinite electrode to perform pole-dipole array (Figure 1.10b & 1.11a). All wells were screened in the aquifer at the base of the interval between 24 m and 30 m depth (Figure 1.11b), except Well #4 that is totally screened (Table 1.1). The groundwater flow direction is west to east, which is perpendicular to the cross-section of Well #2 and Well #4.

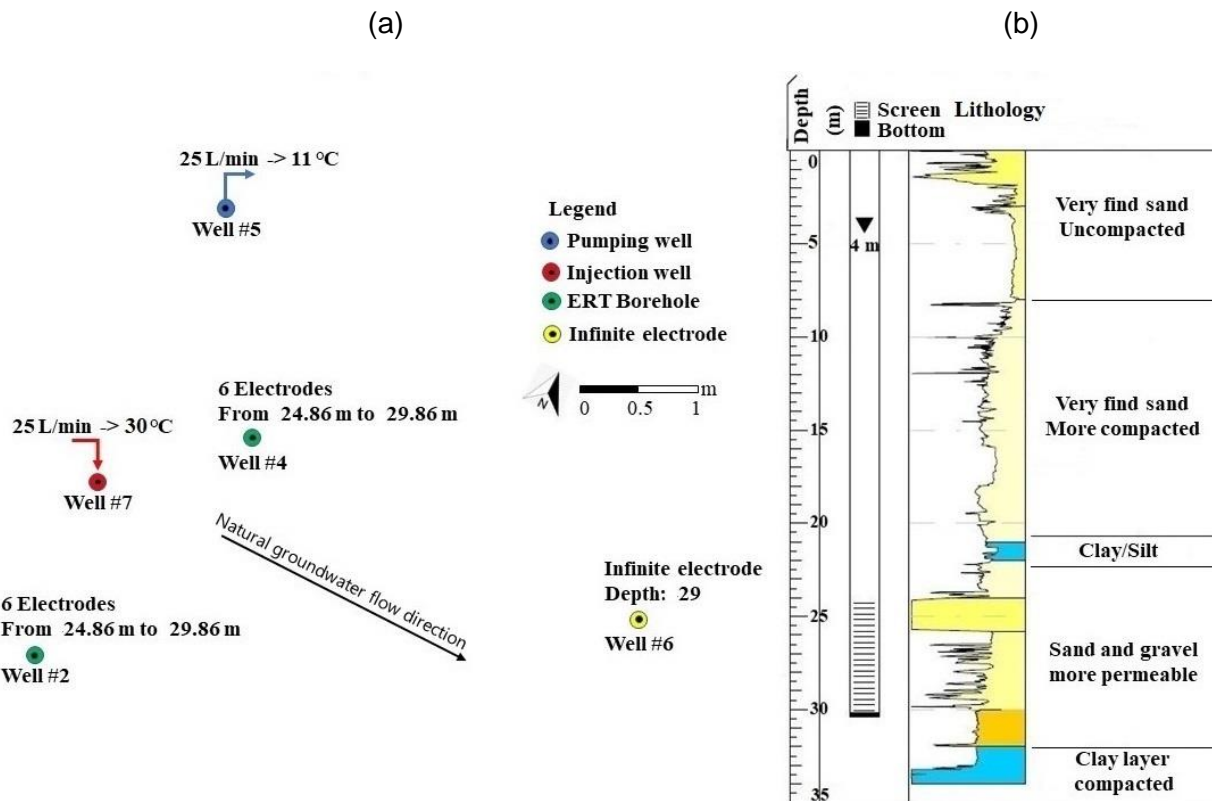


Figure 1.11 : a) The configuration of the pumping, injection and ERT monitoring wells b) interpreted lithological units using CPT logs in Well #2 and scheme of the installed well casing.

Table 1.1 : The wells characterization.

Well name	Final depth (m)	Screened interval depth (m)
Well #2	29.18	[23.18-29.18]
Well #4	30.95	[5.45-30.95]
Well #5	31.82	[25.82-31.82]
Well #6	31.98	[25.98-31.98]
Well #7	31.86	[25.86-31.86]

The groundwater temperature profile was made in Well #2 (Figure 1.12) in order to measure the baseline groundwater temperature prior to the heat-tracing experiment. The baseline groundwater temperature was 10.3 °C according to groundwater temperature profile

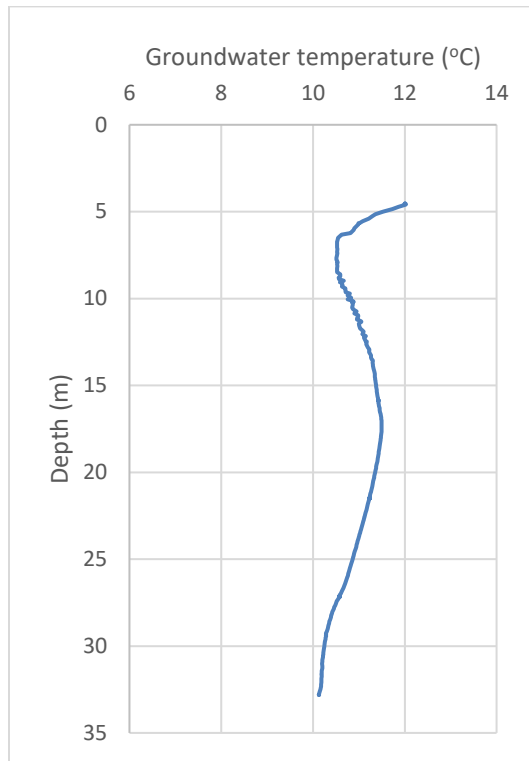


Figure 1.12 : Groundwater temperature profile measured in Well #2.

Thermal response tests (TRT) were performed before the heat tracing experiment in Well #4 and Well #6 to evaluate the thermal conductivity of different Lithostratigraphic units (Lee, et al., 2021). An electrical heating cable with the power of 35.6 ($\text{W} \cdot \text{m}^{-1}$) was employed to inject heat into both boreholes. The duration of injection and recovery phase was 103.5 hours. The temperature sensors were mounted in both wells to monitor the temperature behavior of wells.

Table 1.2 : The results of two TRT performed in Well #4 and Well #6. The interpreted thermal conductivity in Well #6 appeared more reliable.

Well	Depth (m)	Temperature sensor Spacing (m)	Number of temperature sensor	Thermal conductivity (Aquifer) ($\text{W} \cdot \text{m}^{-1} \cdot \text{K}^{-1}$)	Thermal conductivity (Top of Aquifer) ($\text{W} \cdot \text{m}^{-1} \cdot \text{K}^{-1}$)
Well #4	[5.95-30.95]	1	26	[55.89-427.23]	[1.49-14.7]
Well #6	[4.48-31.48]	1	25	[1.5-3.29]	[1.48-1.5]

The TRT assumes that the conduction heat transfer is dominated, but it is not the case in aquifer interval, due to groundwater flow the convection heat transfer dominates in aquifer interval so the estimated thermal conductivity in this interval is increased. To tackle this issue, we used the thermal conductivity from top of aquifer where the conduction heat transfer assumption is satisfied. Figure 1.13a-b depicts the monitoring temperature data at the depth of 28 m in Well #6 during injection and recovery respectively and is given as an example.

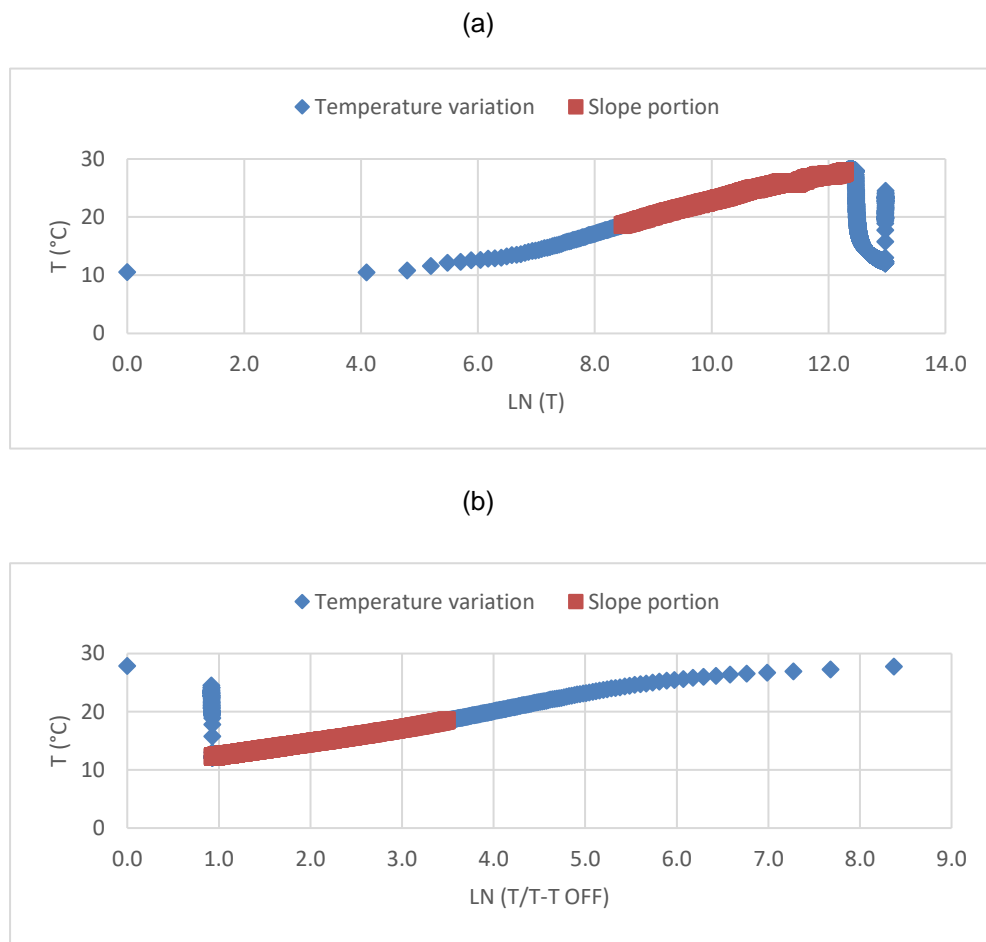


Figure 1.13 : The TRT analysis plots. a) Injection period b) recovery period.

The thermal conductivity values were inferred (Table 1.2) based on the infinite linear source (ILS) equation using the slop method (Focaccia, et al., 2013). ILS is a well-known method for analyzing TRT data that enables us to calculate underground thermal conductivity (Raymond, 2019) (Focaccia, et al., 2013). The slop portion (red line) in Figure 1.13 shows late time injection (Figure 1.13a) and the recovery temperature monitoring data (Figure 1.13b) data which are used to calculate the slope and then thermal conductivity which is proportional to the slope value.

Table 1.3 : The Thermal conductivity calculated at 28 m in well #6 based on the TRT analysis for both heat injection and recovery.

Injection period	Recovery period
1.29 ($\text{W} \cdot \text{m}^{-1} \cdot \text{K}^{-1}$)	1.22 ($\text{W} \cdot \text{m}^{-1} \cdot \text{K}^{-1}$)

It is straight forward to see that temperature data during the recovery period is more uniform hence, the interpreted thermal conductivity using recovery period data is judged more reliable. Six Air- pressurized slug tests were conducted in Well #2 and Well #3 (Table 1.3). The method of Springer-Gelhar (1991) was employed to estimate K. The various slug test analysis estimated the aquifer K ranging from 1.12×10^{-4} ($\text{m} \cdot \text{s}^{-1}$) to 3.03×10^{-4} ($\text{m} \cdot \text{s}^{-1}$).

Table 1.4 : The range of K estimated by slug test. The slug test was performed in Well #2.

Well	Number of tests	Analysis method	Range of K - 10^{-4} ($\text{m} \cdot \text{s}^{-1}$)
Well #2	6	(Springer-Gelhar, 1991)	[1.12-3.03]
Well #3	4	(Springer-Gelhar, 1991)	[2.29-2.89]

Figure 1.14 is one of the slug test analysis plots. In this case, the estimated K was equal to 1.12×10^{-4} ($\text{m} \cdot \text{s}^{-1}$).

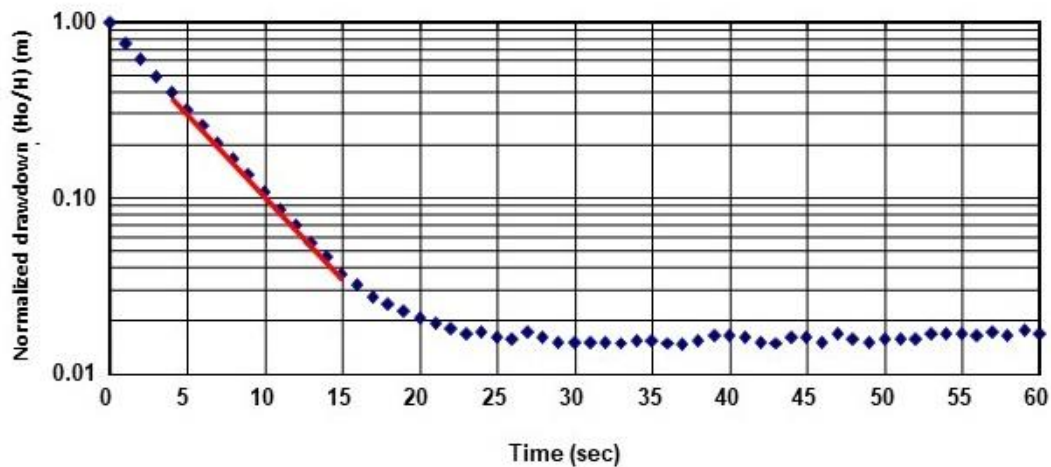


Figure 1.14 : The plot shows the one of the Air- pressurized slug test analyses performed in the well#2.

The pumping and injection heat-tracing experiment started on September 1st, 2020 and lasted for a period of 75 hours. The pumping and injection rates varied over time from 25 ($\text{l} \cdot \text{min}^{-1}$) to 3 ($\text{l} \cdot \text{min}^{-1}$) due to injection Well #7 clogging from biofouling developed from downhole biological activities. The pumped water went directly through a water heater and was reinjected into Well #7 at a temperature of approximately 30 $^{\circ}\text{C}$. During the experiment, the time-lapse ERT monitoring

survey was conducted 11 times at irregular time intervals, ranging from 6 to 12 hours between surveys.

1.9.3 Theoretical background

The numerical model of heat injection experiment was developed using the finite element program FEFLOW 7.3. The theoretical aspect and the governing equation of transient groundwater flow and heat transfer model in an unconfined aquifer in FEFLOW 7.3 are outlined in this subsection.

The transient groundwater flow in unconfined aquifer is governed by following equation (Diersch, 2014):

$$(\mathbf{B}S_0 + \boldsymbol{\varepsilon}_e) \frac{\partial \mathbf{h}}{\partial t} + \nabla \cdot \bar{\mathbf{q}} = \mathbf{Q} \quad 1.4$$

where, \mathbf{B} is the aquifer thickness (m), S_0 is the specific storage coefficient (m^{-1}), $\boldsymbol{\varepsilon}_e$ represents specific yield, \mathbf{h} refers to the head (m), t is time (s), $\bar{\mathbf{q}}$ is the depth-integrated Darcy velocity ($m \cdot s^{-1}$) which is calculated using Equation 1.5 and 1.6 in which \mathbf{f}^B is the bottom bounding surface of aquifer (m), K is the tensor of K .

$$\bar{\mathbf{q}} = -\mathbf{B}K \cdot \nabla \mathbf{h} \quad 1.5$$

$$\mathbf{B} = \mathbf{h} - \mathbf{f}^B \quad 1.6$$

The term \mathbf{Q} is split by Equation 1.7 where \mathbf{Q}_h and \mathbf{Q}_{hw} are flow supply term and flow well-type specific point condition (SPC) ($m^3 \cdot s^{-1}$).

$$\mathbf{Q} = \mathbf{Q}_h + \mathbf{Q}_{hw} \quad 1.7$$

Heat transfer in a porous media with natural groundwater flow includes conduction and forced convection (Kaviany, 1995). A simplifying assumption of the temperature equilibrium between solid matrix and pore fluid ($T_s = T_f = T$) is considered, where subscripts s and f stand for solid and fluid phases, to avoid the complexity of energy transport computation between them (Domenico & Schwartz, 1998).

The equation 1.8 integrates the conductive and forced convection heat transfer to calculate the amount of energy gain/loss at each elemental volume (Diersch, 2014).

$$\begin{aligned}
& (\Theta s \rho_f c_f + (1 - \Theta) \rho_s c_s) \frac{\partial T}{\partial t} + \rho c q \cdot \nabla T - \nabla \cdot (\lambda_e \cdot \nabla T) \\
& = Q_T + Q_{Tw} - \rho' c' (T - T_0) Q
\end{aligned} \tag{1.8}$$

where, Θ is the porosity, s is saturation, $\rho_f c_f$ and $\rho_s c_s$ are the fluid and solid volumetric heat capacity ($J \cdot K^{-1} m^{-3}$) respectively, q is the Darcy velocity ($m \cdot s^{-1}$), ∇T is the gradient of temperature $^{\circ}C$, λ_e is the effective thermal conductivity ($W \cdot m^{-1} K^{-1}$), Q_T is the heat supply term ($W \cdot m^{-2}$), Q_{Tw} is the well-type (SPC) term ($W \cdot m^{-2}$). The notation $\rho' c'$ refers to the effective volumetric heat capacity (Equation 1.12).

$$\lambda_e = \lambda_f + \lambda_s \tag{1.9}$$

$$\rho' c' = \Theta \rho_f c_f + (1 - \Theta) \rho_s c_s \tag{1.10}$$

On the boundary closing the modeling domain or for node(s) inside it, the hydraulic/temperature is known beforehand. In this case the Dirichlet-type (1st kind) boundary conditions (Equation 1.11) are applied. For node(s) where the hydraulic head/temperature values are known, fixed values are forced instead of calculating as a simulation result. It can result in inflow into the model or outflow when neighboring nodes having a lower/higher head/temperature respectively. A fixed/time-varies hydraulic head/temperature is assigned to a/series of node(s) of mesh boundary using following equation:

$$h(\mathbf{x}, t) = h_D(t) \tag{1.11}$$

where, h_D is the prescribed hydraulic head/temperature on/inside the boundary of the model domain.

The prescription of well-type BC in 3D heterogeneous aquifers under confined or unconfined condition requires a general formulation to model the effects of well bore storage and vertical gradient of variables (hydraulic head, temperature) along the well bore and well screens in a more realistic way. A multilayer well boundary condition is used to simulate pumping or injection of water via a vertical/ inclined well screen that possibly extends over several model layers or element groups. The portion of the total pumping or injection rate specified to each layer is a simulation result and depends on the surrounding material properties and the surrounding distribution of hydraulic head in the different layers. Consequently, for a multilayer well with low or no pumping/injection rate, a groundwater flow between layers with different hydraulic-head

level may occur. Thus, groundwater enters into a layer and produce from another layer in the same borehole (Diersch, 2014).

The 1D discrete feature equation describing transient liquid flow along the axis of the borehole is given using the following equation:

$$\pi R^2 \left(\frac{1}{L_w} + \rho_0 g \gamma \right) \frac{\partial h}{\partial t} - \pi R^2 K_w \frac{\partial}{\partial s} \left[f_\mu \left(\frac{\partial h}{\partial z} + \chi e \right) \right] = -Q_w \delta(z - z_w) \quad 1.12$$

where the borehole K is equal to:

$$K_w = \frac{R^2 \rho_0 g}{8 \mu_0} \quad 1.13$$

Here, Q_w is the total pumping rate ($m^3 \cdot s^{-1}$), z refers to the vertical coordinate, z_w is the location of the point that is assigned to discharge/recharge the well bore (m), h represents the hydraulic head in the well (m), L_w is total length liquid-filled well bore (m), R is the radius of well casing and screen(s) (m). $\delta()$ represents the Dirac delta function in 1D, γ is the compressibility of liquid (psi^{-1}), f_μ is the viscosity relation function of liquid, χ is the buoyancy coefficient, e is the gravitational unit vector, g is the gravitational acceleration ($m \cdot s^{-2}$), ρ_0 is the reference density of liquid ($\text{kg} \cdot \text{m}^{-3}$) and μ_0 is the reference viscosity of liquid (Pa.s).

2 Methodology

In this chapter, an overview of the Time-lapse electrical resistivity tomography, time-lapse electrical inversion and finally data assimilation method used in the proposed data assimilation workflow is outlined to support the results chapter.

2.1 Workflow

In this study, a workflow including the implementation of EnKF to assimilate time-lapse cross-borehole ERT data in a heat tracing experiment is tested, in order to investigate the capability of the proposed workflow to characterize the heterogeneity of K of the ground. The proposed workflow is composed of six major steps that are repeated for each monitoring time step:

1. An ensemble of K parameter sets derived from prior information is provided at the beginning of the process. The depth of each layer is determined using lithological unit's log (Figure 1.11B). The K values are populated through each lithological unit using sequential gaussian simulation (SGS). These equiprobable scenarios represent our best knowledge of the heterogeneity of subsurface K.
2. The ensemble is propagated through transition function (forward transient simulation of groundwater flow and heat transport) to model the subsurface temperature.
3. The computed temperatures are converted to a 3D electrical resistivity distribution using petrophysical relationship.
4. An electrical forward model using 3D electrical resistivity distribution is computed in the last step to predict the subsurface apparent electrical resistivity at the location of electrodes.
5. Finally, the cross-borehole ERT field measurements (observations) and the predicted apparent electrical resistivity (output of electrical forward modeling) are assimilated to update the K within the ensemble.

In the following subsections, each step of the workflow will be discussed in detail.

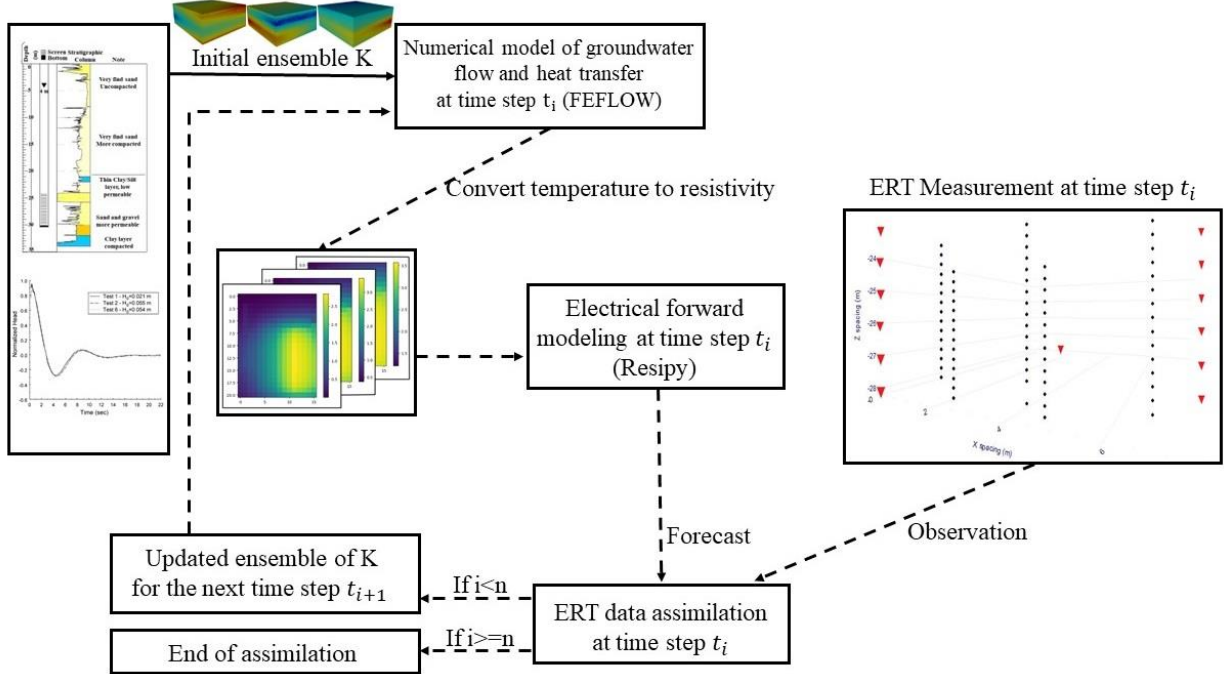


Figure 2.1 : The workflow shows the implementation of time-lapse cross-borehole ERT data assimilation to calibrate subsurface 3D distribution of K. The letter n refers to the number of monitoring time steps.

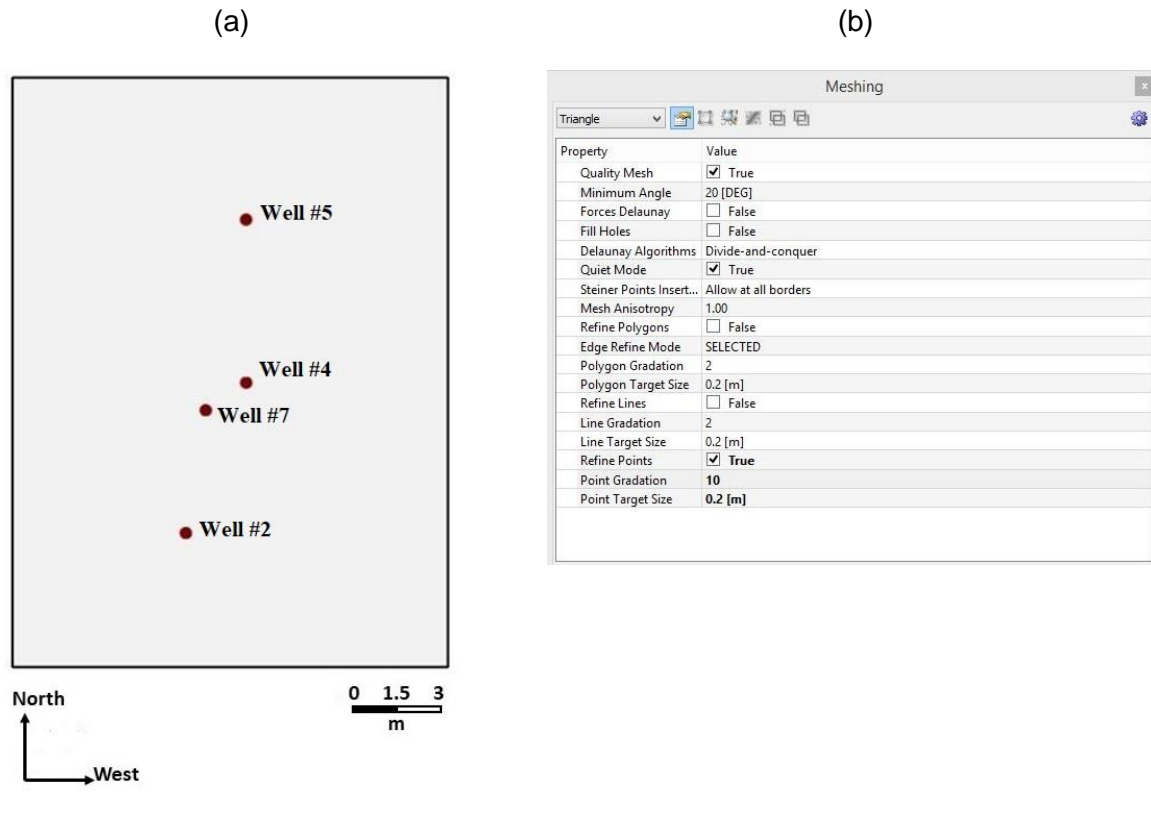
2.2 Numerical model of groundwater flow and heat transfer

The numerical model is solving the differential equations using a finite element mesh and FEFLOW simulator (FEFLOW 7.3). The API functions of FEFLOW 7.3 (DHI, n.d.) were used to reassign updated K at each monitoring time-step and retrieve simulated groundwater temperatures under similar conditions as imposed through the heat-tracing experiment. The conduction-forced convection heat transfer mode was used to simulate heat transfer with the model. The density of water was considered as a function of temperature.

2.2.1 Define a mesh

The model domains' dimensions are 14 m by 19 m by 14 m along North, West, and depth axis respectively (Figure 2.2a). A 3D triangular mesh containing 29 slices and 28 layers with the uniform thickness of 0.5 m was generated. The top of 3D mesh is set to be at the depth of 19 meter, so the model is always fully saturated. Each slice and layer of the mesh is composed of 3,737 nodes and 7,335 elements, respectively (Figure 2.2c). Moreover, a mesh independence test was done to study the mesh resolution at which the simulation results are independent of the mesh resolution. This was accomplished by running a few simulations with a different mesh resolution and verifying if the results changed. The allowed minimum and maximum size of the

element was 0.5 m and 0.2 m respectively. The 3D mesh and the mesh consisted of 205380 elements and 108373 nodes in total (Figure 2.2d).



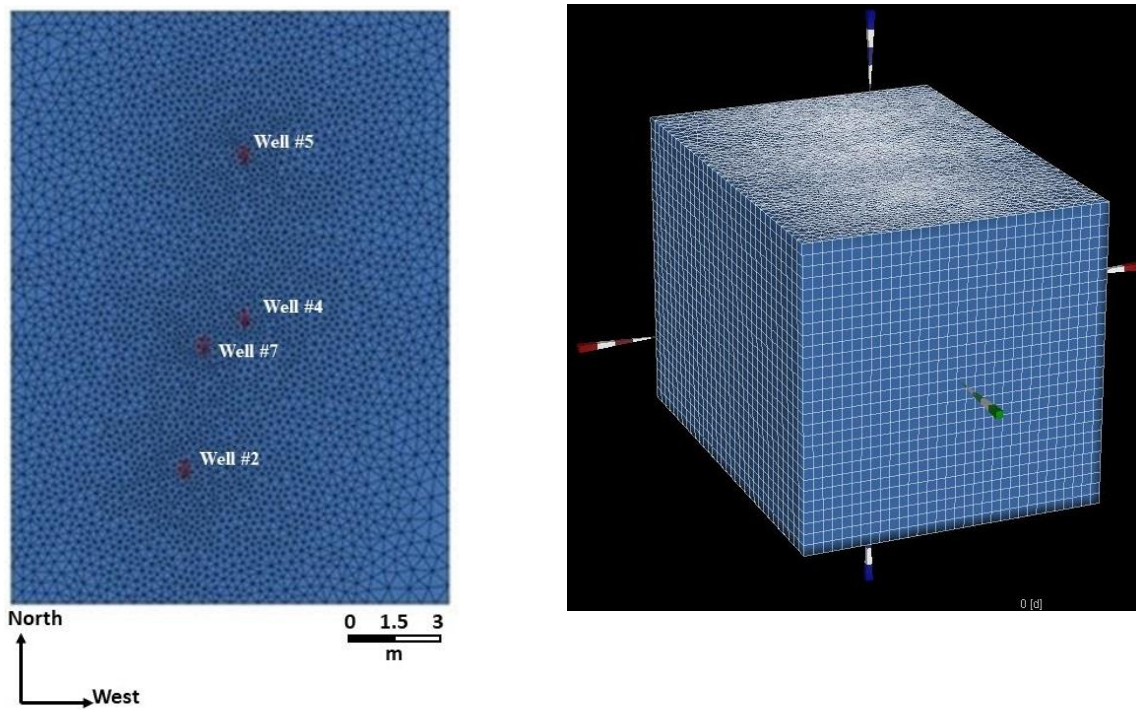


Figure 2.2 : a) Super mesh illustrating the well location and extension of model domain. **b)** Define 2D mesh parameters. **c)** 2D triangular mesh **d)** 3D mesh with vertical resolution of 0.5 m.

It is required to accurately define material properties, initial and boundary condition to develop the numerical model of the heat tracing experiment.

2.2.2 Material properties

The material properties have been specified in the model mesh according to previous measurements available in the field, such as TRT, slug test, lithological log. Bibliographical references (Hwang, et al., 2017; Talbot Poulin, et al., 2013) were also taken into account.

The thermal conductivity was attributed to the mesh according to the TRT results (see section 1.9.2). The mean of two thermal conductivity ranges in Well #6 (Table 1.2) were calculated and specify to the aquifer and top of aquifer's Lithostratigraphic units. The Lithological log (Figure 1.11b) and the bibliographic data (Hwang, et al., 2017) enabled the selection of the range of K values for each Lithostratigraphic units (Table 2.1).

Table 2.1 : Summary of K of Lithostratigraphic units (Hwang, et al., 2017; Talbot Poulin, et al., 2013)

Layer	Depth (m)	K ($\log_{10} K (\text{m.s}^{-1})$)
Very fine sand	[19-21]	Mean: -6 Standard Deviation = - 0.33
Clay/silt	[21-22]	Mean: -7 Standard Deviation = - 0.33
Sandy-gravel Aquifer	[22-32]	Mean: -4 Standard Deviation = - 0.5

Compacted clay	[32-33]	Mean: -9	Standard Deviation = - 0.33
----------------	---------	----------	-----------------------------

The geometric average of other material properties were taken from bibliographic references (Gibb, et al., 1984; Woessner & Poeter, 2020; Talbot Poulin, et al., 2013; Ižvolta & Dobeša, 2014).

Table 2.2 : The table of material properties (Talbot Poulin, et al., 2013)

Layer	porosity	Longitudinal dispersivity (m)	Transverse dispersivity (m)	Specific heat capacity of solid (J. Kg ⁻¹ K ⁻¹)	Density (gr. cm ⁻³)	Storage (m ³ . m ⁻³)
Very fine sand	0.45	5	0.5	945	1.8	3-10 ⁻⁰³
Clay/silt	0.45	5	0.5	945	1.4	3-10 ⁻⁰³
Sandy-gravel Aquifer	0.44	5	0.5	945	1.65	7-10 ⁻⁰⁴
Compacted clay	0.45	5	0.5	945	2	1-10 ⁻⁰⁴

2.2.3 Initial condition

Temperature sensors and level loggers were installed in all the available wells before the start of the experiment to measure the aquifer baseline temperature and hydraulic gradient respectively. According to the temperature sensors and level logger data, the uniform baseline temperature is 10.3 °C and the hydraulic gradient is 0.003 m/m respectively. A steady-state simulation with hydraulic gradient of 0.003 m/m was performed to evaluate the hydraulic head distribution used as initial values for running the transient model of heat injection experiment.

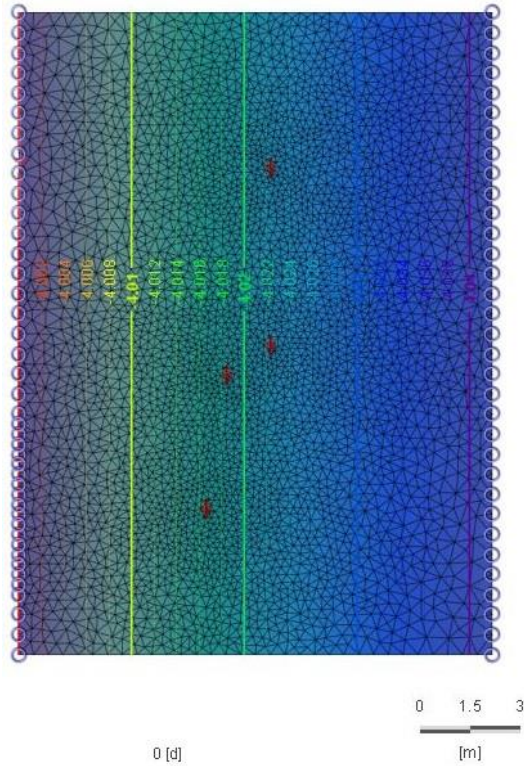


Figure 2.3 : The initial hydraulic head is the result of a steady state simulation.

2.2.4 Boundary condition

The groundwater flow and heat transfer boundary conditions need to be defined to reproduce heat-tracing experiment accurately. Pumping and injection wells have been considered as multilayer wells (Section 1.9.3). Table 2.3 and 2.4 present the time series of injection and pumping rates imposed to the model. The pumping and injecting values are respectively positive and negative.

Table 2.3 : Pumping and injection rate time-series.

Start (min)	End (min)	Flow rate ($\text{l} \cdot \text{min}^{-1}$)
0	1395	± 25
1395	1793	± 15.7
1793	2480	± 10.6
2480	3016	± 5.7
3016	10080	0

Type I (constant temperature) boundary condition (section 1.9.3) has been imposed to the injection well (Figure 1.11a).

Table 2.4 : The time-series of injected water temperature.

Start (min)	End (min)	Temperature (°C)
0	3016	30

Type I (constant heads) hydraulic head boundary condition were imposed from the top to the bottom of the east and west edge of the model (Figure 2.3) to reproduce a horizontal hydraulic gradient of (0.003 m/m) representative of measured hydraulic conditions prior to the test (Diersch, 2014).

Type I (constant temperature) boundary conditions was imposed from the top to the bottom of the east edge of the model to maintain water inflow temperature equal to the baseline groundwater temperature. Other boundaries were far enough from the pumping and injection well to be considered adiabatic.

2.3 Time-lapse electrical resistivity tomography

Time-lapse ERT is an approach to assess the main subsurface thermal and hydrological parameters. The variation of underground electrical conductivity over different monitoring time steps is captured to characterize the thermal/hydraulic characteristics of the subsurface. Although the time-lapse ERT is not able to directly measure the subsurface hydraulic/thermal properties, the change in subsurface electrical conductivity could reflect the distribution of hydraulic and thermal properties.

2.3.1 Petrophysical relationship and forward modeling

Archie (1942) defined the ratio of bulk electrical conductivity and pore fluid electrical conductivity as formation factor (Archie, 2013):

$$F = \frac{\sigma_b}{\sigma_f} \quad 2.1$$

The bulk electrical conductivity σ_b ($S \cdot m^{-1}$) is a function of pore fluid electrical conductivity σ_f , tortuosity and effective porosity. It is worth mentioning that in the case of conductive pore fluid, the effect of surface conductivity is negligible. In this study, we consider a constant formation factor for aquifer because the cross-borehole ERT survey was conducted before beginning of heat injection did not show any indication that formation factor varies in aquifer.

In the low-temperature interval, an empirical linear dependence between temperature and fluid electrical conductivity has been proposed by (Hermans, et al., 2012; Hayley, et al., 2007; Sen & Goode, 1992).

$$\frac{\sigma_{f,T}}{\sigma_{f,10.3}} = m_f(T - 10) + 1 \quad 2.2$$

where $\sigma_{f,T}$ refers to the water electrical conductivity at temperature T in $^{\circ}\text{C}$, $\sigma_{f,10.3}$ is the water electrical conductivity at $10.3\ ^{\circ}\text{C}$ as the aquifer baseline temperature, m_f represents the slope of a fitted line for the increase in electrical conductivity per unit change in temperature $^{\circ}\text{C}$ (Figure 2.4) which is equal to 0.0194 (Hermans, et al., 2015).

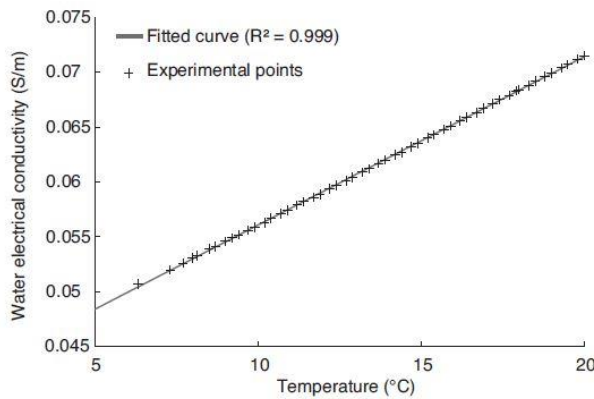


Figure 2.4 : The linear relationship between water electrical conductivity and temperature, this relationship is used to determine the bulk electrical conductivity using Archie's law (Hermans, et al., 2015).

Given that our experiment is performed in a sandy gravel aquifer, the surface electrical conductivity is negligible. On this assumption and using Archie's law allows to make a relationship between bulk and pore fluid electrical conductivity at two different subsurface temperatures (Singha & Gorelick, 2006).

$$\sigma_{f,T} = \frac{\sigma_{b,T}}{\sigma_{b,10.3}} \sigma_{f,10.3} \quad 2.3$$

Here, $\sigma_{b,T}$ represents bulk electrical conductivity, $\sigma_{f,T}$ is pore fluid electrical conductivity at a desired temperature. Considering baseline temperature $10.3\ ^{\circ}\text{C}$, $\sigma_{b,10.3}$ and $\sigma_{f,10.3}$ refer to bulk and fluid electrical conductivity respectively.

Equations 2.2 and 2.3 are integrated in order to calculate the bulk electrical resistivity for a given subsurface temperature distribution.

$$\sigma_{b,T} = \sigma_{b,10.3}((T - 10.3)m_f + 1) \quad 2.4$$

Here \mathbf{T} is a 2D/3D matrix representing the subsurface temperature distribution at a given monitoring time step t , $\sigma_{b,T}$ represents converted bulk electrical conductivity for \mathbf{T} , $\sigma_{b,10.3}$ represents the bulk electrical conductivity at 10.3 °C, \mathbf{m}_f is the change in fluid electrical conductivity per degree Celsius.

It is obvious that the electrical resistivity is inversely proportional to electrical conductivity (Equation 2.5).

$$\rho_b = \frac{1}{\sigma_b} \quad 2.5$$

The electrical forward modeling is performed using a subsurface electrical resistivity model (ρ_b) to measure the modeled apparent resistivity at each measuring point.

The resistivity method is carried out by injecting electrical current into the ground using a pair of electrodes and measuring the electrical potential between different pairs of electrodes in different locations. Electrical forward modeling is performed to model numerically the spatial distribution of electric potential and estimate apparent resistivity for a given subsurface resistivity model. To perform the electrical forward modeling, the following equation (Poisson equation) is solved (Günther, 2004):

$$\nabla (\rho_{b,t} \nabla V(\vec{r})) = -I(\delta(\vec{r} - \vec{r}_s)) \quad 2.6$$

Here $\vec{r} = (x, y, z)$ is a vector of Cartesian coordinates, $V(\vec{r})$ is the spatial distribution of electric potential, I refers to an electrical current source (Amp) located in $\vec{r}_s = (x_s, y_s, z_s)$ and δ is the Dirac delta function.

One of the main steps in the ERT data assimilation workflow is to perform electrical forward modeling for a given subsurface electrical resistivity model at each monitoring time step. In this study, the electrical forward modeling is carried out using Resipy (Saneiyan, et al., 2018), which is an open-source software to perform electrical forward and inversion modeling.

2.3.2 Cross-borehole ERT array

One of the most significant drawbacks of ERT surveys performed at the surface is the decrease in data resolution with depth. It is a fundamental physical limitation which cannot be overcome by reconfiguration of surface array or computer modeling (Loke, 2013). Theoretically, the only way to improve the vertical resolution of the data to a deeper part is to put the electrodes (source and

receiver) closer to the target. To this end, the wells are drilled, and electrodes are inserted into the wells in the vicinity of the target zone. Therefore, the cross-borehole measurements provide better vertical resolution than surface surveys.

Different arrays such as dipole-dipole, triple-pole, pole-dipole etc. have been proposed to perform cross borehole ERT survey (Figure 2.5). The downhole electrodes can be configured differently for each array, Figure 2.5 depicts dipole-dipole, triple-pole and pole-dipole and pole-pole array. It should be noted that many different custom configurations can be generated by rearranging the position of the source and receiver electrodes.

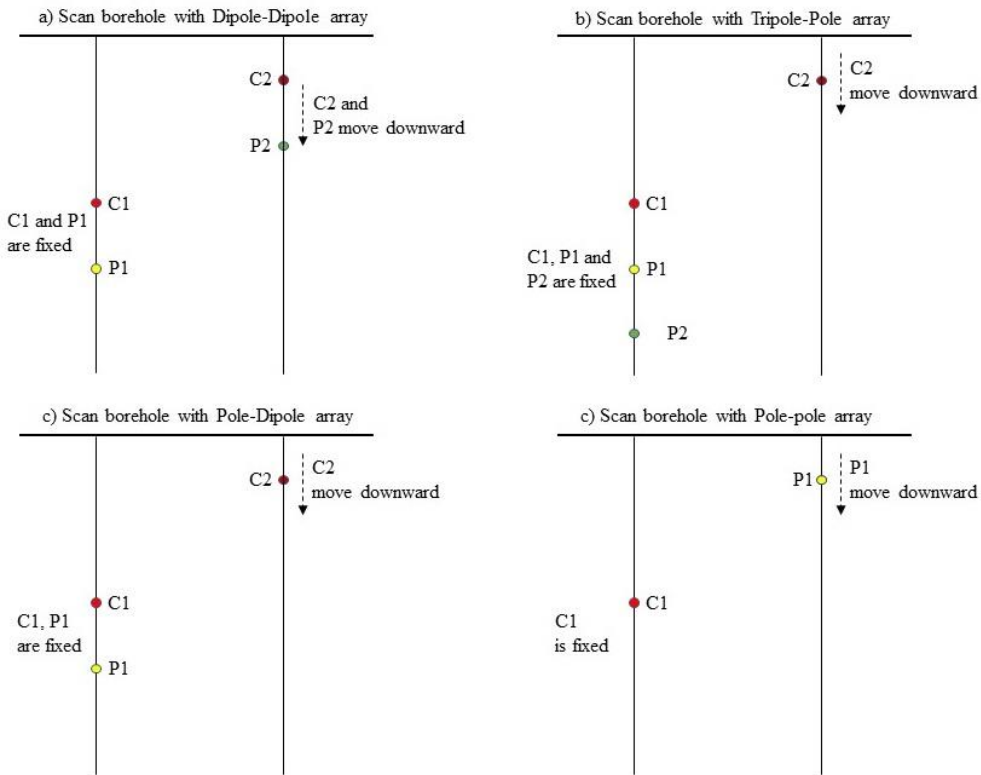


Figure 2.5 : The plot illustrates 4 types of cross-boreholes ERT arrays. a) Dipole-Dipole b) Tripole-Pole c) Pole-Dipole d) Pole-Pole. At each measuring time-step, the electrode(s) in the left borehole are freeze at their location and electrode(s) in the right borehole move from top to the bottom of borehole.

The sensitivity pattern of an array indicates the variations in measured potential by a specific electrode configuration (quadrupole) due to changes in electrical resistivity of each modeling mesh cell. Each cell has a specific amount of sensitivity so that higher amounts indicate a greater influence of the resistivity of that cell on the measured potential. Each quadrupole has a specific sensitivity pattern based on the relative position of the source and receiver electrodes.

For a given quadrupole, the sensitivity function \mathbf{S} is mentioned as the inner product of the electrical current densities $\vec{\mathbf{J}}_s$ and $\vec{\mathbf{J}}_R$, generated by an electrical current source \mathbf{I} at the source and receiver position respectively, integrated over the perturbed volume $d\mathbf{V}$ (Okpoli, 2013; A. Oldenborger, et al., 2005).

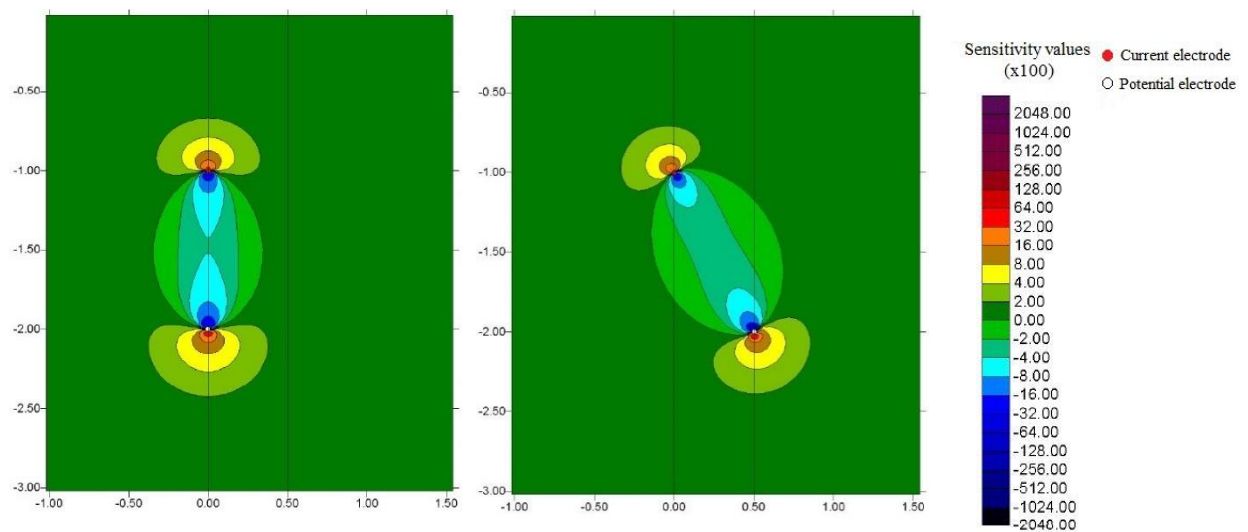
$$\mathbf{S} = \frac{1}{\mathbf{I}} \int_V \vec{\mathbf{J}}_s \cdot \vec{\mathbf{J}}_R d\mathbf{V}. \quad 2.7$$

The sensitivity pattern of several arrays for different quadrupoles was provided by Loke, (2013). In comparison with other arrays, the four-electrode dipole-dipole array has a superior sensitivity pattern as it indicates high positive sensitivity values within the cross-section of two monitoring boreholes (Figure 2.6e-f). In addition, the negative sensitivity value is limited to the zone surrounding the boreholes. Figure 2.6 illustrates the sensitivity pattern of the pole-pole (Figure 2.6a-b), dipole-pole (Figure 2.6c-d), and dipole-dipole array (Figure 2.6e-f). In dipole-dipole array, the C1-P1 (positive current electrode and potential electrode) are located in one borehole and the next pair C2-P2 in another one. It is straight forward to see that as the distance between C1-P1 and C2-P2 decreases, the positive sensitivity within boreholes' cross-section increases (Loke, 2013).

It is seen that for all arrays, the sensitivity pattern of a particular electrode configuration changes as the spacing and position of current/potential electrodes change. Providing a sensitivity model helps in selecting the best array, electrode spacing and configuration for a particular ERT survey. In this study, we avoid considering pole-pole array as it has low sensitivity to resistivity change within the cross-section of monitoring boreholes.

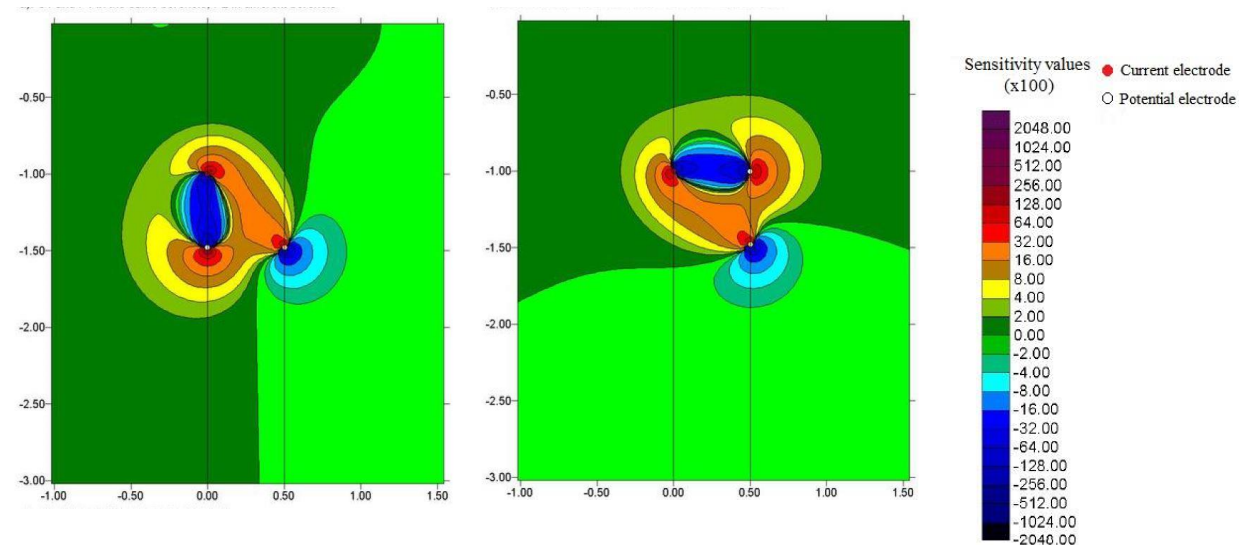
(a)

(b)



(c)

(d)



(e)

(f)

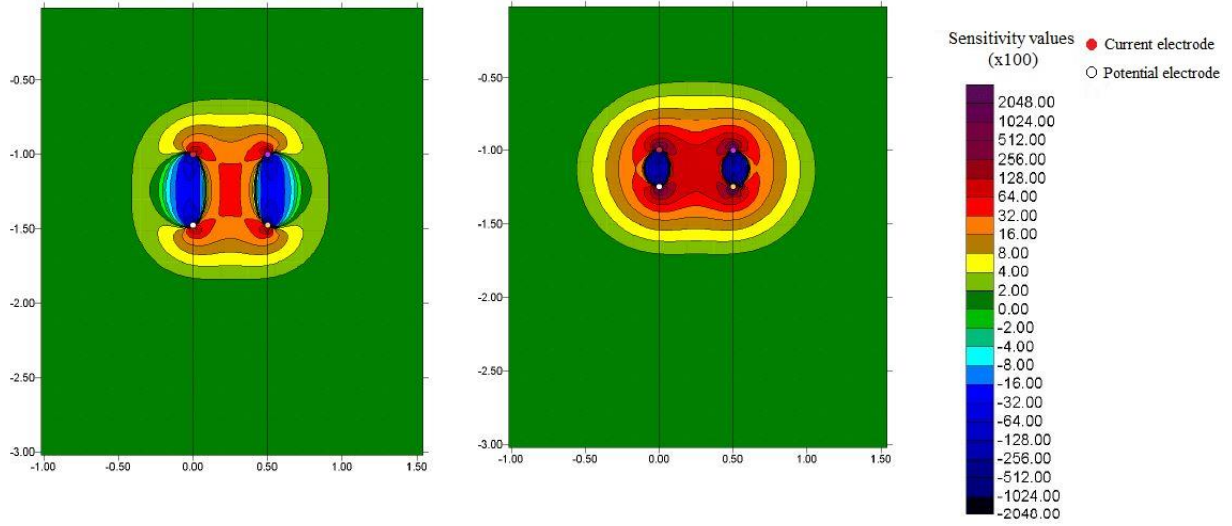


Figure 2.6 : The sensitivity pattern of two, three and four-electrode array. a & b) The sensitivity pattern of Pole-Pole array. c & d) The sensitivity pattern of Dipole-Pole array. e & f) the sensitivity pattern of Dipole-Dipole array, In this configuration the C1 and P1 located in one borehole, C2 and P2 are in other boreholes. Comparison between the section of (e) and (f) illustrates that decreasing P1-C1 and P2-C2 spacing increase the positive sensitivity quantity between boreholes (Loke, 2013).

2.3.3 Error model of ERT measurements

ERT measurement data is subject to various sources of noise (Binley, et al., 1995). For example, measurement errors are associated with poor electrode contact, equipment errors in measuring injected electric current and potential response, unpredictable environmental effect, etc. Therefore, the model error must be characterized as it plays a crucial role, either in the process of electrical inversion or data assimilation experiment.

Providing reciprocal quadrupoles in ERT array is a tool to characterize the error in measurements. The reciprocal quadrupole is provided by exchanging the position of current electrodes (P1-P2) with potential electrodes (C1-C2). The measured apparent resistivity with normal and its reciprocal quadrupole should yield an identical value due to reciprocity principle (Binley, et al., 1995). Hence any difference determines the reciprocal measurement error.

As it is shown in Figure 2.7 the measured apparent resistivity by normal quadruples is plotted versus their corresponding reciprocal errors to link two parameters. Then a reference line is fitted in the space of measured apparent resistivity and reciprocal errors on top of data. The fitted line shows the ascending trend of reciprocal errors versus measured apparent resistivity. Moreover, it is desirable to have the maximum possible amount of data falling beneath the fitted line area.



Figure 2.7 : The apparent resistivity is plotted versus reciprocal error values to make a linear error model. The linear model is utilized to predict measurement error for each quadrupole.

$$\text{Err}^m = a * R + b \quad 2.8$$

Here Err^m is the measurement error in ohm.m, R is the measured apparent resistivity (ohm.m), a and b are slope and intercept of fitted line.

Equation 2.8 was used to predict the measurement error for each normal quadrupole in cross-borehole ERT array (592 normal quadrupoles). Consequently, the corresponding error distribution of the errors provided by equation 2.8 at each ERT monitoring time step is used to generate a 2D observation error matrix ($D_{\text{err}}^m \in R^{mxN}$, section 2.4.3) to perturb the measurements (Equation 2.26) and calculate the observation error covariance matrix (Equation 2.31).

2.3.4 Time-lapse electrical inversion of DC resistivity data

Geophysical methods are based on a variety of physical fields interacting with existing materials. The task is to find a concept (or model) of the subsurface as a function of its physical properties. Given that direct measurement of physical parameters is rarely possible, in most cases the interpretation of geophysical measurements is an inverse problem (Günther, 2004).

Among the geophysical methods, direct current (DC) resistivity measurements have been used for many years to investigate the ground. The measured voltages caused by injected currents reveal information about the earth's resistivity structure.

In order to perform the electrical inversion, an iterative process resolves the following equations (Tarantola, 2005; Saneiyan, et al., 2018).

$$(\mathbf{J}^T \mathbf{W}_d^T \mathbf{W}_d \mathbf{J} + \alpha R) \Delta \mathbf{m} = \mathbf{J}^T \mathbf{W}_d^T (\mathbf{d} - \mathbf{f}(\mathbf{m}_i)) - \alpha R \mathbf{m} \quad 2.9$$

$$\mathbf{m}_{i+1} = \mathbf{m}_i + \Delta \mathbf{m} \quad 2.10$$

Here \mathbf{J} is the Jacobian, such that $J_{i,j} = \partial \mathbf{d}_i / \partial \mathbf{m}_j$, \mathbf{d} is the data vector, \mathbf{m}_i represents the parameter vector at iteration i , \mathbf{W}_d is the data weight matrix, assumed to be diagonal, with diagonal values $W_{i,i} = 1/\epsilon_i$ where ϵ_i is the standard deviation of measurement i , α is the regularization (or smoothing) parameter, R refers to the roughness matrix, which describes the connectivity of parameter blocks, $\Delta \mathbf{m}$ represents an update in parameter values at each iteration, \mathbf{f}_m is the forward model for parameters \mathbf{m} .

We are often interested in dynamic physical processes such as the heat tracing experiment and the use of ERT survey as a monitoring tool. With time-lapse ERT data sets, we are more interested in the change of electrical conductivity than in the absolute value of conductivity.

There are different strategies to compute a time-lapse inversion. The simplest is the independent inversion, in which the inversion is performed separately at each monitoring time step. The results of two consecutive time steps are subtracted to image the temporal resistivity change. However, as address by other authors, this technique accumulates the error, from one time-step to another (Miller, et al., 2008). Another strategy is called ratio or quotient inversion where the ratio of the resistivity of current time-step and the background resistivity (ratio) are calculated and inverted as apparent resistivity (Gunther and Ruckery, 2019). However, this approach is valid only for small resistivity contrasts since it does not take the sensitivity distribution as function of the real model into account.

The reference model-based strategy is another time-lapse strategy, where the models are constrained taking either first or preceding inversion results as background model for current inversion (Loke, 2001). In this case, the inversion results show the resistivity variation (ratio) rather than its absolute value.

$$\text{Ratio} = \frac{\rho_t}{\rho_{\text{ref}}} \quad 2.11$$

Here, ρ_t is inverted resistivity at time t , ρ_{ref} refers to the baseline resistivity model. This approach allows to change the array and the position of the electrodes at each time step. The time-lapse electrical inversion was performed using the open-source software BERT (Gunther and Ruckery, 2019).

2.4 Data assimilation

Data assimilation (DA) serves as a bridge between dynamic model prediction (output) and time-lapse observations taken of the system (Fletcher, 2017). DA fits the dynamic model state to the observations to improve the model output at a given time and provide a more accurate prediction of the future state of the system. The process of combining model output and observations can be solved using classical or statistical optimization approaches. The classical optimization aims to minimize an error cost function whereas the statistical approach involves minimization of the uncertainty of the model error and is based on the theory of statistical estimation (Fletcher, 2017). The Kalman filter (KF) is a statistical DA method for linear dynamic system proposed by Kalman 1960. The KF is the closed-form solution to the Bayesian filtering equations (Kálmán, 1960). Evensen (1994) proposed the idea of using an ensemble to approximate the state of linear/non-linear dynamic systems from Monte Carlo simulation point of view. The method was called the Ensemble Kalman Filter (EnKF; Evensen, 1994). In the following subsection the Bayes' rule, Monte Carlo simulation, Kalman filter and Ensemble Kalman filter are described in detail.

2.4.1 Bayes' rule

The physical systems are subject to randomness such as the unknown initial state, approximations of the complex physics, simplifying assumptions to solve the system, etc. Therefore, they must be treated as probabilistic evidence instead of deterministic evidence (Jazwinski, 2007). Bayes' theorem claims that with perfect knowledge of the present state of the system and knowing the governing rules by which the system state is evolved forward in time, one can obtain perfect knowledge of the future. Bayes' rule is based on conditional probability. We neglect the probability of $P(Y)$ to be able to calculate $P(X|Y)$ (Wiklea & Berliner, 2007):

$$P(X|Y) \approx P(Y|X)P(X) \quad 2.12$$

where X is the unknown system state, Y represents the known observations. The $P(X|Y)$ is conditional probability of X given Y which is referred to as posterior probability density function (pdf). The posterior pdf is estimated by multiplying two pdfs. First, $P(Y|X)$ is observation of the system which is called likelihood and second, $P(X)$ represents a pdf quantifying our prior knowledge about X . The product of prior and likelihood pdfs multiplication provides a pdf with same or smaller variance called posterior pdf, meaning that the posterior pdf has an equal or smaller variance than the prior. (Figure 2.8).

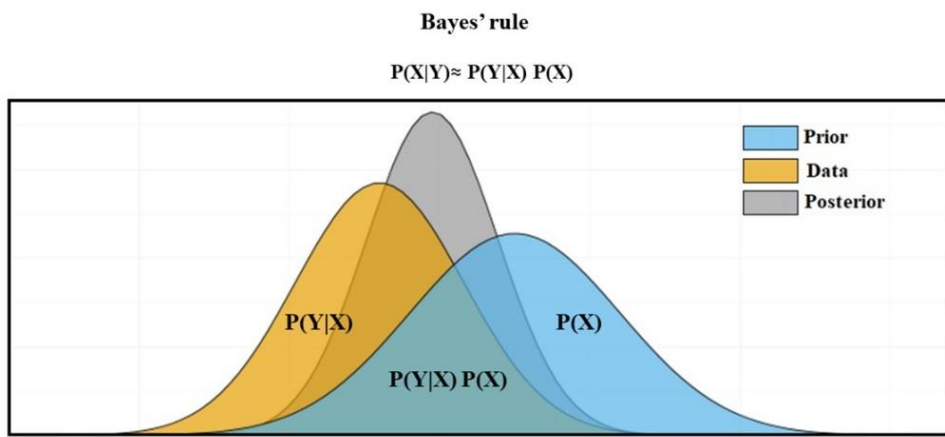


Figure 2.8 : The schematic of Bayes' rule. The multiplication of Prior and Data results in a distribution that has less variance than both initial probability distributions.

The objective of the sequential statistical DA approach is to evolve the posterior pdf forward in time (Raanes, 2016).

$$P(\mathbf{X}_{0:t}|\mathbf{Y}_{1:t}) \approx P(\mathbf{Y}_{1:t}|\mathbf{X}_{0:t})P(\mathbf{X}_{0:t}) \quad 2.13$$

The forecast pdf of $P(\mathbf{X}_t|\mathbf{Y}_{1:t-1})$ at given time t conditions to our knowledge of the system up to time step t-1 is given by Chapman-Kolmogorov equation:

$$P(\mathbf{X}_t|\mathbf{Y}_{1:t-1}) = \int P(\mathbf{X}_t|\mathbf{X}_{t-1})P(\mathbf{X}_{t-1}|\mathbf{Y}_{1:t-1})d\mathbf{x}_{t-1} \quad 2.14$$

Given that the term $P(\mathbf{X}_{t-1}|\mathbf{Y}_{1:t-1})$ at time step t=1 is equal to $P(\mathbf{X}_0)$ which corresponds to the initial prediction of the system state. Moreover, the equation 2.15 is generated based on the Hidden Markov Model (HMM) and Bayes' rule:

$$P(\mathbf{X}_t|\mathbf{Y}_{1:t}) \approx P(\mathbf{Y}_t|\mathbf{X}_t)P(\mathbf{X}_t|\mathbf{Y}_{1:t-1}) \quad 2.15$$

The equations 2.14 and 2.15 enables us to constitute a cycle to evolve the posterior pdf $P(\mathbf{X}_t|\mathbf{Y}_{1:t})$ in time by multiplying the posterior pdf of $P(\mathbf{X}_t|\mathbf{Y}_{1:t-1})$ and pdf of likelihood $P(\mathbf{Y}_t|\mathbf{X}_t)$ at give time step t.

2.4.2 Monte Carlo simulation

The idea of Monte Carlo simulation is to predict possible outcomes of an unknown variable using a set of sampled values of input variables. The input and output variables are linked by a physical function. In other words, Monte Carlo simulation perform uncertainty quantification of the output variable by specifying input variable as pdf (Tomopoulos, 2013).

Figure 2.9 depicts the Monte Carlo simulation flowchart. First, a set of random values are sampled from a predefined pdf of input variable (A) then, the possible outcomes (B) are calculated using function ($B=g(A)$), the two preceding steps may repeat over and over to produce a series of outcomes. A different set of random values of A is used at each iteration to produce a large number of likely outcomes. Finally, the pdf of variable B is provided using the recorded outcomes in the previous step in order to characterize the statistical moments of output variable B. The pdf of outcomes enables us to predict a possible range of value for B. It is unlike normal forecasting models that produce a single value as a prediction.

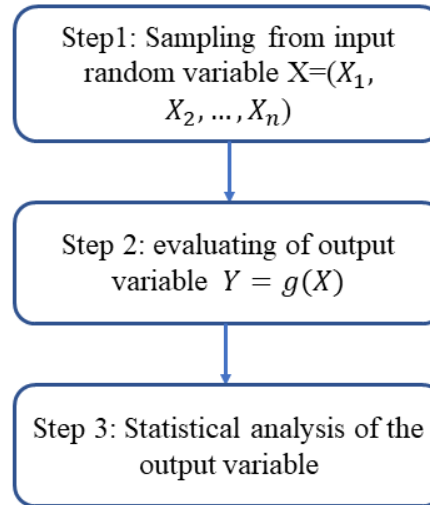


Figure 2.9 : The flowchart of Mont Carlo simulation.

2.4.3 Ensemble Kalman filter

In this subsection, an overview of KF and EnKF is given. The Kalman Filter (KF) is a solution based on Bayesian filtering equations 2.14 and 2.15 for the linear system with the assumption of linearity of the system and Gaussianity of the noise (Raanes, 2016). This assumption is considered to simplify the filtering problem since the Gaussian distribution can be characterized by its first two statistical moments (mean and variance):

$$\mathbf{X}^f = E[\mathbf{X}_t | \mathbf{Y}_{1:t-1}] \quad P^f = \text{Var}(\mathbf{X}_t | \mathbf{Y}_{1:t-1}) \quad 2.16$$

$$\mathbf{X}^a = E[\mathbf{X}_t | \mathbf{Y}_{1:t}] \quad P^a = \text{Var}(\mathbf{X}_t | \mathbf{Y}_{1:t}) \quad 2.17$$

where t is the time index, X and Y are state and observational vector respectively. The operators $E[.]$ and $Var(.)$ represents multivariate expectation and variance functions. The superscript 'f' and 'a' refers to forecast and analysis state respectively.

Considering a linear discrete time forecast and observational system (Evensen, 2009):

$$X_t^f = F(X_{t-1}^a) + q_t \quad 2.18$$

$$Y_t^o = H(X_t^f) + r_t \quad 2.19$$

where F is a forecast operator by which the state is propagated forward in time, H is the observational operator which links the state vector to the observational vector (Y_{t+1}^o). The terms q_t and r_t are the forecast and observational error vector respectively (Evensen, 2003; Raanes, 2016).

It is worth mentioning that in the context of data assimilation, the desired variable to be updated is referred to as a state variable (X). In addition, we have observations (Y^o) and measurements y^m ; In fact, both observation and measurement are the same variable except that the observations are computed by numerical models, but the measurements are real laboratory/field data.

KF is a powerful method to assimilate the linear system. Kalman filter uses an equation to evolve the second-order statistics forward in time to predict error statistics for the model forecast. In non-linear systems the higher-order statistics need to be integrated in time to predict error statistics which, in most cases is beyond our computational capabilities. Hence, KF fails to handle the complexity of non-linear systems (Evensen, 2009). Evensen (1994) proposed the Ensemble Kalman Filter (EnKF) method to address the KF shortcoming associated with the non-linearity of the system. EnKF method is a Monte Carlo approximation of the traditional template of KF. The ensemble (E) refers to a bunch of scenarios/realizations are provided by simulation; the mean of the realizations is supposed to represent the true state of the system:

$$E = \begin{bmatrix} x_1 \\ \vdots \\ x_n \end{bmatrix} \quad 2.20$$

$\{x_{1:n}\}$ represents the realizations of the system state, so the matrix $E \in R^{n \times N}$, each row shows the expected values for a specific location of the simulation domain. n is the number of parameters of the model to be updated and N is the size of ensemble. In literature, a range of ensemble size

of 50-100 members have been mentioned as a reasonable quantity. However, one of our sub-objectives is to investigate the optimal ensemble size for the current study.

The EnKF consists of the recursive application of two main steps: the forecast and the analysis. During the forecast step, the state is propagated in time and the observational vector is calculated for a given time step, then the state vector is updated during analysis step (Evensen, 2009). The forecast and analysis steps will be discussed in the following.

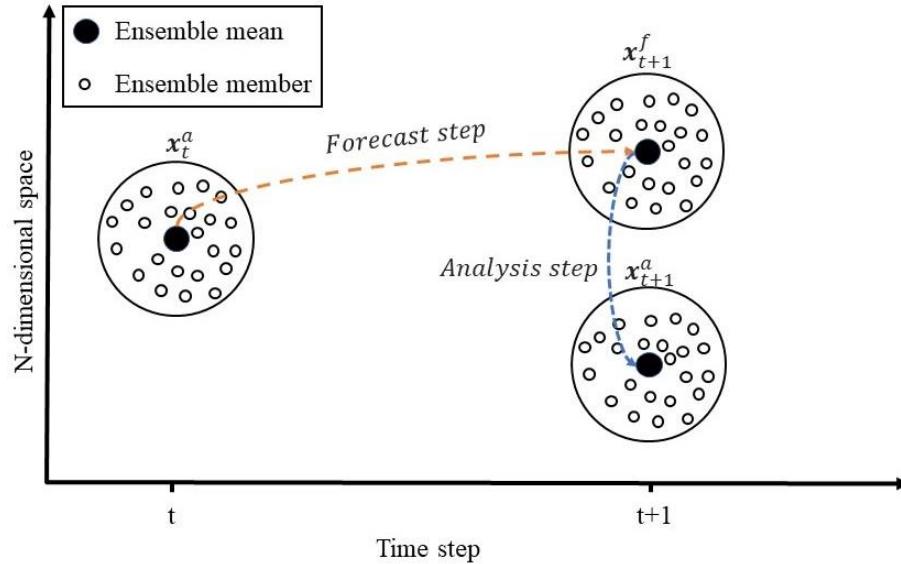


Figure 2.10 : The schematic of forecast and analysis steps of EnKF.

- Forecast step:

The state variable needs to be initialized before the assimilation experiment begins. The initial state vector is provided according to our best prior knowledge of the state variable. For instance, in the context of hydrogeology, the geological map, Slug test, lithological logs could be considered as prior knowledge concerning subsurface K distribution.

According to Equation 2.21, at a given time t , the analysis state vector (\mathbf{X}_{t-1}^a) is integrated forward in time by means of forecast operator (\mathbf{F}) to predict the forecast state vector in next time step t (forecast state vector (\mathbf{X}_t^f)), \mathbf{q}_t is the forecast error vector. It should be noticed that at $t=0$, \mathbf{X}_0^a corresponds to the initial state vector (Raanes, 2016).

$$\mathbf{X}_t^f = \mathbf{F}(\mathbf{X}_{t-1}^a) + \mathbf{q}_t \quad 2.21$$

Equation 2.21 can be expressed as the following matrix form [26]:

$$\mathbf{E}_t^f = \mathbf{F}(\mathbf{E}_{t-1}^a) + \mathbf{Q}_t \quad 2.22$$

where \mathbf{E}_t^f is the forecast state ensemble at the time step t , $\mathbf{E}_t^f \in \mathbb{R}^{n \times N}$, where n refers to the number of parameters to be updated and N is the ensemble size. \mathbf{E}_t^a is the analysis state ensemble at the time step t . \mathbf{Q}_t is the forecast error matrix which is provided by sampling from a white Gaussian noise distribution with mean zero and covariance matrix $\bar{\mathbf{C}}^f$. Each element of the covariance matrix $\bar{\mathbf{C}}^f$ is calculated as the following (Wu & Zheng, 2017):

$$\bar{\mathbf{C}}_{i,j}^f = \frac{1}{N-1} (\mathbf{E}_{i,1:N}^a - \bar{\mathbf{E}}_i^a) \cdot (\mathbf{E}_{j,1:N}^{K,a} - \bar{\mathbf{E}}_j^a)^T \quad 2.23$$

Here $\bar{\mathbf{E}}_i^a$ is the mean of i^{th} row in the forecast state ensemble.

- Analysis step:

The forecast state vector (\mathbf{X}_t^f) was computed during forecast steps. The analysis step aims to update \mathbf{X}_t^f based on the difference between measurement and observation vector. Regarding to equation 2.24 the forecast error vector is reinitialized at each monitoring time step (Evensen, 2009):

$$\mathbf{X}_t^a = \mathbf{X}_t^f + \bar{\mathbf{K}} \{ \mathbf{y}_t + \mathbf{r}_n - H(\mathbf{X}_t^f) \} \quad 2.24$$

where \mathbf{X}_t^a is the analysis state vector, \mathbf{r}_n is random error, which is added to measurements, $H(\mathbf{X}_t^f)$ represents the observation vector (Equation 2.24). The term y refers to any field, laboratory or any type of measurements that is used to update the state vector. The equation 2.24 can be given as the following matrix form (Raanes, 2016):

$$\mathbf{E}_t^a = \mathbf{E}_t^f + \bar{\mathbf{K}} \{ \mathbf{y}_t^{\text{prd}} - H(\mathbf{E}_t^f) \} \quad 2.25$$

Here the \mathbf{E}_t^a stands for analysis state ensemble, \mathbf{E}_t^f represents forecast state ensemble, $H(\mathbf{E}_t^f) \in \mathbb{R}^{m \times N}$ is the observational ensemble, where m is the number of measurements, and \mathbf{y}_{prd} is the perturbed measurements (Equation 2.26).

$$\mathbf{y}_t^{\text{prd}} = \mathbf{y}_t + \mathbf{D}_{\text{err}}^m \quad 2.26$$

At a given monitoring time step t , a vector of measurements $\mathbf{y}_t \in \mathbb{R}^{m \times 1}$ is available. $\mathbf{D}_{\text{err}}^m \in \mathbb{R}^{m \times N}$ is an iid sample from a white Gaussian error model which is added to the vector of measurements

to create the perturbed measurement ensemble ($\mathbf{y}_t^{\text{prd}} \in \mathbb{R}^{mxN}$). $\bar{\mathbf{K}}$ refers to Kalman Gain (KG). The KG determines to which degree the \mathbf{E}_t^f is updated for a given observation and measurement. In better words, KG determines the contribution of measurements to update the state.

KG is calculated as the following (Raanes, 2016):

$$\bar{\mathbf{K}} = \bar{\mathbf{C}}_{\text{err}}^f \mathbf{H}^T (\mathbf{H} \bar{\mathbf{C}}_e^f \mathbf{H}^T + \mathbf{C}_{\text{err}}^m)^{-1} \quad 2.27$$

Here $\bar{\mathbf{C}}_{\text{err}}^f$ represents the forecast error covariance matrix, \mathbf{H} is a matrix that transforms the state to the observation space. $\mathbf{C}_{\text{err}}^m$ is the measurement error covariance matrix.

The matrix form of the KG equation is as follows:

$$\bar{\mathbf{K}} = \mathbf{A} \mathbf{Y}_{\text{an}}^T (\mathbf{Y}_{\text{an}} \mathbf{Y}_{\text{an}}^T + (N - 1) \mathbf{C}_{\text{err}}^m)^{-1} \quad 2.28$$

where, the equations 2.29 to 2.30 represent the anomaly of state ($\mathbf{A} \in \mathbb{R}^{nxN}$) and observation ($\mathbf{Y}_{\text{an}} \in \mathbb{R}^{mxN}$) respectively. The observation error covariance matrix ($\mathbf{C}_{\text{err}}^m \in \mathbb{R}^{mxm}$) is estimated using Equation 2.31.

$$\mathbf{A} = \begin{bmatrix} \mathbf{X}_1 - \bar{\mathbf{X}}_1 \\ \vdots \\ \mathbf{X}_n - \bar{\mathbf{X}}_n \end{bmatrix} \quad 2.29$$

$$\mathbf{Y}_{\text{an}} = \begin{bmatrix} \mathbf{Y}_1^o - \bar{\mathbf{Y}}_1^o \\ \vdots \\ \mathbf{Y}_m^o - \bar{\mathbf{Y}}_m^o \end{bmatrix} \quad 2.30$$

$$\mathbf{C}_{\text{err}}^m = \frac{\mathbf{D}_{\text{err}}^m \mathbf{D}_{\text{err}}^m^T}{N - 1} \quad 2.31$$

The size of state ensemble is $n \times N$, and the observational ensemble has the size of $m \times N$. Given that, $N \ll m \ll n$ at each iteration a matrix with size of $n \times m$ which is the product of KG multiplied by the anomaly of observation and measurement (Equation 2.25) is stored. It is possible to reformulate equation 2.25 in order to avoid computing such a large matrix:

$$\mathbf{A}^a = \mathbf{A} + \mathbf{A} * \mathbf{B} \quad 2.32$$

$$\mathbf{B} = \frac{\mathbf{Y}_{an}^T}{\mathbf{Y}_{an}\mathbf{Y}_{an}^T + (N - 1)\mathbf{C}_{err}^m} (\mathbf{y}_t^{prd} - \mathbf{Y}_{an}) \quad 2.33$$

Hence, at each iteration matrix $\mathbf{B} \in R^{N \times N}$ is computed which is significantly smaller than matrix with size of $n \times m$.

The analysis state can be treated as the weighted average of the model forecast and observations (Wu & Zheng, 2017). The weights are calculated by KG which is proportional to the model and observation covariance matrix. Therefore, the two preceding covariance matrices determine the degree to which forecast state ensemble is updated during analysis step. If these error covariance matrices are estimated correctly, then the analysis state can gradually converge to a true state during assimilation experience.

Using the finite ensemble size to approximate the error covariance matrices poses a problem in the assimilation experiment. This problem leads to spurious correlations over long distances between state variables and observations that are supposed to be uncorrelated. The spurious correlation results in a spurious update to the state variable at each analysis step. The spurious updates may be insignificant in terms of ensemble mean change, but they reduce the ensemble variance (Evensen, 2009). Theoretically, increasing the ensemble size can cancel out the spurious correlation effect. But it is not always possible in practice. The numerous ensemble member raises the assimilation running time dramatically. The inflation technique is used to compensate for the ensemble variance reduction (Wu & Zheng, 2017). There are two ways to implement this technique; first, the additive inflation by which an error is added to the ensemble forecast matrix at each assimilation iteration. Secondly, the multiplicative inflation technique. In this study, the error covariance matrix is multiplied by an inflation factor of 0.01 at each assimilation iteration.

3 Results

In this chapter, the proposed workflow (Figure 2.1) of our assimilation method and the results of its application on the Aquifroid field site are presented.

3.1 Geostatistical simulations

The K is the state variable to be updated using ERT data assimilation (section 2-3-6). An initial ensemble of 100 equiprobable 3D K realizations was generated using unconditional SGS approach based on prior information from field measurements. The SGS simulation was carried out using SGeMS (Remy, et al., 2009), an open-source geostatistical simulation software. The simulation parameters are a Gaussian variogram with a variance of 0.999 and nugget effect of 0.001. Figure 3.1 illustrates one random realization of the initial ensemble of K. Since we did not have enough data to compute an accurate variogram model, we had to approximate the variogram parameters, considering that the K distribution covers a range of possible values of K based on the filed measurement and literature (Talbot Poulin, et al., 2013).

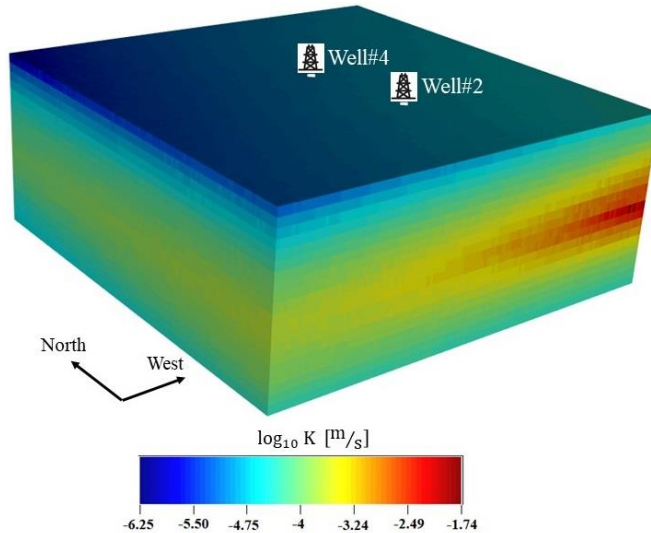


Figure 3.1 : The 3D distribution of sandy gravel aquifer hydraulic conductivities ($\log_{10} K$ [m/s]) provided by SGS. The location of Pumping (Well#4) and injection (Well#2) well was shown.

3.2 Cross-borehole ERT measurements

The Time-lapse Cross borehole ERT measurements were carried out in a cross-section of the Well #2 and Well #4, which is perpendicular to the natural groundwater flow direction. The electrode array configurations of Dipole-Dipole, Pole-Dipole and Pole-Tripole were acquired to

conduct a monitoring cross-borehole ERT survey (Loke, 2013). All possible combinations of electrodes were considered, except those with two current electrodes in the same well, as they cause a short-circuit between the current electrodes. Finally, the measuring sequence consists of 596 pairs of normal and reciprocal quadrupoles that took approximately 30 minutes to run. Due to the presence of clay layers overlying and underlying the sandy-gravel aquifer (Figure 1.11b), the ERT measuring time was set up to 500 milli-seconds to remove any induced polarization (IP) effects on direct current (DC) measurements.

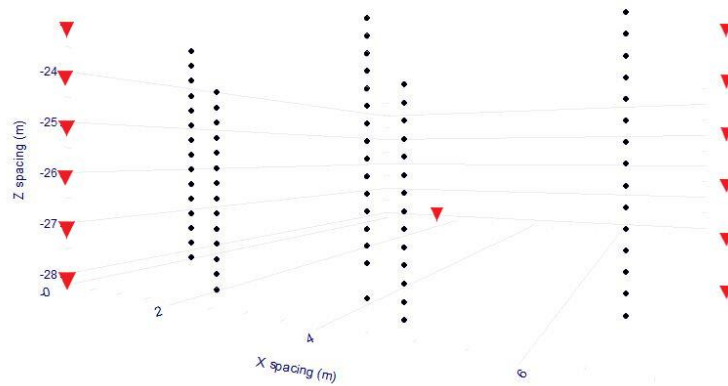


Figure 3.2 : The upside-down red triangles represent the location of downhole electrodes and black circles in the middle of panel are cross-borehole ERT measuring points. The plot was prepared using Electre-Pro software (Truffert, 1990).

3.2.1 Evaluation of cross-borehole ERT monitoring data

The cross-borehole ERT measurement was carried out for 11 time-steps. It is important to qualitatively check if the acquired ERT data contain information about the heat injection experiment. We considered two steps to evaluate the quality of monitoring data. The evaluation consists of checking the variation of the mean value of measured apparent resistivity for each dataset over the time and then a time-lapse electrical inversion was carried out.

3.2.1.1 Mean apparent resistivity variation

A total of 11 cross-borehole ERT surveys were conducted during a period of 7 consecutive days. All data sets were filtered in terms of outliers then the cross-borehole ERT measurements, whose reciprocal errors were more than 10% of their measured apparent resistivity values were eliminated from data set (Binley, et al., 1995) before calculating the mean apparent electrical resistivity (section 2-3-3). The mean apparent electrical resistivity for the background data set was 42.55 (ohm.m). As expected, the apparent resistivity decreased during the heated water injection

phase by 9% and started increasing during the recovery phase after the end of heat injection (Figure 3.3).

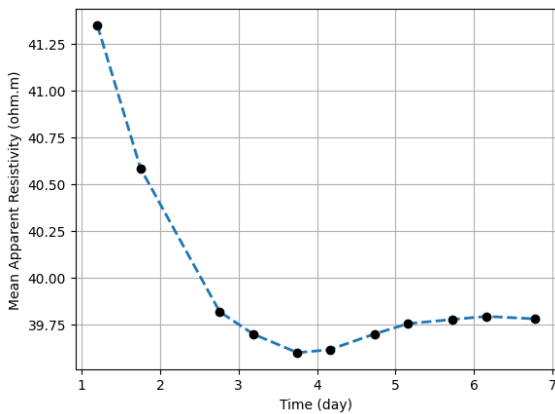


Figure 3.3 : The mean apparent resistivity (ohm.m) of each ERT monitoring time-step dataset versus the time after the beginning of heat injection experiment.

3.2.1.2 Time-lapse electrical inversion

A time-lapse electrical inversion was performed to ensure that the cross-borehole ERT data is informative enough to use in the data assimilation experiment. The reference model-based was used as the inversion strategy (read section 2-5-4). The maximum curvature of the L-curve approach was used to optimize the regularization coefficient (Günther, et al., 2006).

Before inverting cross-borehole ERT data sets, it is required to filter out the measurements whose reciprocal error is more than 10% of their own value. Figure 3.4B illustrates the time-lapse inverted models. The maximum change in resistivity is observed at the center of plume, where the ratio is equal to 0.4, According to the coefficient of water electrical conductivity change per unit temperature change (Equation 2.2), the resistivity change corresponds to 3.03 °C subsurface temperature increase. It is easy to see that the decrease in resistivity/temperature rise is higher at the center of the plume than at the front. Regarding the inversion results, the heat plume expands during the first two days of heat injection and then shrinks slightly during recovery time. In addition, the plume has mostly spread at the bottom of the aquifer where lithological logs show a greater amount of gravel corresponding to a higher K value. The inversion results shows that the plume propagate toward the well#4 after 41.5 hours. The corresponding depth represents the gravel layer at the bottom of the aquifer that leads the heat faster toward well#4; the anomaly keeps existing there for 40 hours and then it starts disappearing as expected during the recovery phase.

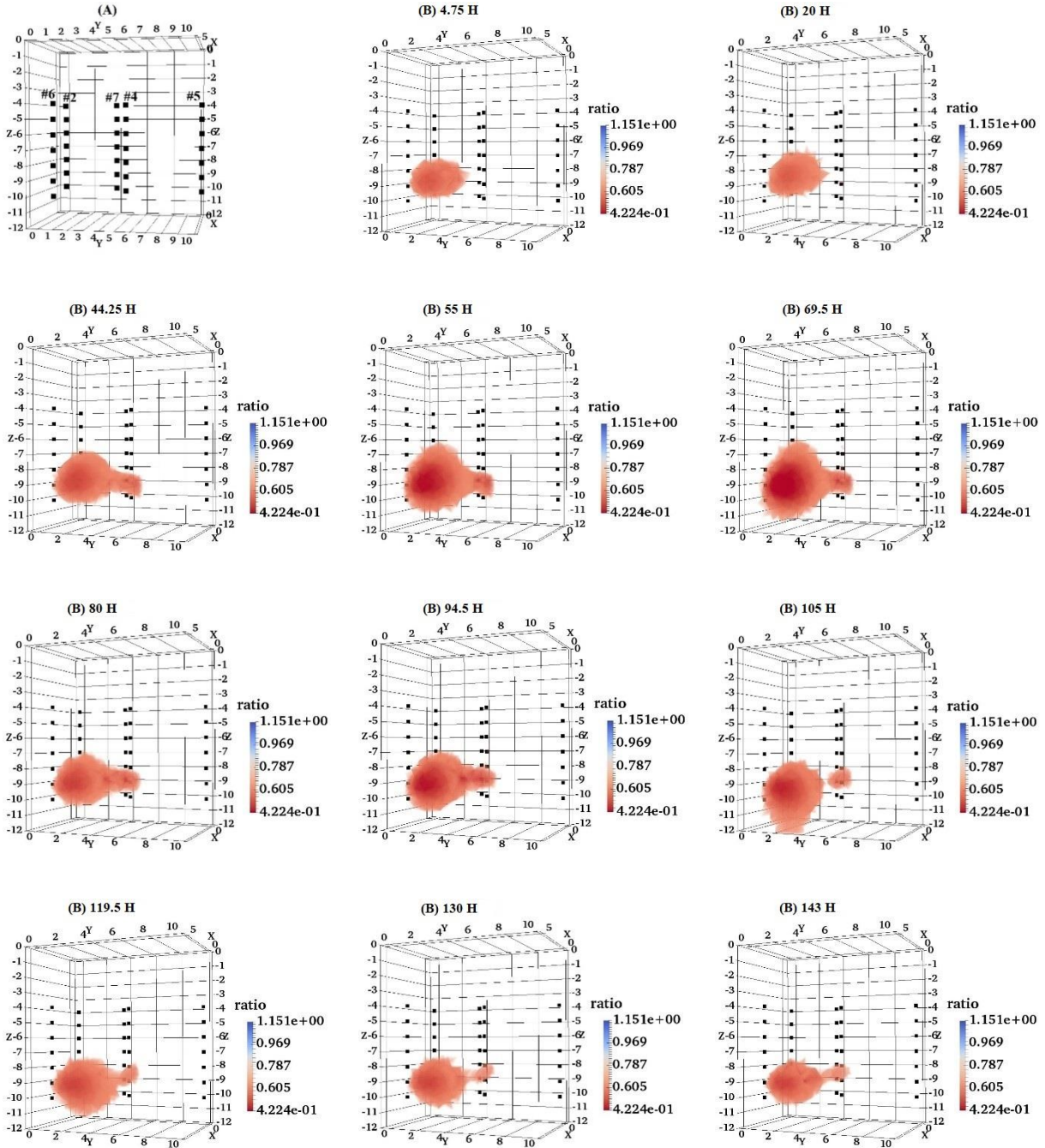


Figure 3.4 : A) Position of wells B) The time-lapse inversion results of 14 time-step ERT monitoring. Each result represents the ratio of current time-step resistivity model and the base-line resistivity model. Square dash line marks the screen part of wells from the depth of 24 m to 30 m.

3.3 Model of measurement error

The ERT measurement error estimation is crucial for both electrical inversion and data assimilation experiment as the accuracy of the results is subject to ERT measurement error. The

magnitude of the ERT measurement error plays an important role to perturb measurement and to calculate error covariance matrix. In this study, reciprocal error was used to qualify the ERT measurement error quantitatively. For all monitoring time step, each pair of normal and reciprocal measurements is used to construct a linear error model by which the measured apparent resistivity and the reciprocal error are linked together (Figure 3.5).

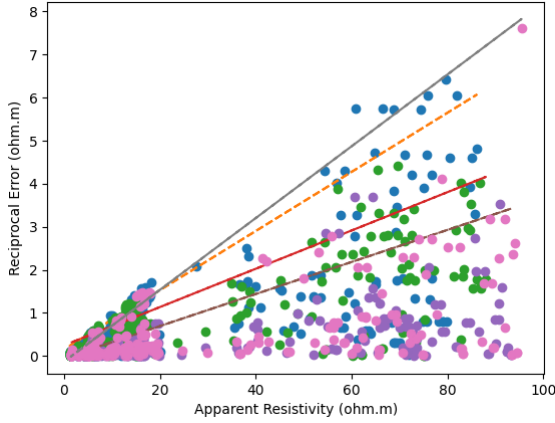


Figure 3.5 : The colored circles represent five measured apparent resistivity dataset versus reciprocal error in different colors. The fitted lines are linear error model. The linear error model is used to predict measurement error for each quadruple in cross-borehole ERT array.

The measurement error is estimated for each quadruple using linear error models. Consequently, a data vector containing the measurement errors is provided for each monitoring time step. The pdf of the measurement errors allows us to generate random errors for each monitoring time step. Random errors are used to perturb the cross-borehole ERT measurements ($\mathbf{D}_{\text{err}}^{\text{m}}$) and to create an observation error covariance matrix (\mathbf{R} , read section 2-6-3).

3.4 Assimilation results

First of all, it is favorable to introduce the main input parameters of assimilation experiments. The initial ensemble of K (\mathbf{E}_0^a) is generated by geostatistical simulations. At each assimilation iteration, the simulated temperature distribution resulting from the numerical model of heat injection, is converted into bulk electrical resistivity. The observation ($H(\mathbf{E}_t^f)$) is the simulated apparent resistivity provided by electrical forward modeling. Measurement (\mathbf{y}_t) are time-lapse cross-borehole ERT field measurements.

The cross-borehole ERT data is considered to be a better tool than the solely monitoring groundwater temperature data in estimating the three-dimensional spatial extent of a heat plume (Figure 3.4B). The cross-borehole ERT data provides significantly higher spatial coverage and resolution. Moreover, the electrical forward modeling result is strongly dependent on the accuracy

of the estimated subsurface temperature (spatial geometry of heat plume) by numerical model of groundwater flow and heat transfer. On the other hand, the estimated geometry of heat plume reflects the accuracy of estimated distribution of K in the aquifer. Hence, being able to replicate cross-borehole ERT data at each monitoring time step was considered an important criterion for the success of the cross-borehole ERT data assimilation experiment to estimate the heterogeneity of aquifer K.

The observation datasets were divided into assimilation and prediction datasets to evaluate the accuracy of the approach. The first nine time-steps were used for data assimilation, while the last two were used to predict the future state of the system. In more details, firstly, the ERT data were assimilated to update the ensemble of K; while in the second step, we skip the ERT data assimilation step of flowchart (Figure 2.1) to see if the numerical model of groundwater flow and heat transfer (using updated ensemble of K) is able to predict the future state of the groundwater temperature accurately.

The results are plotted in Figure 3.6, where we show the mean measured and forecasted apparent resistivity plots over the 11 time-steps for different ensemble size. A comparison of the three plots in Figure 3.6 clearly shows that, increasing the ensemble size results in a better fit between the forecasted apparent resistivity and the field measurements.

The data assimilation experiment starts with 20 realizations (Figure 3.6a). Due to the small ensemble size, the EnKF was not able to converge to an unbiased estimation, the variance of simulated apparent resistivity decreased dramatically up to the ninth time step that marks the end of data assimilation and the predicted apparent resistivity were overestimated. To handle these shortcomings, the ensemble size was increased to 40 realizations (Figure 3.6b), which improved the match between forecasted apparent resistivity with measured apparent resistivity while the ensemble variance didn't collapse. However, the results are required to be modified.

The Figure 3.6c demonstrates a fair match between forecasted and measured apparent resistivity, as almost all measured apparent resistivity falls within the range of forecasted ones. The forecasted apparent resistivities in the two predictions time-steps converge toward measured apparent resistivity indicating that simulated subsurface electrical resistivity which is computed by combination of the numerical model of groundwater flow and heat transfer using posterior K ensemble and petrophysical relationship can replicate the actual subsurface electrical resistivity. These results were obtained with an ensemble of 60 realizations. With this number of realizations, the EnKF avoided filter divergence and variance collapse, and it was obtained at a reasonable computational cost. The running time is approximately 72 hours to assimilate an ensemble of 60

realizations for 11 monitoring time-steps. The simulation was run using a laptop with intel Core i9 processors (8 x 2.4 GHz) and 16 GB RAM.

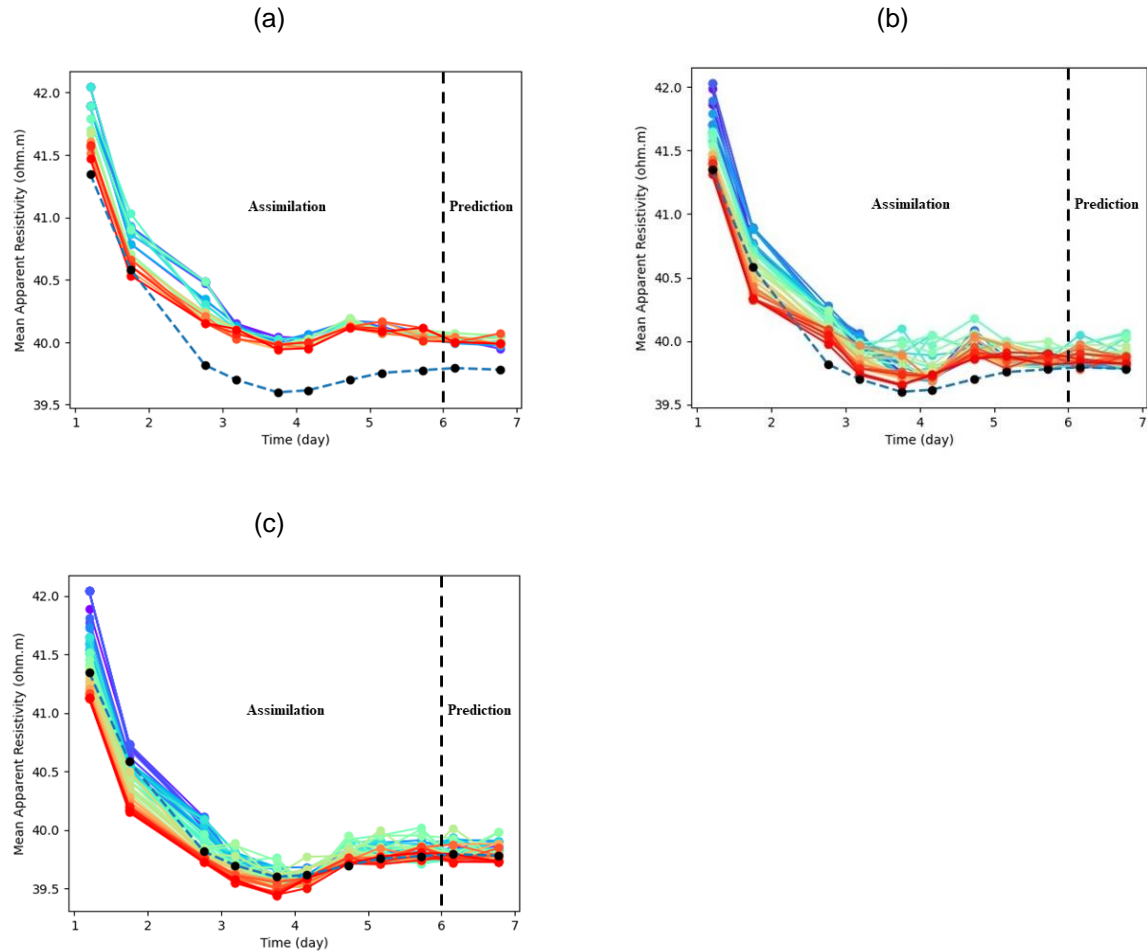
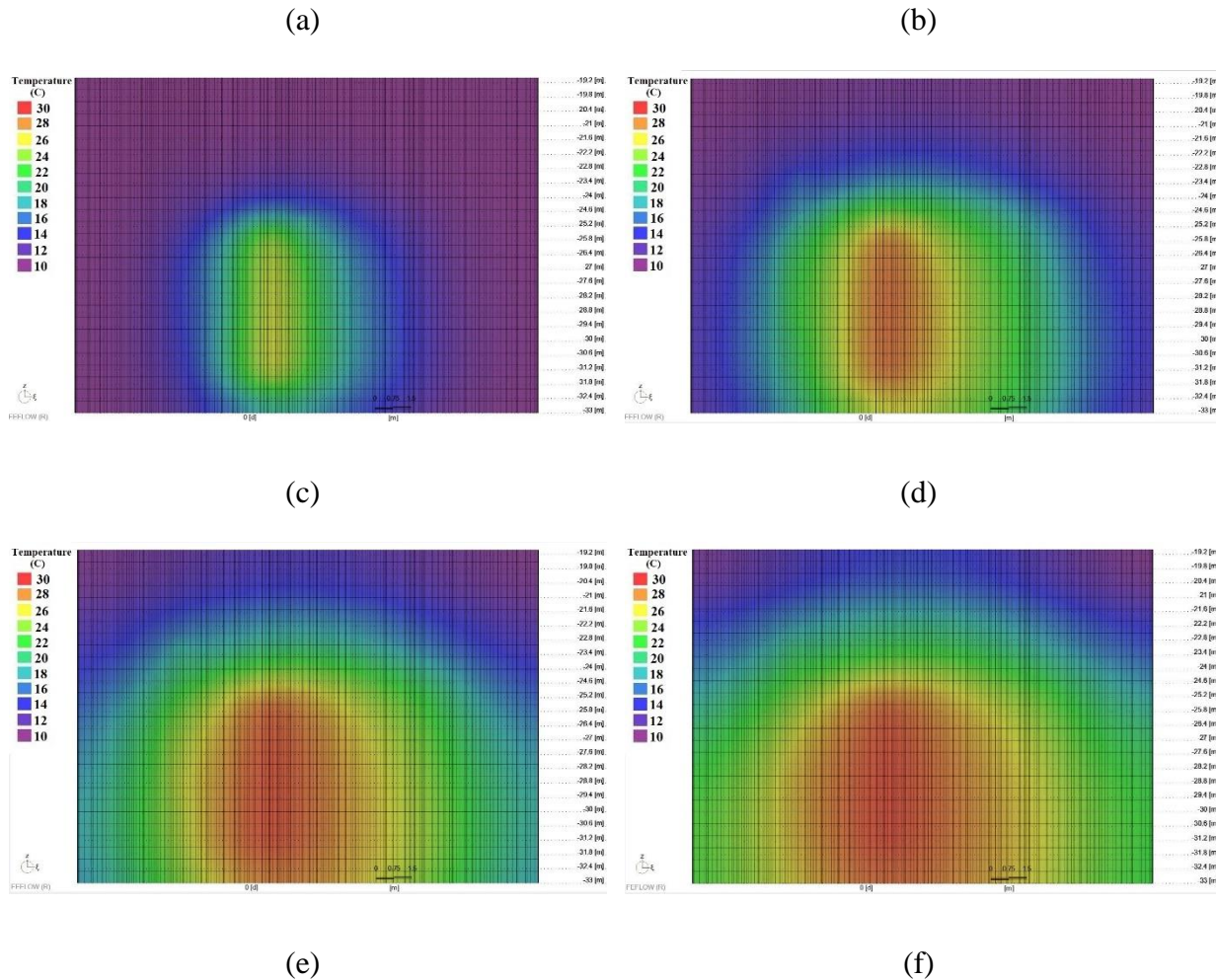


Figure 3.6 : The dash line represents mean apparent resistivity of field measurements. The colored ones are simulated values by electrical forward modeling for each ensemble member versus time after the beginning of heat injection. (a, b and c) demonstrate the same information for 20, 40 and 60 ensemble members respectively.

Figure 3.7 shows the simulated groundwater temperatures for sixty realizations in cross-section of Well #2 and Well #4. The propagation and shrinkage of heat plume during heat injection and recovery phases is clearly illustrated. Moreover, we compared simulated and measured temperature from a temperature sensor located at a depth of 28 m at Well #4. Figure 3.8 shows the simulated groundwater temperatures compared to the measured temperature during the injection and recovery period. Although during the first two monitoring steps, the simulated temperatures do not converge to the measured temperature, after the third time-step they converge to the actual measurements.

We detected the heat plume for the first time by the temperature sensor at the depth 28 m of Well #4. So, we assumed that its recorded temperature data is not affected by the temperature change in other depth hence this temperature sensor was chosen to validate the results. It is worth mentioning that the temperature data neither were assimilated during the assimilation experiment nor were used to calibrate the numerical model of groundwater flow and heat transfer. This is further evidence that the posterior K distribution estimated by our assimilation workflow converges to an unbiased estimate of the subsurface hydraulic conductivity model.



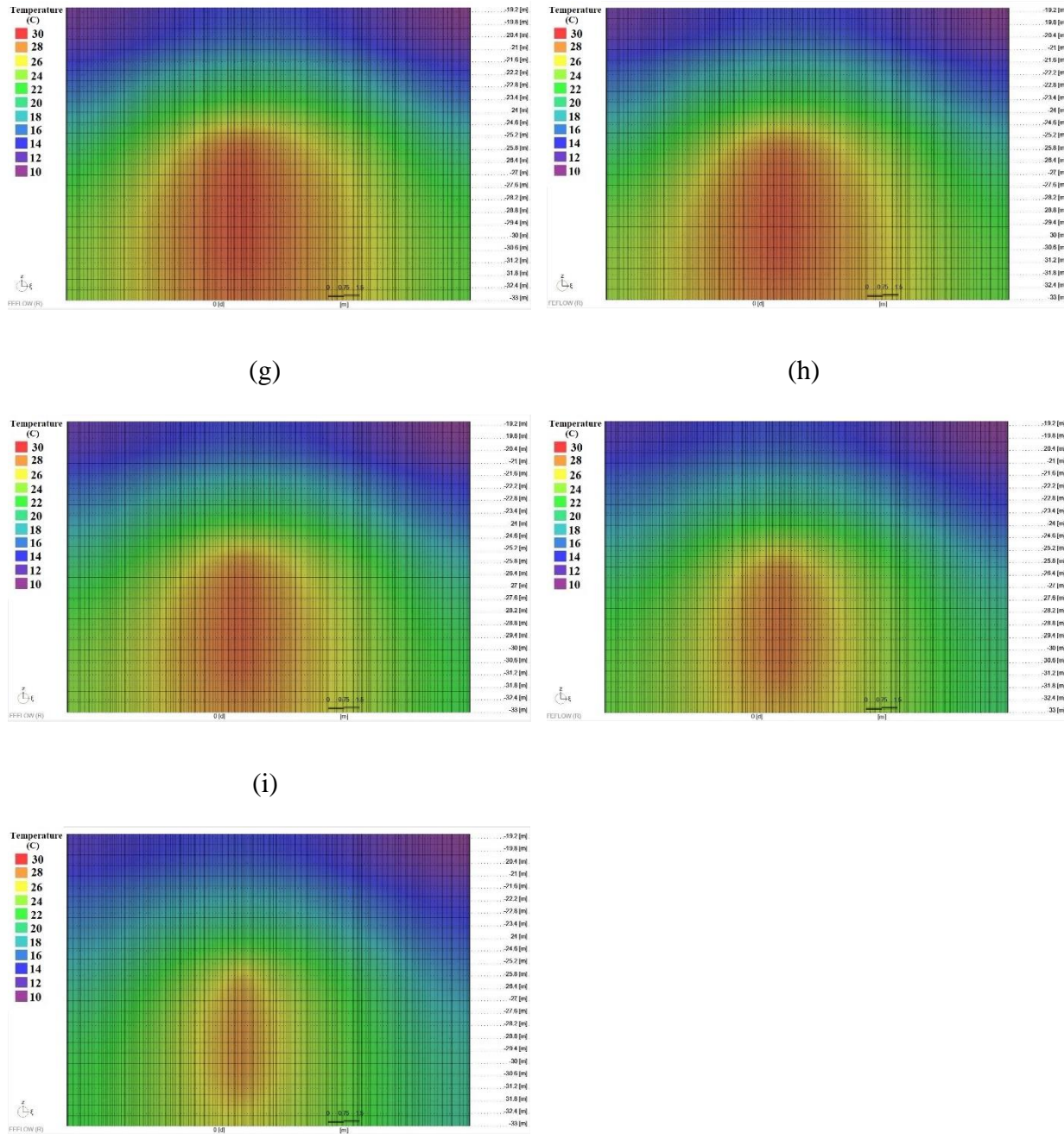


Figure 3.7 : The average simulated temperature of sixty realizations in cross-section of Well #2 and Well #4 for all assimilation time-steps.

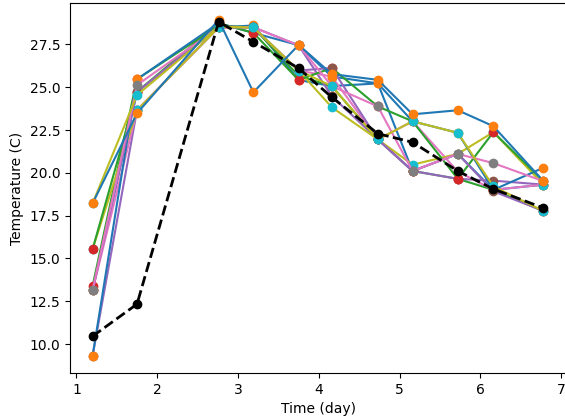


Figure 3.8 : Dash line is the measured temperature at the depth 28 m of well#4. The colored solid lines represent the simulated groundwater temperature of sixty realizations at the depth 28 m of well#4.

The prior and posterior distribution of K ensemble of size 60 is presented in Figure 3.9. In addition, the mean and standard deviation (std) of K distribution, prior and post assimilation experiment is reported to give an idea about K distribution change due to cross-borehole ERT data assimilation. The standard deviation value of K decreased through the assimilation experiment, but it did not collapse. After nine steps of cross-borehole ERT data assimilation, the mean value of K converged to the geometric mean of slug tests results (Talbot Poulin, et al., 2013), although the initial K distribution is negatively biased compared to direct measurement with slug tests.

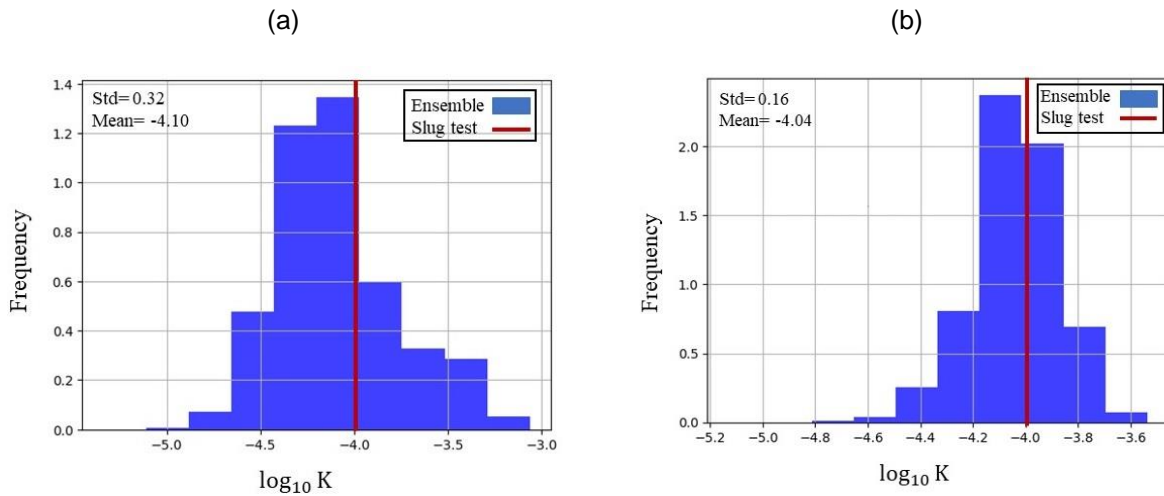
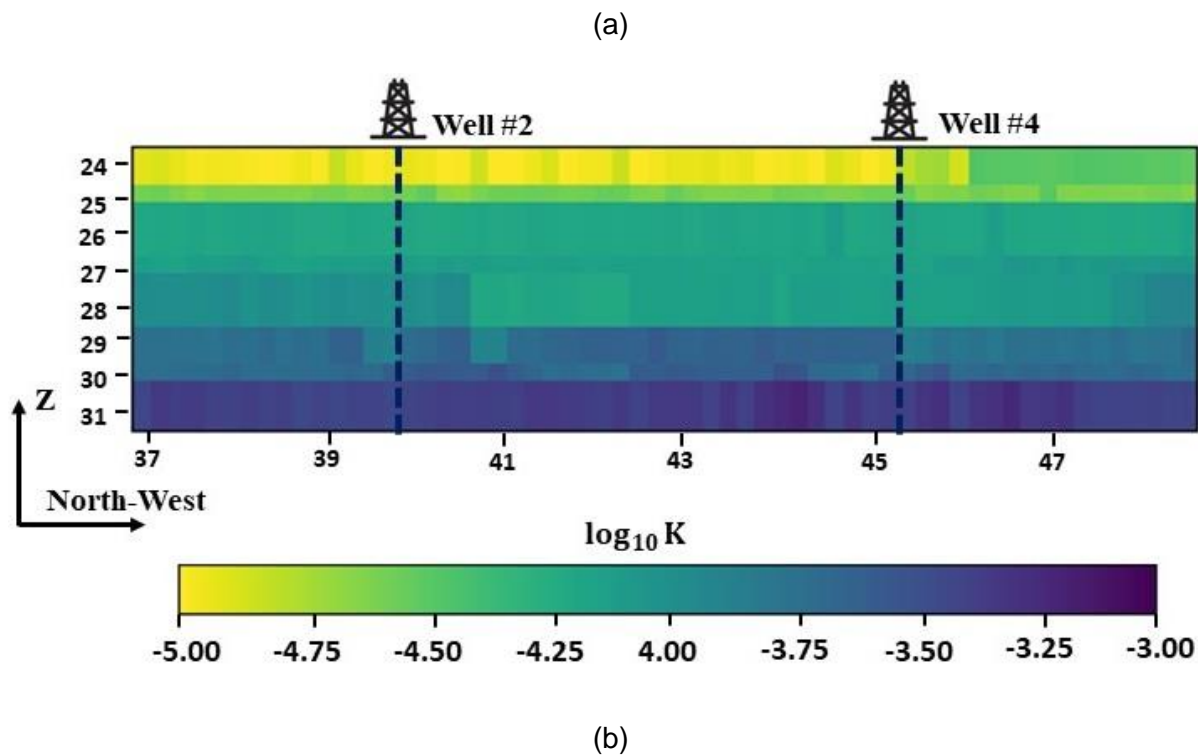
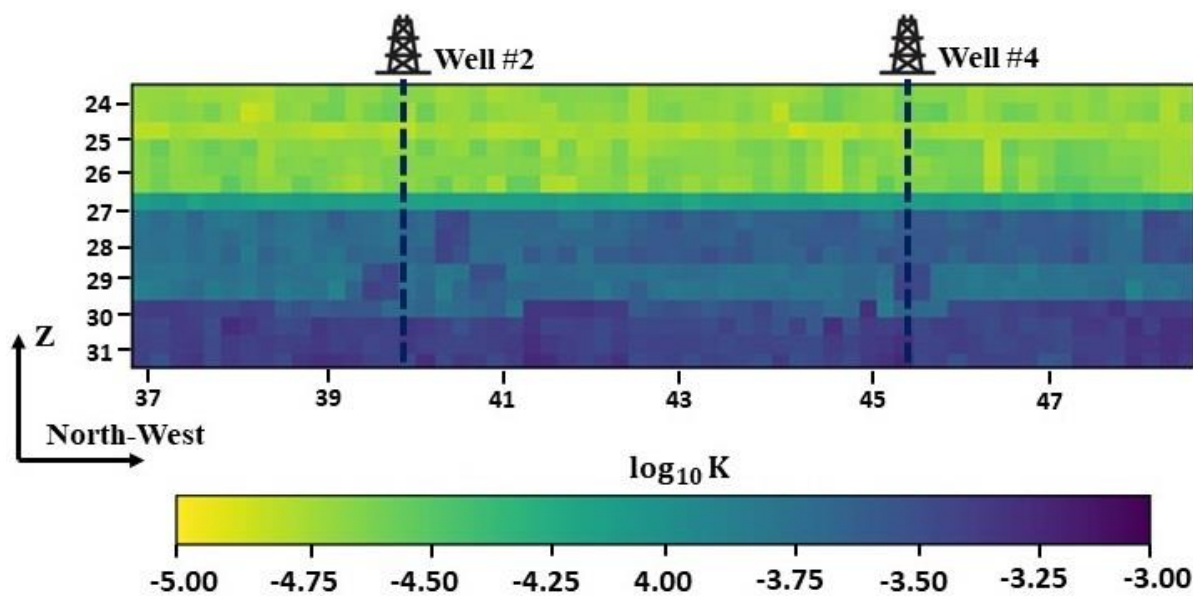


Figure 3.9 : a) Initial K distribution of ensemble before the beginning of the assimilation experiment. b) posterior K ensemble distribution after nine assimilation steps. The vertical red line marks the geometric mean of slug tests result.

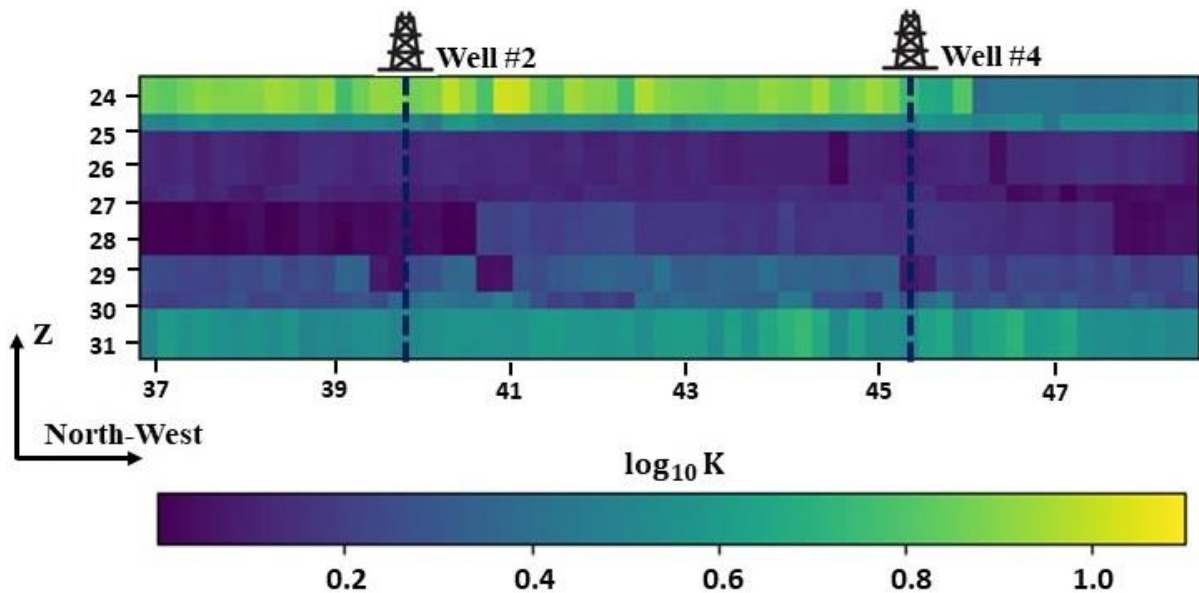
Figures 3.10a and b show the mean of the prior and posterior ensemble of K in the cross-sectional area of Well #2 and Well #4 respectively. Regarding to Figure 3.10, the range of K values in cross-

section (b) are higher than range of K in cross-section (a). this is consistent with the results in Figure 3.9 where the mean of distribution of posterior ensemble of K moved toward higher K values after nine assimilation steps. It should be noted that the same K distribution is used by SGS across whole aquifer thickness to generate prior ensemble of K (Figure 3.10a, Figure 3.1). A zone with higher range of K in cross-section (b) (Figure 3.10b) from depth of 27 m to the bottom of aquifer was created after nine steps of cross-borehole ERT data assimilation. The lithological log (Figure 1.11b) shows the same layer at the bottom of aquifer with a higher quantity of gravel associated with higher K. The difference between prior and posterior K ensemble was calculated in order to visualize the update intensity in every pixel of the cross-sectional area (Figure 3.10c). The standard deviation values of posterior K ensemble were plotted in Figure 3.10d. The standard deviation values have less intensity in the interval depth of 25 m to 30 m of cross-section where the downhole electrodes were mounted. It shows that rate of convergence to an unbiased K estimation is higher for the area which has been covered by cross-borehole ERT data. in other words, it shows all the K models of ensemble converge to a very similar solution in that interval of depth.





(c)



(d)

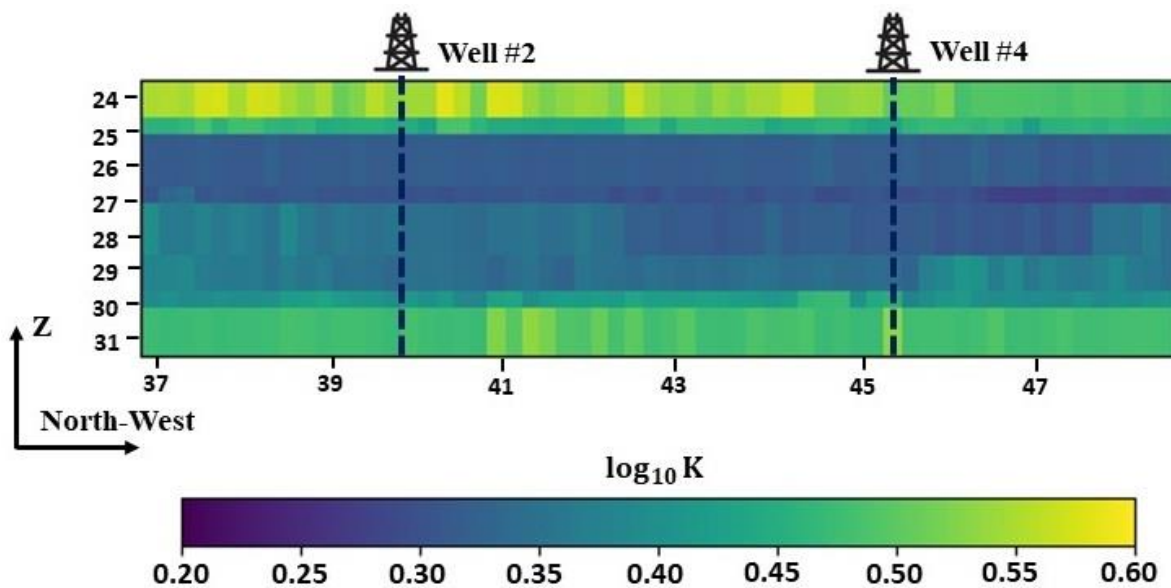


Figure 3.10 : The cross-section between Well #2 and Well #4. a) initial K distribution. b) K distribution after last assimilation step. c) the misfit between cross-section a and b which shows the updated values during assimilation experiment. d) Standard deviation of posterior K distribution at each pixel of cross-section was mapped. Each pixel size is 0.5 m by 0.2 m along Z and X axis respectively.

4 Discussion

The purpose of this study was to investigate the ability of cross-borehole ERT data assimilation using EnKF in a heat tracing experiment in order to estimate the subsurface K heterogeneity. The study provides a numerical tool for eventually simulating the operation of a GWHP system. To the best of our knowledge, this is the first time that ERT data assimilation using EnKF has been applied in the scope of a heat tracing experiment to assess the GWHP potential.

During this study, we were trying to answer the following questions:

1. Are the cross-borehole ERT measurements representative of hydrological change during the heat tracing experiment?
2. Is the ERT data assimilation capable of estimating the K heterogeneity?
3. Is the posterior K model able to predict the future state of the system?

The heat tracing test has been carried out to support the definition of the major hydraulic parameters of the aquifer. In this context, downhole temperature monitoring and electrical resistivity tomography (ERT) can provide relevant, qualitative and quantitative information about the temperature distribution during heat tracing experiments (Hermans, et al., 2012; Hermans, et al., 2015; O Saar, 2011; Anderson, 2005; Maria Sole Giambastiani, et al., 2013; Irving & Singha, 2010). In that case, the ERT inversion and groundwater flow and heat transfer numerical model are essential to fully understand the heat tracing process (Culturra, et al., 2018). To answer the first question, the time-lapse ERT inversion was performed to assess the quality of acquired time-lapse cross-borehole ERT data during the heat tracing test. The cross-hole ERT data must provide information about the dynamic temperature distribution of the aquifer during the heat tracing experiment in order to make a significant update to the K model during the data assimilation experiment. On the other hand, the uncertainty in the measurements and numerical model such as boundary condition, hydrogeological parameters were neglected in the conventional workflow; data assimilation method such as EnKF (Evensen, 1994) provides a promising tool to address such uncertainties. Therefore, in this study EnKF was used to address the uncertainties in the cross-borehole ERT measurements and groundwater flow and heat transfer numerical model.

In the recent decades, the capability of ERT data assimilation using EnKF in hydrogeological application has been investigated (Yan & Dongxiao, 2006; Tso, et al., 2020; Bouzaglou, et al., 2018). These included, using EnKF coupled with hydrogeological inversion used for a synthetic

tracer test experiment to characterize the heterogeneous K fields (Camporese, et al., 2011; Camporese, et al., 2015); as another example, the EnKF was used in controlled laboratory case studies to estimate the K and longitudinal dispersivity (Bouzaglou, et al., 2018).

Unlike previous studies (Bouzaglou, et al., 2018; Yan & Dongxiao, 2006; Tso, et al., 2020) the proposed flowchart is implemented in a field heat tracing experiment instead of synthetic case or controlled laboratory setting in order to answer the second question. We assessed the ability of the proposed flowchart to tackle the measurements, subsurface hydrogeological condition, groundwater flow and heat transfer numerical model uncertainties which are typical of field experiments. It must be noted that we only studied the uncertainty of K with some deterministic parameters (fixed variogram parameters, fixed markers between layers). We did this assumption because we think K is the main uncertain parameter. It could be interesting to investigate the other source of uncertainties such as, varying variogram parameters, the boundary conditions, or other geological parameter uncertainty.

The process of sizing GWHP system is mainly based on the result of the numerical model before the installation of the GWHP system (Ahmadfar & Bernier, 2014; Raymond, 2019). The K heterogeneity has a significant effect on the accuracy of numerical modelling results. Therefore, smoothing effect associated with inversion used to estimate K heterogeneity can impose overestimation or underestimation in the GWHP sizing process. For example, Paradis et al., (2015) performed a resolution analysis of tomographic slug test head data and demonstrated the smoothing of estimated K between boreholes. In previous study of ERT data assimilation using EnKF, Bouzaglou, et al., (2018) concluded that integrating ERT inversion map in ERT data assimilation result in over-smoothing in estimated hydraulic parameters compared to the case where the raw electrical potential data are used. Therefore, ERT inversion is not included in our flowchart to avoid smoothing effect which ends up eliminating the head and tail of the inverted parameter's distribution that typically exist in ERT inversion results due to regularization terms (Day-Lewis, et al., 2005) .

To answer the third question, in addition to assimilation steps two prediction steps were considered to evaluate the ability of the posterior K model to predict the future state of the groundwater temperature accurately.

Overall, we argue that the results support and augment the previous studies (Bouzaglou, et al., 2018; Camporese, et al., 2015; Camporese, et al., 2011) by showing that the proposed ERT data

assimilation flowchart is capable of reproducing the aquifer K heterogeneity. Although a multiplicative inflation factor was used to alleviate variance reduction during assimilation steps, the prior K distribution variance was reduced by fifty percent after nine steps of assimilation, moreover, based on the lithological log (Figure 1.11b) the thickness of gravel layer (Figure 3.10b) at the bottom of aquifer has been overestimated by EnKF which can be due to spurious correlation and limited ensemble size which are typical problems of data assimilation method.

This study provides a numerical tool that can be used during feasibility study of GWHP systems to improve our knowledge of subsurface hydrogeological condition to optimize the GWHP design process by estimating aquifer K heterogeneity model more accurately, which improve the numerical modeling results to estimate/predict the present/future state of GWHP system. Using ERT survey as monitoring tool decreases the cost of drilling operation by minimizing the number of required boreholes.

A set of codes has been developed in Python (Shariatnik, 2022) for the implementation of the suggested workflow. The codes developed in this study consist of the following steps:

- Generate the cross-borehole ERT measurement error model.
- Specify each initial/updated ensemble member of K to the FEFLOW mesh.
- Run FEFLOW.
- Extract the underground temperature model as a result of the last step.
- Convert the temperature model into resistivity model by means of petrophysical relations.
- Run electrical forward modeling
- Assimilate the ERT data to update the ensemble of K

The Python parallel computation module called joblib (Varoquaux, 2022) was used in our code to perform a set of parallel FEFLOW simulations. Using joblib allowed us to execute ten FEFLOW simulations at once.

In this study, the observation interval was between 6 and 12 hours, but it is recommended for further studies that this interval be reduced. In particular, at the beginning of the heat injection experiment when the baseline temperature is disturbed, and the underground temperature undergoes a significant change. To this end, Syscal Pro Switch (IRIS, 1991) offers remote option which allows to remotely control and perform the ERT survey via a PC more frequently.

5 CONCLUSIONS

ERT observations are indirect and low-cost measurements in earth's shallow subsurface. They are worthwhile to be considered for data assimilation experiment as they provide high spatial and temporal resolution data. In this study, we investigated the implementation of the time-lapse cross borehole ERT data assimilation that can reproduce the K heterogeneity of a shallow unconfined sandy-gravel aquifer in a heat tracing experiments. Understanding the heterogeneity of K in an aquifer is very important for designing a GWHP system. We proposed a workflow consisting of assimilation of cross-borehole ERT data as an observation tool into a heat tracing experiment. We performed unconditional sequential Gaussian simulations to generate multiple equiprobable scenarios of K based on using priory available lithologic logs and bibliographic data. The provided realizations are served as the initial ensemble of K to initiate assimilation experiments. The TRT was performed to measure the thermal conductivity of each lithostratigraphic units. In addition, Air- pressurized slug tests were performed to measure the K of the aquifer and the slug test results were used to assess the assimilation results. Moreover, a geological and hydrogeological report done by University of Laval (Talbot Poulin, et al., 2013) was used to provide us with the hydraulic and thermal properties values of each lithostratigraphic unit to creates numerical model of groundwater flow and heat transfer.

The quality of time-lapse cross-borehole ERT measurements was evaluated within two steps. Firstly, the mean apparent resistivity of monitoring datasets was plotted versus time. Secondly, the cross-borehole ERT data was inverted to check if the inverted model can image the heat injection process.

The assimilation experiment was carried out in two steps of assimilation and prediction. In the first step nine ERT datasets are assimilated to update the ensemble of K. In the second step, last two ERT datasets are masked. In a better word, the assimilation step is escaped to assess the reliability of the updated ensemble of K in order to predict the future state of the system. The comparison between the modeled electrical resistivity values and field measurement in both assimilation and prediction steps shows good match between them, confirming the reliability of the approach. The assimilation experiment was repeated with different ensemble sizes to optimize this parameter. The ensemble size of sixty was chosen as optimum ensemble size since the modeled ERT measurements converges to field measurements, the ensemble variance didn't collapse and run time was reasonable. The running time for sixty realizations and 11 time-steps is 72 hours approximately.

In this study, we demonstrated that the assimilation of ERT data into numerical model of groundwater flow and heat transfer is an effective tool which can provide a better characterization of heterogeneity of the aquifer K which is essential in the process of evaluating GWHP potential. Moreover, this method can be considered as an approach to assess the subsurface K heterogeneity. The comparison between prior and posterior distribution of K with geometric mean of slug tests results confirm that the updates imposed to the ensemble of K over 9 assimilation steps caused the mean value of the ensemble of K to move toward the geometric mean of slug tests that proves the model is converging to an unbiased estimation.

A cross-section between cross-borehole ERT observation wells (Well#2 and Well #4) was created to make a visual comparison between the mean of the prior and posterior ensemble of K. The comparison demonstrates that a layer with higher K at the bottom of aquifer was created by ERT data assimilation experiment which is confirmed by lithological log (Figure 1.11b). The standard deviation of the posterior ensemble of K shows less values in the depth interval covered by downhole ERT electrodes. This demonstrates that the convergence rate towards an unbiased estimate of K is higher within this depth interval.

Future studies could be carried out to explore an extended version of the present methodology. The assimilation of distributed temperature sensing with fiber optic data which provide high resolution temperature data in wells and water level monitoring data in addition to the ERT data during the experiment might help to better replicate the field temperature measurement and hydraulic head in boreholes within modeling domain. In addition, the calibration of the petrophysical model for the experimental site may improve the representativity of the simulated resistivity model.

The possibility of using EnKF to predict the future state of a geothermal system such as heat storage systems or deep geothermal resources in the long term could be attractive in further studies.

6 References

- Anderson, M. P., 2005. Heat as a Ground Water Tracer. *Ground Water*, 43(6), pp. 951-968.
- Aghasi, A., Mendoza-Sanchez, I. and Miller, E. L., 2013. A geometric approach to joint inversion with applications to contaminant source zone characterization. *Inverse Problems*, Volume 29, p. 11514.
- Archie, G. E., 2013. The Electrical Resistivity Log as an Aid in Determining Some Reservoir Characteristics. *Transactions of the AIME*, 146(01), pp. 54-62.
- Ahmadfar, M. and Bernier, M., 2014. *An alternative to ASHRAE's design length equation for sizing borehole heat exchangers.*, Seattle: ASHRAE Transactions(Vol. 120, Issue 2).
- Binley, A., Ramirez, A. and D Daily, W., 1995. *Regularised Image Reconstruction of Noisy Electrical Resistance Tomography Data*. Bergen, Proceeding of the 4th Workshop of the european concerted Action on process tomography, pp. 401-410.
- Binley, A., Ramirez, A. and D. Daily, W., 1995. *Regularised Image Reconstruction of Noisy Electrical Resistance Tomography Data*. Bergen, Proceededdings of the 4th Workshop of the European Concered Actionon Process Tomography , pp. 401-410.
- Binley, A., Hubbard, S. S., Huisman, J. A., Revil, A., Robinson, D. A., Singha, K., Slater, L. D., 2015. The emergence of hydrogeophysics for improved understanding of subsurface processes over multiple scales. *Water Resources Research*, 51(6), pp. 3837-3866.
- Bouzaglou, V., Crestani, E., Salandin, P., Gloaguen, E., Camporese, M., 2018. Ensemble Kalman Filter Assimilation of ERT Data for Numerical Modeling of Seawater Intrusion in a Laboratory Experiment. *Water*, 10(4).
- Bayer, P., Attard, G., Blum, P. and Menberg, K., 2019. The geothermal potential of cities. *Renewable & Sustainable Energy Reviews*, Volume 106, pp. 17-30.
- Bruhwiler, L., Basu, S., Butler, J. H., Chatterjee, A., Dlugokencky, E., Kenney, M. A., McComiskey, A., Montzka, S. A., Stanitski, D., 2021. Observations of greenhouse gases as climate indicators. *Climatic Change*, 165(1).
- Chen, Y. and Zhang, D., 2006. Data assimilation for transient flow in geologic formations via ensemble Kalman filter. *Advances in Water Resources*, 29(8), pp. 1107-1122.

Camporese, M., Cassiani, G., Deiana, R. and Salandin, P., 2008. Assessment of local hydraulic properties from Electrical Resistivity Tomography monitoring of tracer test experiments. *Water Resources Research*, 47(12).

Camporese, M., Cassiani, G., Deiana, R. and Salandin, P., 2011. Assessment of local hydraulic properties from Electrical Resistivity Tomography monitoring of tracer test experiments. *Water Resources Research*, 47(12).

Camporese, M., Cassiani, G., Deiana, R., Salandin, P., Binley, A., 2015. Coupled and uncoupled hydrogeophysical inversions using ensemble Kalman filter assimilation of ERT-monitored tracer test data. *Water Resources Research*, 51(5), pp. 3277-3291.

Culturera, M., Boaga, J., Sipio, E. D., Dalla Santa, G., De Seta, M., Galgaro, A., 2018. Modelling an induced thermal plume with data from electrical resistivity tomography and distributed temperature sensing: a case study in northeast Italy. *Hydrogeology Journal*, Volume 26, pp. 837-851.

DHI, M. P. b., n.d. Website, FEFLOW 7.3 Documentation. [Online] Available at: feflow.info/html/help73/feflow/01_Introduction/morehelp/documentation.html

Domenico, A. P. and Schwartz, W. F., 1998. *Physical and Chemical Hydrogeology*. New York, United states: Wiley.

Day-Lewis, F., Singha, K. and Binley, A., 2005. Applying petrophysical models to radar travel time and electrical resistivity tomograms: Resolution-dependent limitations. *Journal of Geophysical Research Atmospheres*, 110(B8).

Diersch, H.-J. G., 2014. *FEFLOW, Finite Element Modeling of Flow, Mass and Heat Transport in Porous and Fractured Media*. New York: Springer.

Earth Science Communications team at NASA's Jet Propulsion Laboratory, C. I. o. T., n.d. *Global Climate Change* NASA. [Online] Available at: <https://climate.nasa.gov/vital-signs/global-temperature/>

European Environment Agency, 1993. Website, European Environment Agency. [Online] Available at: <https://www.eea.europa.eu/data-and-maps/indicators/atmospheric-greenhouse-gas-concentrations/atmospheric-greenhouse-gas-concentrations-assessment>

Evensen, G., 1994. Sequential data assimilation with a nonlinear quasi-geostrophic model using Monte Carlo methods to forecast error statistics. *Journal of Geophysical Research: Oceans*, 99(C5), pp. 10143-10162.

- Evensen, G., 2003. The ensemble Kalman filter: Theoretical formulation and practical implementation. *Ocean dynamics*, 53(4), pp. 343-367.
- Evensen, G., 2009. *Data Assimilation, The Ensemble Kalman Filter*. New York: Springer.
- Ferguson, G. and D. Woodbury, A., 2004. Subsurface heat flow in an urban environment. *Journal of geophysical research*, 109(B2), pp. 1-9.
- Focaccia, S., Tinti, F. and Bruno, R., 2013. A software tool for geostatistical analysis of thermal response. *Computers & Geosciences*, Volume 59, pp. 163-170.
- Gibb, J. P., Barcelona, M. J., Ritchey, J. D. and LeFaivre, M. H., 1984. *Effective Porosity of Geologic Material, First Annual Report*, Champaign, Illinois: Illinois Department of Energy and Natural Resources.
- Günther, T., 2004. *PhD Thesis, Inversion Methods and Resolution Analysis for the 2D/3D Reconstruction of Resistivity Structures from DC Measurements*, s.l.: Technischen Universität Bergakademie Freiberg.
- Günther, T., Rücker, C. and Spitzer, K., 2006. Three-dimensional modelling and inversion of DC resistivity data incorporating topography—II. Inversion. *Geophysical Journal International*, 166(2), pp. 506-517.
- Giambastiani, B. M. S., Colombani, N. and Mastrocicco, M., 2013. Limitation of using heat as a groundwater tracer to define aquifer properties: experiment in a large tank model. *Environmental Earth Sciences*, Volume 70, pp. 719-728.
- G. Diersch, H.-J., 2014. *FEFLOW, Finite Element Modeling of Flow, Mass and Heat Transport in Porous and Fractured Media*. New York: Springer.
- Gernez, S., Bouchedda, A., Gloaguen, E. and Paradis, D., 2019. Comparison Between Hydraulic Conductivity Anisotropy and Electrical Resistivity Anisotropy From Tomography Inverse Modeling. *Environ. Sci.*, Volume 7.
- Gunther, T. and Ruckery, C., 2019. Boundless Electrical Resistivity Tomography BERT 2 { the user tutorial.
- H. Jazwinski, A., 2007. *Stochastic processes and filtering theory*. New York: Dover Publications.
- Hayley, K., Bentley, L., Gharibi, M. and Nightingale, M., 2007. Low temperature dependence of electrical resistivity: Implications for near surface geophysical monitoring. *Geophysical Research Letters*, 34(18).

Hermans, T., Vandenbohede, A., Lebbe, L. and Nguyen, F., 2012. A shallow geothermal experiment in a sandy aquifer monitored using electric resistivity tomography. *GEOPHYSICS*, 77(1), pp. B11-B21.

Hermans, T., Wildemeersch, S., Jamin, P., Orban, P., Brouyère, S., Dassargues, A., Nguyen, F., 2015. Quantitative temperature monitoring of a heat tracing experiment using cross-borehole ERT. *Geothermics*, pp. 14-26.

Hwang, H. T., Jeen, S. W., Suleiman, A. A. and Lee, K. K., 2017. Comparison of Saturated Hydraulic Conductivity Estimated by Three Different Methods. *Water*, 9(12).

IRIS, 1991. *IRIS Instruments*. [Online]

Available at: http://www.iris-instruments.com/Pdf_file/Syscal_pro_sw.pdf

Irving, J. and Singha, K., 2010. Stochastic inversion of tracer test and electrical geophysical data to estimate hydraulic conductivities. *Water Resources Research*, 46(11).

Ižvolta, L. and Dobeša, P., 2014. Test Procedure Impact for the Values of Specific Heat Capacity and Thermal Conductivity Coefficient. *Procedia Engineering*, Volume 91, pp. 453-458.

J. Fletcher, S., 2017. *Data assimilation for the geosciences*. Amsterdam, North Holland: Candice Janco Press.

J. Fletcher, S., 2017. *Data Assimilation for the Geosciences From Theory to Application*. Amsterdam: Candice Janco.

Kálmán, R. E., 1960. A New Approach to Linear Filtering and Prediction Problems. *Journal of Basic Engineering*, Volume 82, pp. 35-45.

Kaviany, M., 1995. *Principles of Heat Transfer in Porous Media*. New York, United States : Springer Press.

Loke, M. H., 2001. *Constrained Time-Lapse Resistivity Imaging Inversion*. Denver, Colorado, USA, s.n.

Ladislaus, R., 2001. *Design and performance of borehole heat exchanger/heat pump systems..* Oradea/Romania, s.n.

Loke, M. H., 2013. Tutorial: 2-D and 3-D electrical imaging surveys. *Geotomo software Malaysia*.

Lamarche, L., 2011. *Palaeoenvironmental evolution of quaternary dynamics in the Quebec City region: Application in three-dimensional and hydrogeological modelling*. PhD thesis, Quebec City: Institut national de la recherche scientifique-Centre Eau Terre Environnement.

Leung, J., 2018. *Report, Decarbonizing U.S. Buildings*, s.l.: Center for Climate and Energy Solutions.

Lee, V. Raymond, J., Rivard, C., Comeau, F. A., Newson, J., 2021. *Groundwater Heat Pump (GWHP) Systems to Fight Urban Heat Islands: A solution for Canada's Major Cities*. Toronto, ON, Canada, s.n.

Menke, W., 1984. *Geophysical Data Analysis: Discrete Inverse Theory*. New York: Academic.

Maslin, M., 2004. *Global Warming, A Very Short Introduction*. New York: Oxford University Press.

Marsily, d. G., Delay, F., Goncalves, J., Renard, P., Teles, V., Violette, S., 2005. Dealing with spatial heterogeneity. *Hydrogeology Journal*, 13(1), p. 161–183.

Miller, C. R., Routh, P. S., Brosten, T. R. and McNamara, J. P, 2008. Application of time-lapse ERT imaging to watershed characterization. *Society of Exploration Geophysicists*, 73(3), pp. 1942-2156.

Mackenzie Macdonald, A., Barker, J. A. and Davies, J., 2008. The bailer test: A simple effective pumping test for assessing borehole success. *Hydrogeology Journal*, 16(6), pp. 1065-1075.

Majorowicz, J., E. Grasby, S. and R. Skinner, W., 2009. Estimation of Shallow Geothermal Energy Resource in Canada: Heat Gain and Heat Sink. *Natural Resources Research*, 18(2), pp. 95-108.

Maidment, G., 2013. *Ground source heat pumps*. Levenham: Lavenham Press.

Nakicenovic, N., Davidson, O., Davis, G., Grübler, A., Kram, T., Rovere, Emilio., Metz, B., Morita, T., Pepper, W., Pitcher, H., Sankovski, A., Shukla, P., Swart, R., Watson, R., Dadi, Z., 2000. *Summary for Policymakers, Emissions Scenarios*, s.l.: Intergovernmental Panel on Climate Change (IPCC).

Oldenborger, G. A., Routh, P. S. and Knoll, M. D., 2005. Sensitivity of electrical resistivity tomography data to electrode position errors. *Geophysical Journal International*, 163(1), pp. 1-9.

Okpoli, C. C., 2013. Review Article, Sensitivity and Resolution Capacity of Electrode Configurations. *International Journal of Geophysics*.

Olsthoorn, T., 2019. *FD modeling course groundwater flow 0.01 documentation*. [Online] Available at: <https://olsthoorn.readthedocs.io/en/latest/index.html>

Pidlisecky, A., Singha, K. and Day-Lewis, F. D., 2011. A distribution-based parametrization for improved tomographic imaging of solute plumes. *Geophysical Journal International*, 187(1), pp. 214-224.

Paradis, D., Gloaguen, E., Lefebvre, R. and Giroux, B., 2015. Resolution analysis of tomographic slug test head data: Two-dimensional radial case. *Water Resources Research*, 51(4), pp. 2356-2376.

Park, Y., Kim, N. and Lee, J.-Y., 2015. Geochemical properties of groundwater affected by openloop geothermal heat pump system in Korea. *Geosciences Journal*, 19(3), pp. 515-526.

Remy, N., Boucher, A. and Wu, J., 2009. *Applied Geostatistics with SGeMS, A User's Guide*. United Kingdom: Cambridge University Press.

Raymond, J., 2018. Colloquium 2016: Assessment of subsurface thermal conductivity for geothermal applications. *Canadian Geotechnical Journal*.

Raanes, P., 2016. PhD Thesis, Improvement to ensemble methods for data assimilation in the geosciences. *University of oxford*.

Rossati, A., 2017. Global Warming and its Health Impact. *International Journal of Occupational and Environmental Medicine*, Volume 8, pp. 7-20.

Raymond, J., 2019. *Heat transfer applied to earth science- Course Note*. Quebec City, Canada, s.n.

Springer, R.K. and L.W. Gelhar, 1991. Characterization of large-scale aquifer heterogeneity in glacial outwash by analysis of slug tests with oscillatory response, Cape Cod, Massachusetts, U.S. Geol. Surv. Water Res. Invest. Rep. 91-4034, pp. 36-40.

Sen, P. N. and Goode, P. A., 1992. Influence of temperature on electrical conductivity on shaly sands. *GEOPHYSICS*, Volume 57, pp. 89-96.

Singha, K. and Gorelick, S. M., 2006. Effects of spatially variable resolution on field-scale estimates of tracer concentration from electrical inversions using Archie's law. *GEOPHYSICS*, 71(3).

Saar, M. O., 2011. Review: Geothermal heat as a tracer of large-scale groundwater flow and as a means to determine permeability fields. *Hydrogeology Journal volume*, Volume 19, pp. 31-52.

Sarbu, L. and Sebarchievici, C., 2016. *Ground-Source Heat Pumps, Fundamentals, Experiments and Applications*. New York: Academic Press.

Saneiyan, S., Boyd, J., Blanchy, G. and McLachlan, P., 2018. *ResIPy documentation master file*. [Online]

Available at: <https://hkex.gitlab.io/resipy/>

Shariatinik, B., Bouchet, A., Gloaguen, E., Raymond, J., Fabien-Ouellet, G., 2021. *A heat tracing experiment using cross-borehole time-lapse ERT*. Bordeaux, France, Conference: NSG2021 2nd Conference on Geophysics for Infrastructure Planning, Monitoring and BIM.

Shariatinik, B., 2022.[Online] Available at: <https://github.com/Benyamin-Shariatinik/EnKF-ERT> [Accessed 09 08 2022].

Truffert, C., 1990. *IRIS Instrument*. [Online]
Available at: <http://www.iris-instruments.com/elrec-pro.html>

Tarantola, A., 2005. Inverse Problem Theory and Methods for Model Parameter Estimation. ebook: Society for Industrial and Applied Mathematics.

Tomopoulos, N. T., 2013. *Essential of Monte Carlo Simulation, statistical method for building simulation moddels*. New York: Springer.

Talbot Poulin, M.C., Comeau, G., Tremblay, Y., Therrien, R., Nadeau, M.M., Lemieux, J.M., Molson, J., Fortier, R., Therrien, P., Lamarche, L., Donati-Daoust, F., Bérubé, S., 2013. *Projet d'acquisition de connaissances sur les eaux souterraines du territoire de la Communauté métropolitaine de Québec (PACES-CMQ), Rapport final*, ville de Québec: Département de géologie et de génie géologique, Université Laval.

Tso, C. H., Johnson, T. C., Song, X.; Chen, X., Kuras, O., Wilkinson, P., Uhlemann, S., Chambers, J., Binley, A., 2020. Integrated hydrogeophysical modelling and data assimilation for geoelectrical leak detection. *Journal of Contaminant Hydrology*, Volume 234.

U.S Department of ENERGY, n.d. *Energy.gov*. [Online]
Available at: <https://www.energy.gov/energysaver/geothermal-heat-pumps>

Varoquaux, G., 2022. *Joblib*. [Online]
Available at: https://joblib.readthedocs.io/_downloads/en/latest/pdf/ [Accessed 2008].

Wiklea, C. K. and Berliner, L. M., 2007. A Bayesian tutorial for data assimilation. *Physica D: Nonlinear Phenomena*, 230(1-2), pp. 1-16.

Wu, G. and Zheng, X., 2017 [online]. The Error Covariance Matrix inflation in Ensemble Kalman Filter. In: *Kalman Filters-Theory for Advanced Applicatoions*. London, United Kingdom: IntechOpen.

Woessner, W. W. and Poeter, E. P., 2020. *Hydrogeologic Properties of Earth Materials and Principles of Groundwater Flow*. Guelph, Ontario, Canada: The Groundwater Project.

Xu, Y.S., Wang, X.W., Shen, S.L. and Zhou, A., 2020. Distribution characteristics and utilization of shallow geothermal energy. *Energy & Buildings*, Volume 229.

Yan, C. and Dongxiao, Z., 2006. Data assimilation for transient flow in geologic formations via ensemble Kalman filter. *Advances in Water Resources*, 29(8), pp. 1107-1122.

